UNIVERSITÀ DI PISA

FACOLTÀ DI SCIENZE MATEMATICHE, FISICHE E NATURALI

DIPARTIMENTO DI FISICA

TESI DI LAUREA MAGISTRALE

Josephson effect in ballistic semiconductor nanostructures

Laureando

Antonio Fornieri

Relatori

Dott. Francesco Giazotto

Dott. Vittorio Pellegrini

ANNO ACCADEMICO 2012/2013

To my parents

Bohr: So, Heisenberg, why did you come?
Heisenberg: Why did I come?
Bohr: Tell us once again. Another draft of the paper. And this time we shall get it right. This time we shall understand.
Margrethe: Maybe you'll even understand yourself.

— Michael Frayn, *Copenhagen*

Contents

Introduction

The Josephson effect [1] is one of the most remarkable macroscopic manifestations of quantum mechanics. It consists in the dissipationless flowing of a phase-coherent current between two superconducting leads, coupled by a weak-link. The weak-link can be made of a thin insulating layer (S-I-S junctions) or a short section of normal conducting material (S-N-S junctions) [2]. In recent years, semiconducting weak-links have been the focus of increasing interest driven by the fast development of semiconductor electronic devices. Research on such hybrid superconductor/semiconductor devices has been further expanded by the realization of Two-Dimensional Electron Gases (2DEGs) in semiconductor heterostructures, in which the carrier density can be finely controlled and large mobilities can be achieved. This, in particular, has opened the way to the fabrication of ballistic hybrid junctions [3]. In these devices new quantum effects can be observed, which rely on the large Fermi wave-length and electron mean free path of 2DEGs compared to purely metallic structures. A prominent example was the observation of the Josephson current quantization, obtained in a superconducting Quantum Point Contact (QPC) constriction [4, 5].
In this thesis work we have investigated the transport properties of ballistic S-2DEG-S nanostructured junctions, in which the 2DEG is hosted in an InAs-based quantum well. We studied two different designs of the InAs-based semiconducting region: a QPC and a Quantum Ring (QR). First, we fabricated normal QPCs and QRs observing conductance quantization [6, 7] and the magneto-electrostatic Aharonov-Bohm (AB) interference effect [8, 9]. Then, we replaced the normal contacts with Nb leads, thereby fabricating S-QPC-S and S-QR-S junctions. In both these junctions we were able to manipulate the Josephson current by applying external magneto-electrostatic fields. In the case of S-QPC-S junctions, we observed a magnetic interference pattern of the supercurrent and we electrically tailored it by using side gates [10]. We qualitatively confirmed the theoretical predictions made by Barzykin and Zagoskin [11] for the evolution of the interference pattern as a function of the gate voltage and temperature. In S-QR-S junctions, we found that the magnetic modulation of the Josephson current displays a periodicity h/e [12] (where h is the Planck's constant and e

the electron charge) typical of the AB effect, in contrast to the standard $h/2e$ period observed in conventional superconducting quantum interference devices (SQUIDs), implemented either with two Josephson junctions in parallel [2] or with metallic rings in the diffusive regime [13]. This difference stems from the topology and the ballistic nature of our junction, which consists of a single ring-shaped weak-link connecting the same superconducting leads. Within the ballistic weak-link the electrons are influenced by the external magnetic field as in a normal QR, thus giving rise to the AB periodicity of the supercurrent interference pattern. The obtained result agrees with the theoretical prediction made by Dolcini and Giazotto [14] for this particular system and offer the first experimental verification of this effect.

The thesis is organized as follows:
Chapter 1 presents the fundamentals of the Josephson effect in S-2DEG-S junctions. It starts with the introduction of the Bogoliubov-de Gennes equations, which constitute the basic theoretical instrument to describe inhomogeneous superconducting systems. Then we discuss the transport properties of a N/S interface, presenting the Andreev reflection process and the Blonder-Tinkham-Klapwijk model. After a brief introduction of the 2DEG characteristics, the Josephson current in semiconducting hybrid junctions is theoretically described as the sum of the contributions carried by Andreev continuous and bound states. At the end of the chapter, some features of the junction dissipative state are presented.
In **chapter** 2 we present a brief overview of the results found in literature for devices similar to those here considered.. In particular, we describe the conductance quantization observed in normal QPCs and the AB interference effect measured in normal QRs. Afterwards, we discuss the Josephson current dependence on external magneto-electrostatic fields in S-QPC-S and S-QR-S junctions. In the case of S-QPC-S junctions, we describe the supercurrent quantization and the magnetic interference effect, giving account for the most relevant theoretical models and experimental results. Then, in the last section of the chapter, we present the theoretical predictions for the interferometric properties of the ballistic S-QR-S junctions.
Chapter 3 is dedicated to the accurate description of the nanofabrication procedure followed to realize the investigated devices. Afterwards, the experimental setup used to perform low-temperature transport measurements is presented in **chapter** 4.
In **chapter** 5 we illustrate and discuss the obtained experimental data. The first two sections report the results for the normal devices, which allowed us to test

the fabrication process and the 2DEG properties. Then, in the following sections, we focus on the study of the ballistic hybrid junctions. After a preliminary characterization of the devices, we investigate the Josephson current behaviour in the presence of magneto-electrostatic fields, comparing the experimental data to the theoretical predictions discussed in the first part of the thesis.
Finally, in **chapter** 6 we resume the results of our experiments, together with some possible future extensions of the present work.

Chapter 1

Superconductor/semiconductor Josephson junctions

1.1 The Bogoliubov-de Gennes equations

In 1957 Bardeen, Cooper and Schrieffer (BCS) formulated the first microscopic theory [15, 16] of superconductivity since its discovery in 1911 [17]. They found that two electrons near the Fermi surface with opposite wave vector k and spin can form a Cooper pair ($\mathbf{k}\uparrow, -\mathbf{k}\downarrow$). The electron pairing is mediated by a weak electron-phonon coupling, also known as the Frölich interaction. Because of this attractive interaction, Cooper pairs behave as boson-like particles, being able to condense to an energetically lower ground state. Even though the ground state energy is lower, the kinetic energy of the electrons can be higher than the kinetic energy of electrons in a non-interacting Fermi gas. In fact, at 0 K the negative pairing energy enables the electrons to occupy states with $k > k_F$, where k_F is the Fermi wave number.

The excited states of a superconductor system at T = 0 K can be obtained using the Bogoliubov canonical transformations to diagonalize the BCS mean-field Hamiltonian [18, 19]. In this way, it turns out that the excitations of the condensed ground state are formed by fermionic quasi-particles, consisting of a linear combination of electron and hole ladder operators. Their energy spectrum is represented in Fig. 1.1. In comparison to the normal metal excitation energy, an energy gap Δ_0 is opened at Fermi energy E_F, owing to the attractive interaction between electrons in the ground state. The Cooper pair has to absorb an energy equal to $2\Delta_0$ to split up. For $k > k_F$ the quasi-particles can be regarded as electron-like, while for $k < k_F$ they acquire a hole-like character [20].

In order to treat inhomogeneous systems at a microscopic level, the quasi-

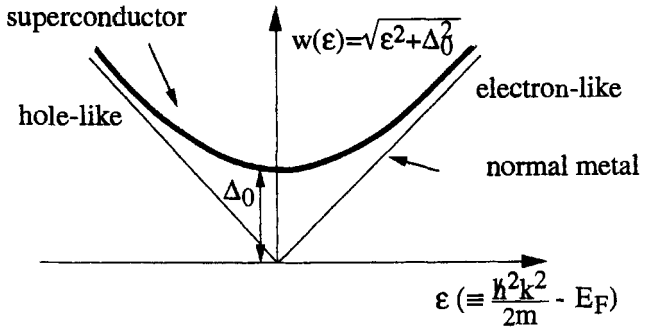

Figure 1.1: BCS quasi-particle energy spectrum for the superconductor at T = 0 K, compared to the normal metal excitation energy. The origin is placed at the Fermi energy. Adapted from [20].

particle states introduced above can be described by the Bogoliubov-de Gennes (BdG) equations [21]:

$$\begin{pmatrix} H(\mathbf{r}) & \Delta(\mathbf{r}) \\ \Delta^*(\mathbf{r}) & -H(\mathbf{r}) \end{pmatrix} \begin{pmatrix} u_{\mathbf{k}}(\mathbf{r}) \\ v_{\mathbf{k}}(\mathbf{r}) \end{pmatrix} = E \begin{pmatrix} u_{\mathbf{k}}(\mathbf{r}) \\ v_{\mathbf{k}}(\mathbf{r}) \end{pmatrix}. \tag{1.1}$$

The solution of the BdG equations are electron-like or hole-like quasi-particles represented by the vector $(u_{\mathbf{k}}, v_{\mathbf{k}})$. Here, $H(\mathbf{r})$ is the one-electron Hamiltonian, defined as

$$H(\mathbf{r}) = -\frac{\hbar^2}{2m^*}\nabla^2 + U(\mathbf{r}) - \mu, \tag{1.2}$$

where μ is the chemical potential, m^* is the effective electron mass and $U(\mathbf{r})$ is an external scalar potential. The coupling between the components of the vector $(u_{\mathbf{k}}, v_{\mathbf{k}})$ is provided by the superconducting pair potential $\Delta(\mathbf{r})$. The component $u_{\mathbf{k}}$ represents the probability of an electron-like state, while $v_{\mathbf{k}}$ represents the probability of a hole-like state.
In the case of an homogeneous superconductor with $\Delta(\mathbf{r}) = \Delta_0$, $U(\mathbf{r}) = 0$ and constant μ, the vector $(u_{\mathbf{k}}, v_{\mathbf{k}})$ can be written in a simple form:

$$\begin{pmatrix} u_{\mathbf{k}}(\mathbf{r}) \\ v_{\mathbf{k}}(\mathbf{r}) \end{pmatrix} = e^{i\mathbf{k}\cdot\mathbf{r}} \begin{pmatrix} u_0 \\ v_0 \end{pmatrix}. \tag{1.3}$$

Therefore u_0 and v_0 are given by

$$u_0^2 = \frac{1}{2}\left(1 + \frac{\sqrt{E^2 - \Delta_0^2}}{E}\right), \tag{1.4}$$

$$v_0^2 = 1 - u_0^2, \tag{1.5}$$

where the energy eigenvalues are equal to those calculated for Bogoliubov quasi-particles in the BCS theory:

$$E = \pm \left[\left(\frac{\hbar^2 k^2}{2m_e} - \mu \right)^2 + \Delta_0^2 \right]^{1/2} . \tag{1.6}$$

The minus sign makes sense only in a generalized semiconductor scheme [22], where the hole-like particle energies are defined as negative with respect to the Fermi level. The results obtained for u_0 and v_0 are identical to the BCS coherence factor, with the exception that the former are defined also for $|E| < \Delta_0$. In this case u_0 and v_0 are complex conjugates.
It follows from (1.6) that four values of k correspond to the same energy:

$$\pm k^{\pm} = \pm \frac{\sqrt{2m}}{\hbar} \left[\mu \pm (E^2 - \Delta_0^2)^{1/2} \right]^{1/2} . \tag{1.7}$$

When $|\mathbf{k}| > k_F$, the quasi-particle is predominantly electron like, since $|u_0|^2 > |v_0|^2$, while for $|\mathbf{k}| < k_F$ the character of the particle is predominantly hole-like ($|u_0|^2 < |v_0|^2$).
For a normal conductor, the two components of equation (1.1) are decoupled and pure electrons $(1, 0)$ and holes $(0, 1)$ exist. As one can easily see by solving the BdG equation with $\Delta_0 = 0$, for a hole state the energy eigenvalues are positive for $|\mathbf{k}| < k_F$ and negative for $|\mathbf{k}| > k_F$. This leads to an important consequence: for a hole, the direction of the group velocity

$$\mathbf{v_k} = \frac{1}{\hbar} \nabla_{\mathbf{k}} E \tag{1.8}$$

is opposite to its wave vector $\mathbf{k}$. On the contrary, in the case of an electron, $\mathbf{v_k}$ and $\mathbf{k}$ have the same direction.

1.2 Quasi-particle transport through a N/S interface

In the next sections the BdG equations will be used to treat inhomogeneous systems like normal conductor/superconductor interfaces. First, we will discuss the physical properties of an ideal N/S interface (i. e., with a transmission-probability equal to one), then we will introduce the Blonder-Tinkham-Klapwijk (BTK) model, in order to extend the description to more realistic interfaces.

1.2.1 Andreev reflection

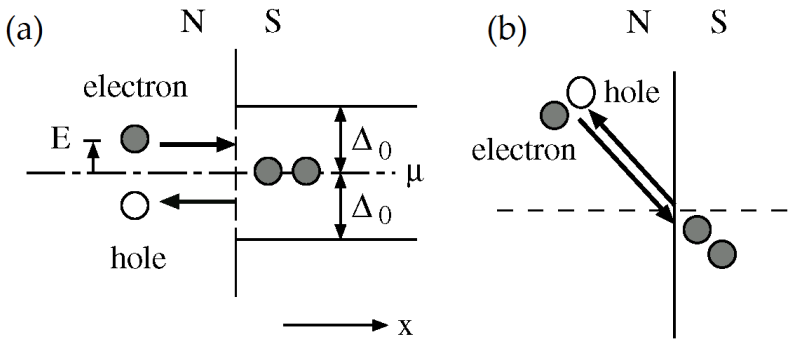

Figure 1.2: (a) Schematic energy diagram of the Andreev reflection mechanism: an incident electron from the N side is retro-reflected as a hole and a Cooper pair is formed in the superconductor. (b) In real space: in contrast to the normal reflection process, the incident electron and the retro-reflected hole have the same wave vector. Adapted from [3].

If a normal metal is coupled to a superconductor, a particular reflection process, namely Andreev reflection, can be observed [23]. This process is schematically represented in Fig. 1.2.

When an electron in the N side with an energy $\mu < E < \Delta_0$ and a wave vector $\mathbf{k}_e$ moves towards the ideal N/S interface, it will be neither transmitted nor normally reflected. In fact, since energy must be conserved in the process, the electron can not find any quasi-particle state at the energy $E < \Delta_0$. Moreover, since the interface is ideal, the electron can not be normally reflected, because there is no barrier which can absorb the momentum difference. Still, a Cooper pair can be created in the superconductor, if an additional electron is transferred from the completely filled Fermi sea of the normal conductor to the superconductor. In order to do so, the wave vector of the second electron must have the same magnitude and the opposite direction with respect to $\mathbf{k}_e$ (the Cooper pair has to be in a singlet state). Since the total wave vector of the completely filled Fermi sea is zero, the resulting wave vector of the system after the Cooper pair creation has to be equal to $\mathbf{k}_e$. Thus, a hole with a wave vector $\mathbf{k}_h = \mathbf{k}_e$ is produced. However, as noticed above, the wave vector and the group velocity of a hole have opposite directions. Because of this, the hole takes the same path as the electron but in the reverse direction [see Fig. 1.2(b)]. This is the reason why this process is also referred to as *retro-reflection*. Considering the opposite charges and the opposite group velocity of electrons and holes, we can conclude that an Andreev reflection provides a conductance which is twice as large as the one for an ideal transmission through the interface.

For an incident electron with $|E| > \Delta_0$, quasi-particle states are available and

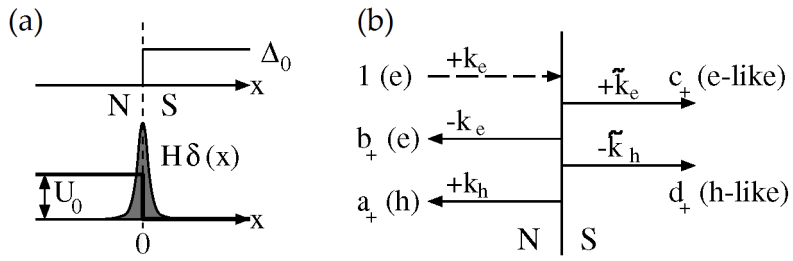

Figure 1.3: (a) BTK model of a N/S interface. A step-like increase of the pair potential $\Delta(x)$ is assumed at the N/S boundary. The potential $U(x)$ is formed by a step of height U_0 and by a δ-shaped barrier at the interface. (b) Scattering process of an incident electron with wave vector k_e. The orientation of the arrows represents the direction of the group velocity. Adapted from [3].

also normal specular reflection occur with a certain probability. In general, N/S interfaces are not ideal and the Andreev reflection probability is less than one even for $|E| < \Delta_0$, if a potential barrier is introduced.

1.2.2 The Blonder-Tinkham-Klapwijk (BTK) model

In 1982 Blonder, Tinkham and Klapwijk (BTK) formulated a one-dimensional model able to describe Andreev and normal reflections, as well as transmission of quasi-particles, at a non-ideal N/S interface [22]. In the model a potential barrier at the interface (due, for instance, to an oxide layer or a Schottky barrier) is approximated by a δ-shaped barrier, as shown in Fig. 1.3. Even though it was not considered in the original model, the Fermi energies of the two materials can differ significantly, since the electron density in a semiconductor is usually much lower than in a superconductor. Consequently, when a semiconductor is coupled to a superconductor, the alignment of the Fermi energies generates a potential step of height U_0 at the bottom of the conduction band at the interface (see Fig. 1.3(a)). This potential step, combined with the δ-shaped barrier, will increase the probability of normal reflections with respect to Andreev reflections. For simplicity, a step-like pair potential is assumed at the N/S boundary: $\Delta(x) = \Theta(x)\Delta_0$. The potential $U(x)$ is defined as follows:

$$U(x) = U_0\Theta(-x) + \frac{\hbar^2 k_{FS}}{m_e} Z\delta(x), \tag{1.9}$$

where $k_{FS} = \sqrt{2m_e\mu/\hbar^2}$ is the Fermi wave number in the superconductor. The height H of the δ-shaped barrier is expressed by the dimensionless parameter

$$Z = H\frac{m_e}{\hbar^2 k_{FS}}, \tag{1.10}$$

which is related to the junction normal-state transmission coefficient

$$\mathcal{T} = \frac{1}{1+Z^2}. \tag{1.11}$$

The scattering process of an incident electron wave

$$\psi_{in} = \begin{pmatrix} 1 \\ 0 \end{pmatrix} e^{ik_e x} \tag{1.12}$$

from the N side is represented in Fig. 1.3(b). As a result, electron-like (u_0, v_0) and hole-like (v_0, u_0) quasi-particles are transmitted into the superconductor:

$$\psi_{trans} = c_+ \begin{pmatrix} u_0 \\ v_0 \end{pmatrix} e^{i\tilde{k}_e x} + d_+ \begin{pmatrix} v_0 \\ u_0 \end{pmatrix} e^{i\tilde{k}_h x}. \tag{1.13}$$

At the same time a fraction of the incident wave is reflected as an electron $(1, 0)$ and as a hole $(0, 1)$:

$$\psi_{refl} = b_+ \begin{pmatrix} 1 \\ 0 \end{pmatrix} e^{-ik_e x} + a_+ \begin{pmatrix} 0 \\ 1 \end{pmatrix} e^{ik_h x}. \tag{1.14}$$

The wave numbers in the normal conductor and superconductor are

$$k_e = \sqrt{k_{FN}^2 + (2m^*/\hbar^2)E}, \tag{1.15}$$

$$k_h = \sqrt{k_{FN}^2 - (2m^*/\hbar^2)E} \tag{1.16}$$

and

$$\tilde{k}_e = \sqrt{k_{FS}^2 + (2m_e/\hbar^2)(E^2 - \Delta_0^2)^{1/2}}, \tag{1.17}$$

$$\tilde{k}_h = \sqrt{k_{FS}^2 - (2m_e/\hbar^2)(E^2 - \Delta_0^2)^{1/2}}, \tag{1.18}$$

respectively. $k_{FN} = \sqrt{(2m^*/\hbar^2)(\mu - U_0)}$ is the Fermi wave number in the normal conductor. Figure 1.4 represents all particles involved in the scattering process in the $E(k)$ dispersion relation [22].

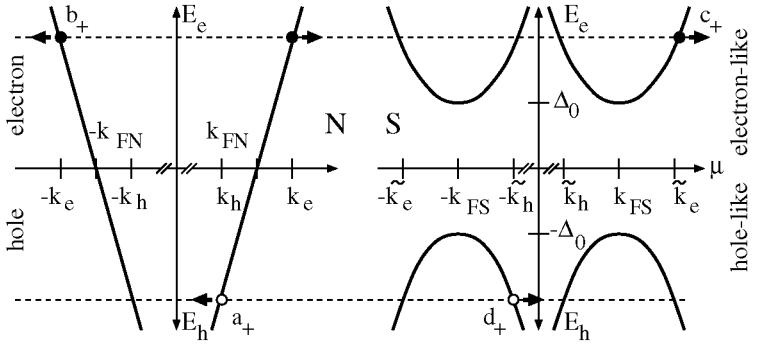

Figure 1.4: Generalized semiconductor description of the $E(k)$ dispersion relation in the normal conductor (N) and in the superconductor (S). The filled circles denote electrons and electron-like quasi-particles, the open circles holes and hole-like quasi-particles. The arrows indicate the direction of the group velocities. The axis of the hole energy E_h is directed downwards. Adapted from [3].

In order to determine the coefficients a_+, b_+, c_+ and d_+, it is necessary to impose the boundary conditions for the wave function and its derivative at the interface:

$$\psi_{in}(0) + \psi_{refl}(0) = \psi_{trans}(0); \tag{1.19}$$

$$\psi'_{in}(0^-) + \psi'_{refl}(0^-) - \psi'_{trans}(0^+) = 2k_{FS}Z\psi(0). \tag{1.20}$$

The results are:

$$a_+ = \frac{u_0 v_0}{\gamma}, \tag{1.21}$$

$$b_+ = \frac{(v_0^2 - u_0^2)(iZ + q)}{\gamma}, \tag{1.22}$$

$$c_+ = \frac{u_0[(1+r)/2 - iZ]}{\gamma}, \tag{1.23}$$

$$d_+ = -\frac{v_0[(r-1)/2 - iZ]}{\gamma}, \tag{1.24}$$

where $\gamma = u_0^2(p+1) - v_0^2 p$, $q = Z^2/r + (1-r^2)/4r$ and $p = Z^2/r + (r-1)^2/4r$. The ratio $r = v_{FN}/v_{FS}$ is the Fermi velocity mismatch between the normal conductor and the superconductor. In the case of $E < \Delta_0$ the quasi-particle waves are exponentially damped, since $\tilde{k}_e$ and $\tilde{k}_h$ contain an imaginary component. Therefore, the transmission coefficients c_+ and d_+ become equal to zero.

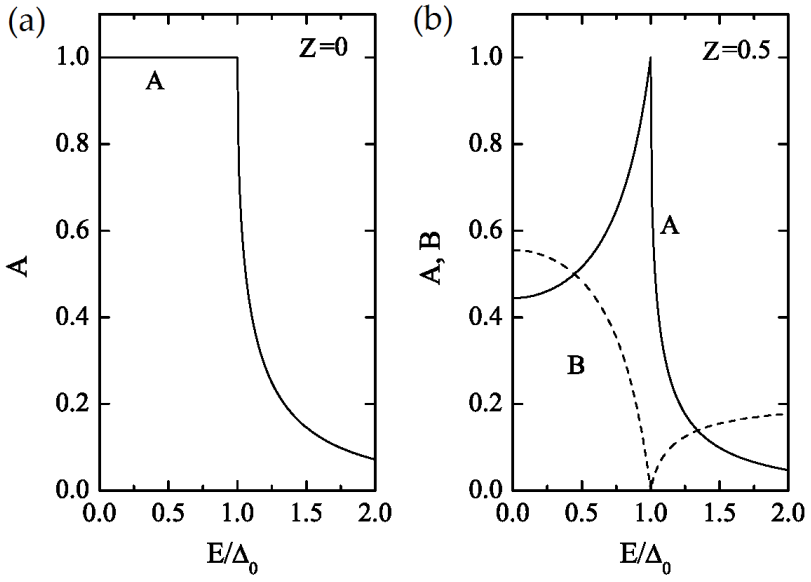

Figure 1.5: (a) Andreev reflection coefficient A as a function of E/Δ_0 for $Z = 0$. (b) Andreev reflection coefficient A and normal reflection coefficient B for $Z = 0.5$. Adapted from [3].

For an incident hole, the reflection and transmission coefficients a_-, b_-, c_- and d_- are obtained from the coefficients calculated for the electrons by replacing Z with $-Z$, i. e., $a_-(Z) = a_+(-Z)$. On the other hand, if electron-like or hole-like quasi-particles are injected in the normal conductor, the corresponding coefficients are:

$$c'_\pm = c_\pm(u_0^2 - v_0^2)/r, \tag{1.25}$$

$$d'_\pm = d_\pm(u_0^2 - v_0^2)/r. \tag{1.26}$$

This set of coefficients will be used in section 1.4 to calculate the supercurrent in a S-2DEG-S junction.

The electrical current $I_S(V)$ flowing through the N/S interface is calculated from the probability currents [22]. Since the current must be conserved, it is sufficient to consider only the contributions of the normal side:

$$I_S(V) = \frac{ek_{FN}W}{\pi^2\hbar}\int_{-\infty}^{\infty}[f_0(E+eV) - f_0(E)][1 + A(E) - B(E)]dE. \tag{1.27}$$

Here, f_0 is the equilibrium Fermi distribution function, V is the voltage drop at the interface and W is the contact width. The Andreev reflection probability is defined as $A(E) = a_+^* a_+$, whereas the normal reflection process is expressed by $B(E) = b_+^* b_+$. The trends of A and B for two values of Z are plotted in Fig. 1.5. In the case of ideal interfaces, the Andreev reflection probability is equal to 1 for $E \leq \Delta_0$, since no other scattering process is permitted, as explained in section 1.2.1. If a potential barrier with $Z > 0$ is introduced, A is reduced while the

normal reflection probability B is increased.
It is worth noting that Andreev reflection increases the total current and, therefore, the conductance of the junction, as it was already mentioned in section 1.2.1. This contribution leads to the so-called *excess current* I_{exc}, which can be defined as:

$$I_{exc} \equiv (I_S - I_N)|_{eV \gg \Delta_0}, \tag{1.28}$$

where $I_N = V/R_N$ is the normal current for $V \gg \Delta_0/e$ and R_N is the normal-state resistance of the N/S junction. I_N can be calculated from Eq. 1.27 by setting $A = 0$ and $1 - B = \mathcal{T} = 1/(1 + Z^2)$:

$$I_N = \frac{2e^2 k_{FN} W}{\pi h} \frac{V}{1 + Z^2} = \frac{V}{R_N}. \tag{1.29}$$

Thus, the explicit expression for the excess current is given by:

$$I_{exc} = \frac{1}{eR_N\mathcal{T}} \int_0^\infty [1 + A(E) - B(E) - \mathcal{T}]dE. \tag{1.30}$$

As it will be explained in section 1.5, from the experimental value of I_{exc} we can estimate the value of the Z parameter and, consequently, of the junction transmissivity $\mathcal{T}$.
The normal conducting part of the devices under investigation is constituted by a semiconductor heterostructure, containing a 2DEG. In the next section, we will introduce the main properties of the 2DEG.

1.3 Two-dimensional electron gases (2DEGs)

A system of electrons whose motion is confined in one spatial direction, but free to move in the perpendicular plane, constitutes a 2DEG.
One of the simplest way to produce a spatial confinement is through a Quantum Well (QW) potential. If we consider a one-dimensional particle with mass m trapped in an infinite square well potential with width L, it can only occupy discrete energy levels [24]:

$$E_n = \frac{\hbar^2 \pi^2}{2mL^2} n^2 \qquad \text{with } n = 1, 2, ... \tag{1.31}$$

Cooling the system to a temperature $k_B T < E_2 - E_1$ will force the particle to occupy the ground state ($n = 1$). In this way, the dynamics of the particle will be effectively blocked in the well direction.
For the most used III-V semiconductors, such as Gallium Arsenide (GaAs), Aluminium Arsenide (AlAs), Indium Arsenide (InAs) and their alloys, electron states near the minimum of the conduction band (CB) can be well described

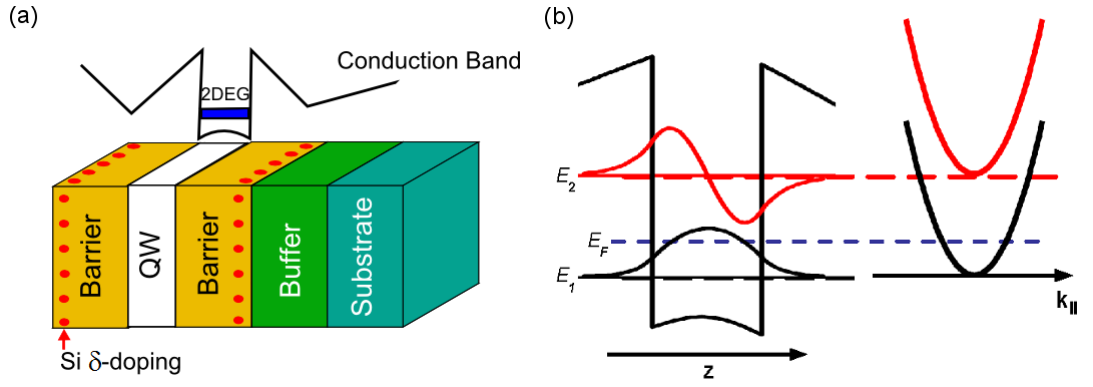

Figure 1.6: Realization of a 2DEG in a semiconductor heterostructure. (a) Schematic illustration of the layered structure of a modulation-doped QW; the black curve is the spatial profile of the bottom of the CB through the sample. In the left part of (b), the CB potential well and its lowest two confined energy states (E_1, E_2) with the corresponding envelope wave function profiles are shown along the growth direction (z). The right part represents the subbands associated with each of the levels. Here the Fermi level E_F (dashed horizontal line) lies in the lowest subband. Re-elaborated from [26].

as free particles with an effective mass m^* smaller than the electron mass (for GaAs $m^* = 0.067m_e$, for AlAs $m^* = 0.124m_e$ and for InAs $m^* = 0.023m_e$). In the presence of an interface between two different materials, these electrons "perceive" an effective potential described by the spatial profile of the band edge. This fact is explained rigorously by the Envelope Function Formalism [25].
More practically, a QW can be created by sandwiching a thin layer of lower band gap materials (well) within two layers of higher band gap materials (barriers). As a first approximation, the well is a rectangular potential profile whose width is the thickness of the low band gap material, and whose depth is given by the conduction/valence band offsets (for electrons and holes, respectively) between the well and the barrier materials. This is shown in Fig. 1.6(a).
It is important to understand that since the motion is confined only in one dimension (z), electrons will be free to move in the plane perpendicular to the well. Therefore the in-plane Bloch wave vector $\mathbf{k}_\parallel$ remains a good quantum number and each confined level gives rise to a subband with in-plane parabolic dispersion:

$$E_n(\mathbf{k}_\parallel) = E_n + \frac{\hbar^2 \mathbf{k}_\parallel^2}{2m^*}, \tag{1.32}$$

as illustrated in Fig. 1.6(b). Electrons occupy the lowest subbands depending on their density and on the value of temperature.
In order to obtain a 2DEG, the QW must be n-doped. This condition is necessary, since near $T = 0\ K$ semiconductors are insulating. Silicon impurities are

commonly used as donors in III-V semiconductors. In proper conditions, they can replace an atom of the third group and easily donate the additional electron in their outer shell. On the other hand, Si-impurities in the well layer produce potential fluctuations in space, which can scatter electrons and reduce their mobility.

This problem was solved at the end of the 1970's, when modulation-doping [27] and δ-doping [28] techniques were introduced for the first time. These methods consist in creating the donor region in the barrier layer, with a δ-like spatial profile along the growth direction. In this way, if the doping region is sufficiently close to the well, the additional electrons are able to reach the QW, but the scattering mechanisms introduced by the Si-impurities will be suppressed, since the donor ions are not in the well layer. As a result, mobilities over $10^6\ cm^2/Vs$ and mean free paths l_e on the order of tens of microns or more can be achieved at low temperatures. These parameters usually satisfy the *clean* (or *ballistic*) limit conditions:

$$l_e = \frac{\hbar\mu}{e}\sqrt{2\pi n_{2D}} \gg \xi_N = \frac{\hbar v_F}{2\pi k_B T}, \tag{1.33}$$

where n_{2D} is the charge density of the 2DEG, ξ_N is the coherence length, v_F is the Fermi velocity, T is the temperature and k_B is the Boltzmann's constant.

When electron confinement is created along one of the directions in the 2DEG plane (for instance, with another QW in the y direction), each subband of the QW in the z direction splits into one-dimensional parabolic subbands:

$$E_{n,l}(k_y) = E_n + E_i + \frac{\hbar^2 k_x^2}{2m^*}, \tag{1.34}$$

where n and l are subband indexes for the z and y directions, respectively. k_x represents the x-component of the Bloch wavevector. It can be demonstrated [29] that each subband contributes to the electric transport in the x direction with a quantum of conductance:

$$G_0 = \frac{2e^2}{h}, \tag{1.35}$$

where e is the electric charge of the electron and the factor 2 takes into account the spin degeneracy of each subband. In a Quantum Point Contact (QPC) formalism, these subbands give rise to quantized "conductance channels". This phenomenon will be discussed in detail in section 2.1.

1.4 Josephson current in S-2DEG-S junctions

In Section 1.2, the phase of the pair potential Δ_0 in the superconductor was neglected. However, the phase coherence between the superconducting electrodes

is essential for the occurrence of a supercurrent in a Josephson junction.
In the clean limit case ($\xi_N < l_e$), it was shown [30] that two contributions are responsible for generating a Josephson current: one is due to discrete energy levels, which are formed within the superconductor gap; the other comes from the continuous energy spectrum at $|E| > \Delta_0$.
In the following, we will introduce a basic model for an ideal one-dimensional S-N-S junction, then we will be rapidly generalize it to the case of non-ideal interfaces. Finally, we will discuss the model by Chrestin, Matsuyama and Merkt (CMM) [31] for a non-ideal S-2DEG-S junction, providing explicit expression for the Josephson current as a function of the 2DEG charge density, the strength of the potential barrier at the interfaces, the junction length and temperature.

1.4.1 Andreev energy levels in an ideal S-N-S junction

The basic principles of non-dissipative transport through an ideal one-dimensional S-N-S junction were first introduced by Kulik [30] in 1969. The model assumes ideal N/S interfaces: neither potential barriers nor Fermi velocity mismatches are considered. Similarly to the BTK model [22], a step-like pair potential $\Delta(x)$ is assumed, but now a phase difference ϕ between the superconducting leads is present, as shown in Fig. 1.7:

$$\Delta(x) = \begin{cases} \Delta_0 e^{-i\phi/2} & \text{for } x < 0, \\ 0 & \text{for } 0 < x < L, \\ \Delta_0 e^{i\phi/2} & \text{for } x > L. \end{cases} \tag{1.36}$$

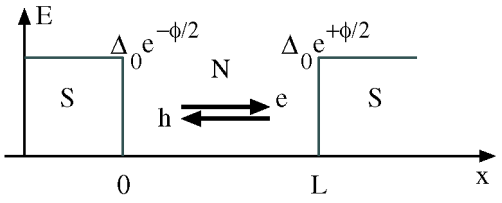

Figure 1.7: Schematic drawing of an ideal one-dimensional S-N-S junction. A step-like pair potential $\Delta(x)$ is assumed. The arrows indicate the direction of the group velocities of electrons and holes. Adapted from [3].

The solutions of the BdG equations for this problem can be divided in a continuous Andreev spectrum for $|E| > \Delta_0$ and in discrete Andreev states for $|E| \leq \Delta_0$. The latter are due to the fact that there are no available states within the superconductor gap. As mentioned in section 1.2.2, in this region the wave functions decay exponentially. This energy configuration is similar to a finite-depth quantum well for electrons, with discrete states within and continuous states outside

the well. Yet, in the S-N-S junction case, the barriers "contain" a condensed ground state and the discrete states can carry a supercurrent by means of Andreev reflections.

Kulik's ansatz for the wave functions $\psi_\pm$ of an excitation moving to the right $(+)$ or to the left $(-)$ with an energy $E \leq \Delta_0$ can be written as [3]:

$$\psi_+(x) = \begin{cases} A_+ \begin{pmatrix} v_0 e^{-i\phi/2} \\ u_0 \end{pmatrix} e^{i\tilde{k}_h x} & \text{for } x < 0, \\ B_+ \begin{pmatrix} v_0 e^{-i\phi/2} \\ 0 \end{pmatrix} e^{ik_e x} + B_+ \begin{pmatrix} 0 \\ u_0 \end{pmatrix} e^{ik_h x} & \text{for } 0 < x < L, \\ C_+ \begin{pmatrix} u_0 e^{i\phi/2} \\ v_0 \end{pmatrix} e^{i\tilde{k}_e (x-L)} & \text{for } x > L, \end{cases} \tag{1.37}$$

and as

$$\psi_-(x) = \begin{cases} A_- \begin{pmatrix} u_0 e^{-i\phi/2} \\ v_0 \end{pmatrix} e^{-i\tilde{k}_e x} & \text{for } x < 0, \\ B_- \begin{pmatrix} u_0 e^{-i\phi/2} \\ 0 \end{pmatrix} e^{-ik_e x} + B_- \begin{pmatrix} 0 \\ v_0 \end{pmatrix} e^{-ik_h x} & \text{for } 0 < x < L, \\ C_- \begin{pmatrix} v_0 e^{i\phi/2} \\ u_0 \end{pmatrix} e^{-i\tilde{k}_h (x-L)} & \text{for } x > L. \end{cases} \tag{1.38}$$

The wave vectors k_e, k_h, $\tilde{k}_e$ and $\tilde{k}_h$ were defined in Eqs. 1.15 - 1.18. For the ideal case, as considered here, the Fermi wave vectors in the superconductor and in the normal conductor are assumed to be identical: $k_{FN} = k_{FS} = k_F$. If the boundary conditions are imposed at $x = 0$ and $x = L$, the following result is obtained by using the definitions (1.4, 1.5) of u_0 and v_0:

$$\frac{u_0^2}{v_0^2} = \frac{2E^2 - \Delta_0^2}{\Delta_0^2} + i2\frac{E}{\Delta_0^2}\sqrt{\Delta_0^2 - E^2} = e^{\pm i\phi} e^{i(k_e - k_h)L}, \tag{1.39}$$

where $+i\phi$ corresponds to the right-moving quasi-particles and $-i\phi$ to the left-moving quasi-particles. When $|E| \leq \Delta_0$ the absolute value of u_0^2/v_0^2 is equal to 1, thus it is possible to define $u_0^2/v_0^2 = exp(i2\gamma)$. Then, for $|E| \ll \mu$, $(k_e - k_h)$ can be approximated by $k_F E/\mu = E/(\Delta_0 \xi_0)$, where $\xi_0 = \mu/(k_F \Delta_0)$ is the BCS coherence length. By inserting these equations in Eq. 1.39, one can determine

the energy eigenvalues:

$$\left(\frac{E}{\Delta_0}\right)\left(\frac{L}{\xi_0}\right) = 2\arccos\left(\frac{E}{\Delta_0}\right) \mp \phi + 2\pi n, \tag{1.40}$$

with $n = 0,\ \pm 1,\ \pm 2,\ ....$ Two typical eigenvalue spectra are shown in Fig. 1.8, in the short-junction limit ($L \ll \xi_0$) [Fig. 1.8(a)] and in the long-junction limit ($L \gg \xi_0$) [Fig. 1.8(b)]. Similarly to the eigenvalues for electrons in a quantum well, the number of states increases with L, while the energy separation between adjacent levels is reduced. In the case of a long junction, the energy dispersion at low energies ($E \ll \Delta_0$) is approximately linear:

$$E_n^{\pm} = \frac{\xi_0 \Delta_0}{L}[\pi(2n+1) \mp \phi]. \tag{1.41}$$

In the next section, we will determine the contribution of these level to the supercurrent, together with the part that comes from the continuum with $|E| > \Delta_0$.

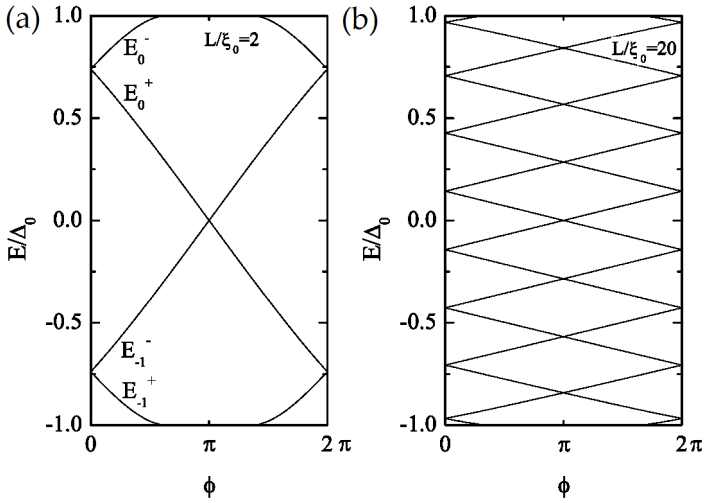

Figure 1.8: Andreev levels of an ideal S-N-S junction in the short (a) and long (b) limit. Adapted from [3].

1.4.2 Supercurrent in a general S-N-S junction

If a δ-shaped potential barrier at the interfaces and a velocity mismatch between normal conductor and superconductor are introduced, the Andreev levels and the supercurrent can be calculated by a transfer matrix method [32]. Here, the main features of the model will be qualitatively described and only the main results will be discussed.

The starting point of this approach is the following equation:

$$\begin{pmatrix} \tilde{\Psi}_e \\ \tilde{\Psi}_h \end{pmatrix} = \mathbf{T}(E,\phi) \begin{pmatrix} \Psi_e \\ \Psi_h \end{pmatrix}, \tag{1.42}$$

where $\tilde{\Psi}_e$ and $\tilde{\Psi}_h$ are the incoming electron-like and hole-like wave functions, whose transmission through the junction is described by a transfer matrix $\mathbf{T}(E,\phi)$ (E is the energy of the quasi-particles and ϕ is the phase difference between the superconducting electrodes).
$\mathbf{T}(E,\phi)$ is calculated by a product of several components, which take in account all the possible processes occurring in the junction. In fact, several different steps contribute to the transport and have to be considered: first, the transmission through the left (S/N) and right (N/S) boundaries are represented by two different matrices, which contain the transmission coefficients obtained by the BTK model (see Eqs. 1.23, 1.24, 1.25, 1.26). Then, a matrix that expresses the phase shifts of electrons and holes in the N region is introduced. Finally, two scattering matrices are used to describe Andreev and normal reflection at the S/N and N/S boundaries (where BTK coefficients $a_\pm$ and $b_\pm$ are employed).
In this way, the supercurrent flowing through the junction can be analytically expressed by two contributions: one is due to the discrete Andreev levels $E_n^\pm$ and the other comes from the continuous states with $|E| > \Delta_0$. At zero temperature only the discrete levels below the chemical potential μ are occupied, therefore the former contribution can be expressed as [3]:

$$I_{dis} = \sum_{n,\pm,E<0} \frac{2e}{\hbar} \frac{dE_n^\pm(\phi)}{d\phi}. \tag{1.43}$$

The energy eigenvalues $E_n^\pm$ are numerically calculated from the poles of $\mathbf{T}(E,\phi)$. On the other hand, the current carried by the continuous states is:

$$\begin{aligned} I_{cont} &= \frac{2e}{\hbar} \int_{-\infty}^{-\Delta_0} i(E,\phi) dE \\ &= \frac{2e}{\hbar} \int_{\infty}^{-\Delta_0} \frac{1}{|u_0^2 - v_0^2|} \{ [T^e_{L\to R}(E,\phi) - T^e_{L\leftarrow R}(E,\phi)] \\ &- \left[T^h_{L\to R}(E,\phi) - T^h_{L\leftarrow R}(E,\phi)\right] \} dE, \end{aligned} \tag{1.44}$$

where the transmission coefficients $T^{e,h}_{L\leftrightarrow R}$ are obtained from the squared absolute values of $\mathbf{T}(E,\phi)$ diagonal elements. An example of the energy eigenvalue spectrum for different values of the barrier strength Z and Fermi velocity mismatch r is shown in Fig. 1.9(a). For $Z > 0$ and $r < 1$ an energy gap appears between the levels and the $E(\phi)$ dispersion is flattened. Because of this, the Josephson current due to the discrete levels is lowered in agreement with Eq. 1.43. In Fig. 1.9(b) the different contributions to the supercurrent are represented.

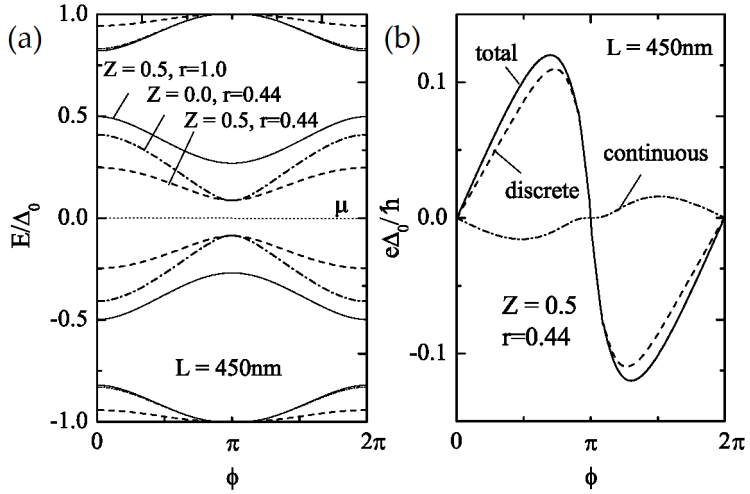

Figure 1.9: (a) Andreev levels for a 450-nm-long S-N-S junction with $Z = 0.5$, $r = 1$ (solid lines), $Z = 0$, $r = 0.44$ (dash-dotted lines) and $Z = 0.5$, $r = 0.44$ (dashed lines). (b) Contributions to the Josephson current of a 450-nm-junction with $Z = 0.5$ and $r = 0.44$. Adapted from [3].

At finite temperature the occupation of Andreev levels is determined by the Fermi distribution function $f_0(E)$, which modifies the expressions for the two parts of the supercurrent as follows:

$$I_{dis} = \sum_{n,\pm} \frac{2e}{\hbar} \frac{dE_n^{\pm}(\phi)}{d\phi} f_0(E_n^{\pm}(\phi)), \tag{1.45}$$

$$I_{cont} = \frac{2e}{\hbar} \left(\int_{-\infty}^{-\Delta_0} + \int_{\Delta_0}^{\infty} \right) i(E,\phi) f_0(E) dE. \tag{1.46}$$

The current direction of two adjacent levels is opposite. As the temperature is increased, the difference between the populations of these levels decreases. As a result the total supercurrent decreases with temperature. The same effect is obtained at constant temperature by increasing both L and, consequently, also the density of Andreev levels within the superconductor gap. In both cases, the reduction of the supercurrent has an exponential trend [3].

1.4.3 The Chrestin-Matsuyama-Merkt (CMM) model

In order to treat realistic S-2DEG-S junctions, the one-dimensional models introduced in the previous sections need to be extended to two-dimensional systems. This implies that electrons and holes in the 2DEG impinge at various angles onto the interface with the superconductor. Only the component of the wave vector normal to the interface is relevant for the phase-coherent transport processes described above. Therefore, at a given Fermi number, a complete spectrum of normal wave vector components will have to be taken into account. Moreover,

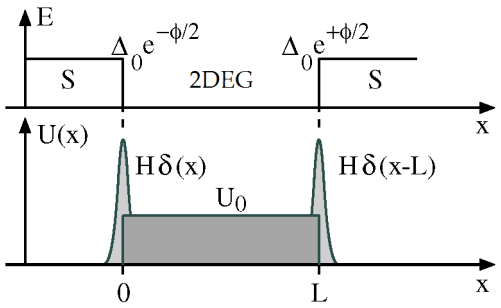

Figure 1.10: Spatial dependence of the pair potential $\Delta(x)$ and the potential $U(x)$ in the CMM model. Adapted from [3].

the properties of the 2DEG, such as the subband quantization, must be considered.

In 1993 Chrestin, Matsuyama and Merkt (CMM) [31] formulated a relatively simple model, which can describe the Josephson current flowing through a S-2DEG-S junction as a function of several parameters, such as the temperature T, the charge density in the 2DEG n_{2D} and the barrier strength Z. Along the transport direction (x) they assumed δ-shaped barriers at the interfaces and a potential step U_0 due to the Fermi velocity mismatch between the superconductor and the 2DEG (see Fig. 1.10):

$$U(x) = U_0[\Theta(x) - \Theta(x-L)] + \frac{\hbar^2 k_{FS}}{m_e} Z[\delta(x) + \delta(x-L)]. \tag{1.47}$$

Periodic boundaries were assumed along the other in-plane dimension (y), while a triangular well was introduced along z in order to simulate the confining potential of the 2DEG. As in the BTK model, the pair potential was supposed to be step-like.

The wave function defined in Eq. 1.37 was adapted to the subband structure of the 2DEG and boundary conditions were imposed. If a single subband is occupied in the 2DEG quantum well, the current per unit width flowing through the junction can be expressed as:

$$\langle i \rangle = -\frac{e k_B T}{\hbar} \sum_{\omega_n} \frac{1}{2\pi} \int_{-\infty}^{\infty} \frac{sin\phi}{(1/2)cos\phi + f(k_y, \omega_n)} dk_y, \tag{1.48}$$

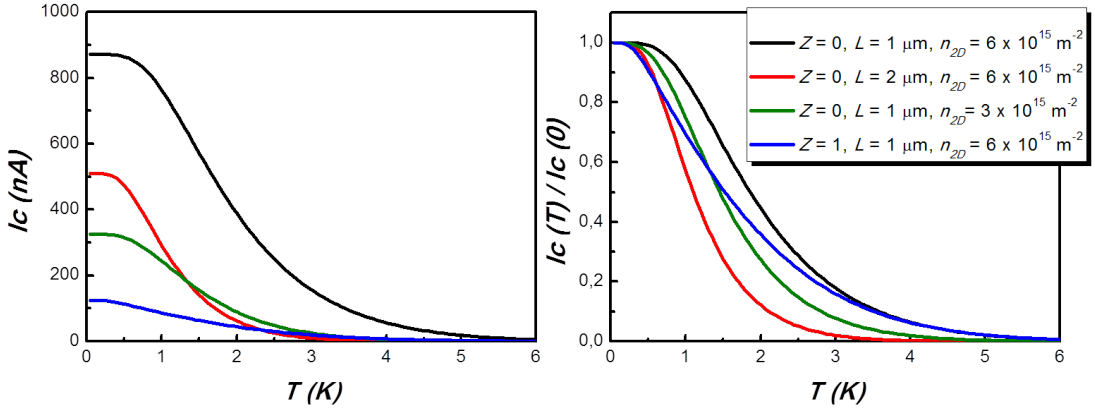

Figure 1.11: Calculated temperature dependence of the maximum supercurrent I_C for $Z = 0$, $L = 1\ \mu m$ and $n_{2D} = 6{\cdot}10^{15}\ m^{-2}$ (black), $Z = 0$, $L = 2\ \mu m$ and $n_{2D} = 6{\cdot}10^{15}\ m^{-2}$ (red), $Z = 0$, $L = 1\ \mu m$ and $n_{2D} = 3 \cdot 10^{15}\ m^{-2}$ (green), $Z = 1$, $L = 1\ \mu m$ and $n_{2D} = 6 \cdot 10^{15}\ m^{-2}$ (blue). The currents are plotted in absolute values (left) and normalized values (right). The width of the junction is $W = 800\ nm$ and the superconductor gap $\Delta_0 = 1.2\ eV$. $I_C(0)$ is the zero-temperature critical current.

where ϕ is the phase difference between the superconducting electrodes, $f(k_y, \omega_n)$ is given by:

$$f(k_y,\omega_n) = \eta_1^- e^{i(k^+-k^-)L} + \eta_1^+ e^{-i(k^+-k^-)L} - \eta_2^- e^{i(k^++k^-)L} - \eta_2^+ e^{-i(k^++k^-)L}, \tag{1.49}$$

$$\eta_1^\pm = \frac{1}{16}\frac{\sigma^2p^2}{k^+k^-}\left\{\frac{\Omega_n}{\Delta_0}\left[1+\left(2Z\frac{k_{FS}}{p}\right)^2+\frac{k^+k^-}{\sigma^2p^2}\right] \pm\left(\frac{\omega_n}{\Delta_0}\frac{k^++k^-}{\sigma p}-2iZ\frac{k_{FS}}{p}\frac{\Omega_n}{\Delta_0}\frac{k^+-k^-}{\sigma p}\right)\right\}^2 \tag{1.50}$$

and

$$\eta_2^\pm = \frac{1}{16}\frac{\sigma^2p^2}{k^+k^-}\left\{\frac{\Omega_n}{\Delta_0}\left[1+\left(2Z\frac{k_{FS}}{p}\right)^2-\frac{k^+k^-}{\sigma^2p^2}\right] \pm\left(\frac{\omega_n}{\Delta_0}\frac{k^+-k^-}{\sigma p}-2iZ\frac{k_{FS}}{p}\frac{\Omega_n}{\Delta_0}\frac{k^++k^-}{\sigma p}\right)\right\}^2. \tag{1.51}$$

Here, $\sigma = m^*/m_e$ and $p = (k_{FS}^2 - k_y^2)^{1/2}$ represents the wave vector component in the superconductor normal to the interface. The energy is expanded in discrete Matsubara frequencies $\omega_n = (2n+1)\pi k_B T$ by means of analytic continuation $E + i\delta \to i\omega_n$ and Ω_n is defined as $\sqrt{\omega_n^2 + \Delta_0^2}$. The wave vector $k^\pm$ within the semiconductor is:

$$k^\pm = \sqrt{k_{FN}^2 - k_y^2 \pm i\frac{2m^*}{\hbar^2}\omega_n}, \tag{1.52}$$

where $k_{FN} = \sqrt{(2m^*/\hbar^2)(\mu - U_0 - E_0)}$ is the Fermi wave vector in the semiconductor and E_0 is the energy level of the first subband in the 2DEG.
From Eq. 1.48 we have numerically calculated the dependence of the maximum supercurrent I_C on T by setting $\phi = \pi/2$. Figure 1.11 shows four examples of the curves obtained for different values of Z, n_{2D} and L. The parameter values were chosen on the basis of the experimental characteristics of the devices which will be investigated in chapter 5. It can be noted that the absolute value of $I_C(0)$ is influenced by all the considered parameters, while the decay rate is mainly determined by L and n_{2D}.

1.5 Dissipative state of S-2DEG-S junctions

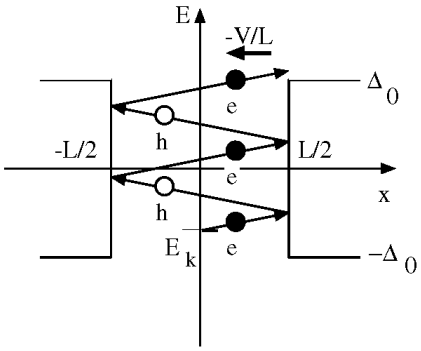

Figure 1.12: Schematic drawing of Multiple Andreev Reflection (MAR) process for an S-2DEG-S junction with ideal interfaces. Electrons e and holes h are accelerated by an external electric field $\mathbf{E} = -\mathbf{e}_x V/L$. As long as the particle energy is within the gap $\pm\Delta_0$, Andreev reflection occur at the S/2DEG interfaces. Adapted from [3].

The basic method used to characterize S-2DEG-S junctions is to measure the current-voltage characteristic. Above a critical current I_C, the system switches into a voltage-carrying state. At voltages above $V_A = 2\Delta_0/e$ Andreev reflection processes are no longer effective, therefore it is possible to measure the normal-state resistance R_N. For $|V| < V_A$ subharmonic gap structures can be observed. The latter are differential conductance peaks occurring at:

$$V_n = \frac{2\Delta_0}{en} \qquad \text{with } n = 1,\ 2,\ 3\ ..., \tag{1.53}$$

and they are due to Multiple Andreev Reflections (MARs) between the two S/2DEG interfaces. This process is schematically depicted in Fig. 1.12.
In the case of ideal interfaces, an electron in the 2DEG with initial energy E_k is accelerated by the applied voltage towards the boundary with the superconductor. There it is Andreev reflected as a hole, which is also accelerated by the external electric field. Then these steps are repeated until the particle in the 2DEG is

able to gain enough energy to enter the superconductor in a quasi-particle state above Δ_0. The path represented in Fig. 1.12 can also be taken in the opposite direction by particles moving against the field. If the applied field is decreased, more Andreev reflection will be necessary to gain or lose enough energy before the particles can be transmitted to the superconductors. This picture is a bit complicated if we introduce potential barriers at the interfaces. In this case, normal reflections will occur even for $|E| < \Delta_0$. In 1983 Octavio, Tinkham, Blonder and Klapwijk (OTBK) [33] formulated a model which was able to describe MARs in a ballistic S-N-S junction with a Boltzmann-equation approach.

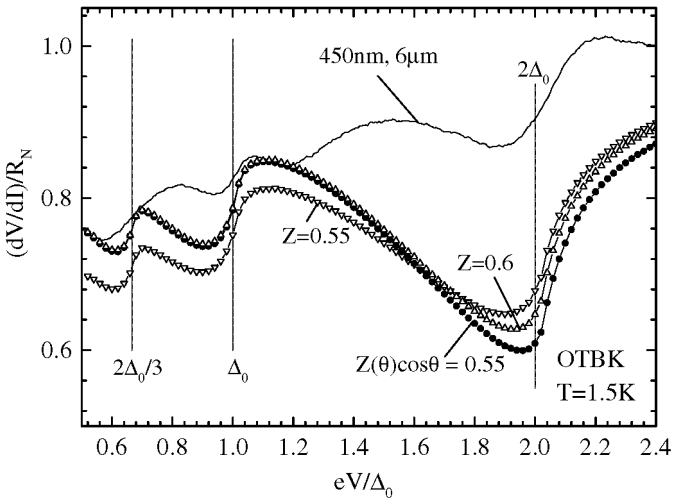

Figure 1.13: Normalized differential resistance (solid line) of a 450-nm-long and 6-µm-wide S-2DEG-S junction as a function of eV/Δ_0 at 1.5 K. The symbols $\triangle$, $\triangledown$ and $\bullet$ represent the theoretical curves obtained from the OTBK model for different values of Z. The dips due to MARs are clearly visible at $V = V_n$. R_N is the normal-state resistance of the junction. Adapted from [3].

Figure 1.13 compares the measured differential resistance of a 450-nm-long and 6-µm-wide S-2DEG-S junction to the theoretical characteristics obtained from the OTBK model for different values of Z. Even though the experimental and the theoretical curves do not perfectly match, the resistance dips at $V = V_n$ are well-reproduced.

Using this method, Flensberg *et al.* [34] numerically calculated the dependence of the excess current I_{exc} on the barrier strength parameter Z, as shown in Fig 1.14. This result will be used to determine the Z parameter of the investigated junctions.

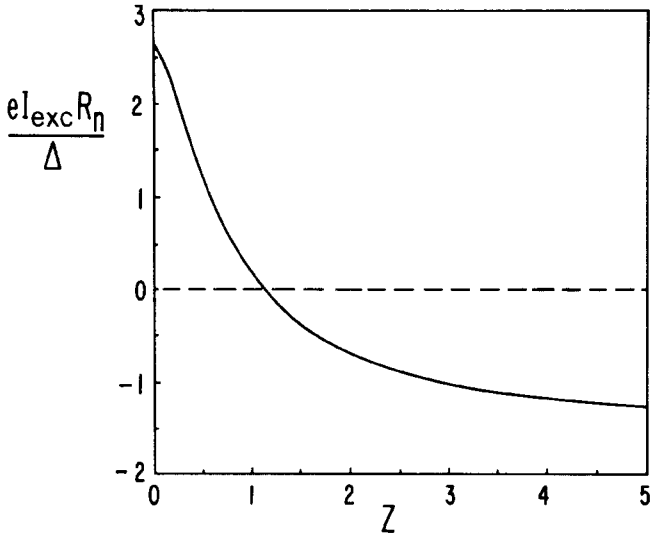

Figure 1.14: Plot of normalized excess current as a function of the barrier strength parameter Z. R_n is the junction normal-state resistance and Δ is the superconductor gap. The curve was calculated by using the OTBK model at $T = 0\ K$, but the temperature dependence is totally contained in the gap function Δ in the normalization factor. Therefore the plot can be used for a comparison with the experimental results. Adapted from [34].

Chapter 2

Quantum point contacts and quantum rings

The main goal of the thesis is the investigation of the electron transport phenomena in nanofabricated S-2DEG-S Josephson junctions, with two particular designs of the normal conducting region: a quantum point contact and a quantum ring. First, we fabricated and measured normal preliminary devices, in order to test the fabrication procedure and the 2DEG properties. Then, we replaced the normal contacts with superconducting leads, thereby fabricating hybrid Josephson junctions. In this chapter, we will present a brief review of available results present in literature for Normal Quantum Point Contacts (NQPCs) (section 2.1), Normal Quantum Rings (NQRs) (section 2.2), S-QPC-S (section 2.3) and S-QR-S junctions (section 3.9). The basic physical principles will be discussed as well as the more detailed models for the hybrid systems.

2.1 Normal Quantum Point Contacts (NQPCs)

A Quantum Point Contact (QPC) is a narrow constriction between two wide electrically-conducting regions, of a width comparable to the electronic Fermi wavelength. The first studies of metallic QPCs date back to 1960's [35] and yielded the first observation of ballistic transport. However, the quantum-mechanical character of the electron transport became evident only when QPCs were created in semiconductor heterostructures. In 1988 van Wees *et al.* [6] and Wharam *et al.* [7] independently realized a QPC in a GaAs/AlGaAs 2DEG and observed the quantization of its conductance. Following the split-gate technique developed in the 1980's [36], they evaporated two metallic gates on top of the heterostructures and created a 250-300-nm-wide point contact. By applying a negative voltage to the gates, they could deplete the 2DEG until the conduction

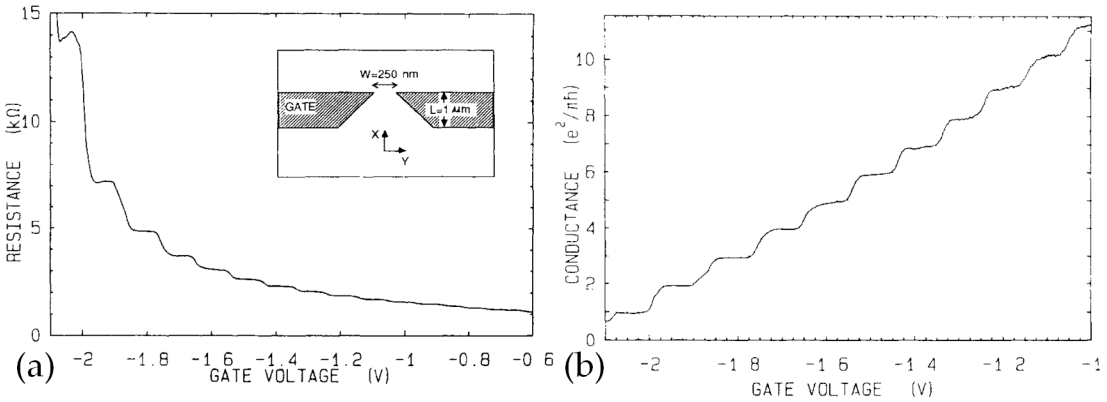

Figure 2.1: Plot of the QPC resistance (a) and conductance (b) versus the applied gate voltage. Up to sixteen plateaus are visible when the gate voltage is varied from -0.6 V (depletion of the 2DEG below the gates) to -2.2 V ("pinch-off"). The conductance is obtained from the data of (a) after subtracting the lead resistance. The inset in (a) shows the schematic drawing of the split-gates which define the QPC. Adapted from [6].

took place through the QPC only. A further decrease of the gate voltage gradually reduced the width W of the QPC, until the depopulation was complete and no current flowed (the QPC "pinched off"). The effectiveness of the split gates is based on the Schottky barrier which originates at the metal/GaAs interface, avoiding current leakages from the gates to the 2DEG. The measured resistance and conductance showed several plateaus, as represented in Fig. 2.1. The observed conductance steps are multiples of the conductance quantum $G_0 = 2e^2/h$ defined in Eq. 1.35.

This behaviour can be understood within the formalism developed by Landauer [37] and then extended by Büttiker and Imry [29]. As already mentioned in section 1.3, when the electron motion in a 2DEG is confined in a transverse direction (y), the y-component of the Bloch wave vector becomes quantized in $k_y = \pm i\pi/W$ ($i = 1,\ 2,\ ...$). Therefore, the two-dimensional subbands defined in Eq 1.32 split into one-dimensional subbands given by Eq. 1.34. According to the Landauer-Büttiker model, the two terminal conductance of N independent ballistic channels is given by:

$$G = \frac{2e^2}{h} \sum_{i=1}^{N} T_i, \tag{2.1}$$

where T_i is the transmission coefficient of the i-th channel. Under the assumption of ballistic transport with no channel mixing (the electron mean free path l_e must be $\gg W$ and the Fermi wave length λ_F must be $\ll W$), T_i can be taken equal to one. If the confining potential is approximated as a square well, the number N of channels in the QPC is obtained by comparing the discrete energy

levels in the y direction with the 2DEG Fermi energy:

$$N = k_F W/\pi, \tag{2.2}$$

where k_F is the Fermi wave number of the 2DEG [6].
The conductance quantization effect fades away as the temperature is increased. Backscattering due to random inhomogeneities and boundary roughness introduces deviations from the ideal behaviour, causing the transmission coefficient T_i to be less than one. On the other hand, conductance quantization proved to be quite independent from the shape of the confining potential: sharp constrictions exhibit conductance plateaus as well as smooth ones do [38].
As it will be explained in chapter 3, all the devices that we investigated in this thesis work are based on a InAs/$In_{0.75}Ga_{0.25}As$ quantum well with $In_{0.75}Al_{0.25}As$ barriers. The external layer of the heterostructure consists of $In_{0.75}Ga_{0.25}As$. It was shown that InAs [39] and $In_xGa_{1-x}As$ with $x > 0.75$ [40] do not form Schottky barriers at the interface with metals. This property is essential for creating highly-transmissive S-N-S junctions, but it does not permit the use of split gates to control the carrier population in the 2DEG. Thus, we defined the gates in the 2DEG itself by means of dry etching [41]. The fabrication process will be accurately described in chapter 3.

2.2 Normal Quantum Rings (NQRs)

The Aharonov-Bohm (AB) effect is one of the most distinct physical phenomena which illustrates the importance of the quantum-mechanical phase [8, 9]. In the AB effect, a charged particle acquires a phase shift:

$$\phi = 2\pi e/h \int_\gamma \mathbf{A} \cdot d\mathbf{r} \tag{2.3}$$

from the electromagnetic vector potential $\mathbf{A}$ while travelling along the path γ. The existence of this phase shift can be verified, for instance, by measuring the current through a quantum ring (QR) in a uniform perpendicular magnetic field. The electrons travelling along right and left arms of the QR gain a relative phase shift:

$$\begin{aligned} \phi_r - \phi_l &= \frac{2\pi e}{h}\left(\int_{\gamma_r} \mathbf{A} \cdot d\mathbf{r} - \int_{\gamma_l} \mathbf{A} \cdot d\mathbf{r}\right) \\ &= \frac{2\pi e}{h}\int_S \mathbf{B} \cdot d\mathbf{s} \\ &= 2\pi\Phi/\Phi_{AB}, \end{aligned} \tag{2.4}$$

where the surface integral yields the magnetic flux Φ through the QR and $\Phi_{AB} = h/e$ is the AB magnetic flux quantum.
In 1985 Webb *et al.* [42] were able to fabricate submicron-diameter Au QRs. They measured the resistance of the devices as a function of the applied magnetic field and observed AB oscillations with period Φ_{AB}. Similar conductance oscillations were later found also in semiconductor rings [43, 44, 45, 41]. An example of the conductance G measured in a semiconductor ballistic ring [41] is shown in Fig. 2.2. The period of the oscillations ΔH is equal to 107 G, which is consistent with $\Phi_{AB}/(\pi r^2)$, where r=350 nm is the mean radius of the quantum rings shown in Fig. 2.2(d).

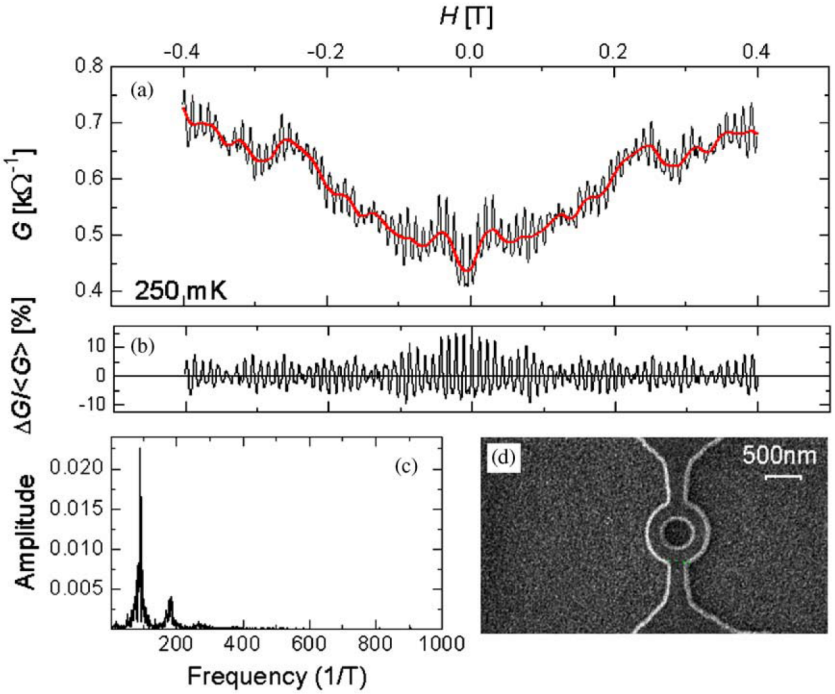

Figure 2.2: (a) Plot of the QR conductance G as a function of the external magnetic field, applied orthogonally to the QR plane. The AB oscillations have a period consistent with the expected Φ_{AB} and exhibit a contrast $\Delta G/G$ which can reach 20%, as represented in (b). (c) Fourier analysis shows the presence of other harmonics with smaller amplitudes (see text). (d) Scanning electron micrograph of a semiconductor QR. Adapted from [41].

Fourier analysis of the signal shows the presence of higher harmonics, at frequencies n/Φ_{AB}, with $n = 1,\ 2,\ ....$ In the case of a ballistic device, these higher frequencies are due to multiple transport loops in the ring: a part of the electron density does not flow out from the QR after travelling through one of the arms just once, but it continues to flow in the ring and can travel through n QR arms before exiting the ring or losing phase coherence. The contrast $\Delta G/G$ decreases with the width of the ring arm, because the overlap between electron

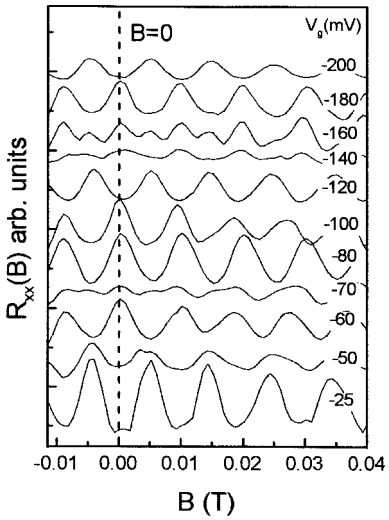

Figure 2.3: Plot of the QR resistance as a function of the external magnetic field for different values of the applied gate voltage. It is evident how the electrostatic potential can reduce the amplitude or invert the phase of the AB magnetic interference. Adapted from [48].

wave packets coming from different arms is reduced, together with the interference effect [46].

Semiconductor QRs were fabricated with different methods, such as wet etching [44], atomic force microscopy lithography [45] and dry etching [43, 41]. As already mentioned in the previous section, the latter approach is the most suited to InAs/$In_{0.75}Ga_{0.25}$As heterostructures. By using the dry etching technique it is also possible to define two side gates in the 2DEG, at a distance of few hundreds of nanometres from the QR arms. The side gates can be employed to investigate the electrostatic AB effect: the interference pattern can be changed effectively by varying the phase of the electron wave in one arm so that a phase difference is induced between both branches of the ring. This situation is realized experimentally if one gate is biased, while the other is kept at a fixed voltage. The additional phase $\Delta\alpha$ acquired along a path of length L_G is given by [47]:

$$\Delta\alpha = \frac{2\pi e}{h}\frac{L_G}{v_F}V, \tag{2.5}$$

under the assumption that electrons move with the Fermi velocity v_F for a time L_G/v_F under the influence of potential V. An exemple of the electrostatic effect is shown in Fig. 2.3. It is evident that the electrostatic potential can reduce the amplitude or invert the phase of the AB interference pattern. The applied gate voltage varies the Fermi velocity of the electrons in one of the ring arms, thereby creating an interference effect in the QR conductance. This phenomenon differs from the one generated in a QPC or in a field-effect transistor, where the con-

ductance of the device depends only on the charge density in the 2DEG and no interference effect is generated.

2.3 S-QPC-S junctions

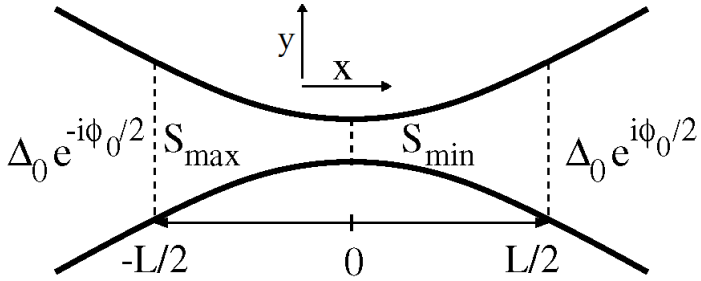

Figure 2.4: Schematic illustration of a constriction between two superconducting reservoirs. Adapted from [49].

Given the observation of conductance quantization in NQPCs, it is natural to ask whether it is possible to observe a quantization of the supercurrent if two superconducting electrodes are connected by a point contact. This problem was theoretically addressed by Beenakker and van Houten [49] and by Furusaki *et al.* [50]. The method used by Beenakker and van Houten, which applies to a short adiabatic constriction, will be discussed briefly.

The transmission through the constriction is assumed to be ballistic and no scattering between the transverse mode is considered. The geometry of the constriction is depicted in Fig. 2.4. It widens from a minimum width of S_{min} to $S_{max} \gg S_{min}$, at both sides. The length of the junction L is assumed to be much shorter than the coherence length $\xi_0 = \hbar v_F/\pi\Delta_0$, where Δ_0 is the superconductor gap. The pair potential at both ends of the constriction is approximated by $\Delta_0 \exp(-i\phi_0/2)$ for $x < -L/2$ and by $\Delta_0 \exp(i\phi_0/2)$ for $x > L/2$. Here ϕ_0 is the macroscopic phase difference between the superconducting reservoirs. Initially, no specific assumptions are made on the variation of $\Delta(x)$ in the narrow part of the constriction. In particular, the model also applies to a non-superconducting constriction with $\Delta_0(0) = 0$. The number of transverse modes (along the other in-plane direction y) propagating through the constriction is $N \simeq S_{min}/\lambda_F$. The BdG equations (Eq. 1.1) are solved by expanding the eigenfunctions $\psi = (u, v)$ into transverse modes φ_i:

$$\psi(\mathbf{r}) = \sum_i^N \begin{pmatrix} u_i(\mathbf{r}) \\ v_i(\mathbf{r}) \end{pmatrix} \varphi_i(\mathbf{r}), \tag{2.6}$$

where $\varphi_i(\mathbf{r})$ are the eigenfunctions of the one-electron Hamiltonian $-(\hbar^2/2m_e)$ $\partial^2/\partial y^2 + U(\mathbf{r})$ with eigenvalues $E_n(x)$. Here $U(\mathbf{r})$ is the confining potential of the constriction.

The WKB method [51] can be used in order to find solutions for the propagation along the constriction. It consists of substituting each vector (u_i, v_i) with

$$\begin{pmatrix} u(\mathbf{r}) \\ v(\mathbf{r}) \end{pmatrix} = \begin{pmatrix} e^{i\eta(x)/2} \\ e^{-i\eta(x)/2)} \end{pmatrix} \exp\left(i \int_0^x k(x')dx' \right), \tag{2.7}$$

into the BdG equations neglecting second-order derivatives (or product of first-order derivatives). The subscript i is omitted for notational simplicity. In general, the parameters $\eta(x)$ and $k(x)$ are complex. The WKB approximation requires that the pair potential varies smoothly along the constriction and its absolute value must be much smaller than $\mu - E_n(x)$, where μ is the chemical potential of the superconductor. Within this adiabatic frame, no Andreev reflections take place for $|E| > \Delta_0$. Thus, only discrete Andreev levels for $|E| < \Delta_0$ contribute to the Josephson current.

In the short-junction limit ($L/\xi_0 \to 0$), the Andreev bound-state energies defined in Eq. 1.40 can be written in a simple form:

$$\arccos(E/\Delta_0) = \pm\frac{1}{2}\phi_0. \tag{2.8}$$

This solution is independent from the precise behaviour of $\Delta(x)$ in the constriction. Moreover, the Andreev bound-state energy is identical for all the transverse modes i.

The normalized WKB wave function for the bound state of each mode is given by:

$$\begin{aligned} \psi_\pm = \left(\frac{m_e}{2\hbar^2}\right)^{1/2} (\Delta_0 - E^2)^{1/4} k_0(x)^{1/2} \begin{pmatrix} 1 \\ 1 \end{pmatrix} \\ \times \exp\left(\pm i \int_0^x k(x')dx' \right), \end{aligned} \tag{2.9}$$

where $k_0(x) = \{2m_e[\mu - E_n]/\hbar^2\}^{1/2}$, and

$$k(x) = k_0(x)\left[1 - \frac{i|\Delta(x)|}{2(\mu - E_n(x))}\text{sin}\phi(x)\right]. \tag{2.10}$$

Here, $\phi(x)$ is the superconducting phase within the constriction. In contrast to the one-dimensional model discussed in section 1.4.1, the wave vector does change along the constriction owing to the quantization in the transverse direction. The wave function of the bound state is ψ_+ for $0 < \phi_0 < \pi$ and ψ_- for

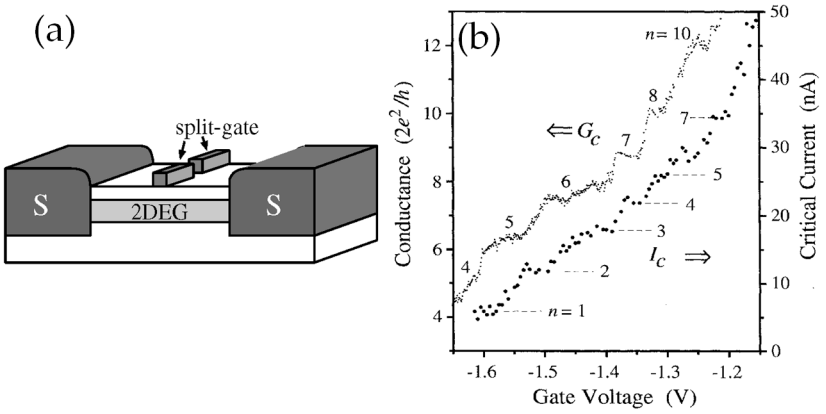

Figure 2.5: (a) Schematic drawing of a split-gate S-QPC-S junction. (b) Plot of the conductance and the critical current versus the gate voltage. Adapted from [4].

$-\pi < \phi_0 < 0$. Then, it is possible to calculate the Josephson current due to a single mode, which at $T = 0$ is:

$$I_i = \frac{e}{\hbar}\Delta_0 \sin(\phi_0/2). \tag{2.11}$$

Since all modes contribute by the same amount to the supercurrent, the critical current for N occupied modes is given by

$$I_C = N\frac{e\Delta_0}{\hbar}. \tag{2.12}$$

If the number of channels N increases, the critical current increases stepwise. The steps have a constant height $e\Delta_0/\hbar$, which does not depend on the specific characteristics of the junction. This result holds only for a short junction in the adiabatic approximation.

For the opposite case of a long ($L \gg \xi_0$) ballistic S-QPC-S junction, Furusaki *et al.* [50] extended the model by Beenakker and van Houten. They found that in the long-junction limit the quantization of the supercurrent is not any more universal but depends on the junction parameters. In 2000, Chtchelkatchev *et al.* [52] obtained a simple formula for the supercurrent step height by using a scattering matrix approach. Assuming ideal N/S interfaces and no Fermi velocity mismatch, they demonstrated the quantization of the supercurrent in units of $e/(\tau_0 + \hbar/\Delta_0)$. Here, τ_0 is the quasi-classical time of flight a quasi-particle requires to traverse the normal region of length L. During the time $\hbar/\Delta_0$ an electron wave packet is Andreev reflected into a hole wave packet. In the case of a transverse mode with transmission probability equal to one, the travel time can be approximated by $\tau_0 = L/v_F$ and the supercurrent is quantized at the non-universal value:

$$\Delta I_C = \frac{ev_F}{L + \pi\xi_0}. \tag{2.13}$$

If a finite barrier at the interfaces and a Fermi velocity mismatch are considered, the Andreev reflection probability is reduced and normal reflection has to be taken into account. In this case the expression of ΔI_C, according to Shchelkachev [53], is given by:

$$\Delta I_C = \frac{\mathcal{T} e}{4\pi\tau}. \tag{2.14}$$

Here, $\mathcal{T} = 1/(1+Z^2)$ is the normal-transmission probability through a N/S interface (Z is the BTK coefficient defined in Eq. 1.10) and:

$$\tau = \frac{\hbar}{\Delta_0} + \tau_0 \frac{1+\mathcal{R}}{\mathcal{T}}, \tag{2.15}$$

where $\mathcal{R} = 1 - \mathcal{T}$ is the normal-reflection probability from the potential barrier at the interfaces. Because of normal reflection, the residence time of quasi-particles in the 2DEG is increased by a factor $1 + \mathcal{R}/\mathcal{T}$ and the supercurrent carried by each transverse mode is reduced.
On the experimental side, the first S-QPC-S junctions were realized by Takayanagi *et al.* in 1995 [4]. A schematic drawing of the investigated devices is represented in Fig. 2.5(a). Two split gates were evaporated over a InAs 2DEG, which was contacted by two Nb leads. The distance L between the superconducting electrodes was 0.3 µm and their width was 10 µm. The measured conductance and Josephson current as a function of the gate voltage are plotted in Fig. 2.5(b). At 10 mK, the maximum critical current was I_C=1.8 µA with a quantization $\Delta I_C \simeq$5 nA. In 2005, Bauch *et al.* [5] confirmed these results in the same type of junctions.

If an external magnetic field is applied perpendicular to the plane of the S-2DEG-S junction, more detailed information about the Josephson current transport may be gained. Owing to the effect of the magnetic flux penetrating the junction, an interference pattern develops in the behaviour of the critical current versus magnetic field. In the simplest case, with a short junction, a regular Fraunhofer-like interference pattern is expected [2, 54]:

$$I_C = I_C^0 \left| \frac{\sin(\pi\Phi/\Phi_0)}{\pi\Phi/\Phi_0} \right|, \tag{2.16}$$

where I_C^0 is the critical current at zero magnetic field, Φ is the magnetic flux in the junction and $\Phi_0 = h/2e$ is the superconducting magnetic flux quantum. This result can be easily obtained by adding the field effect to the phase difference of the pair potential along the junction. Then, the Josephson current is integrated along the transverse direction, resulting in Eq. 2.16. A typical measurement of this interference pattern is shown in Fig. 2.6. Because of the planar geometry of

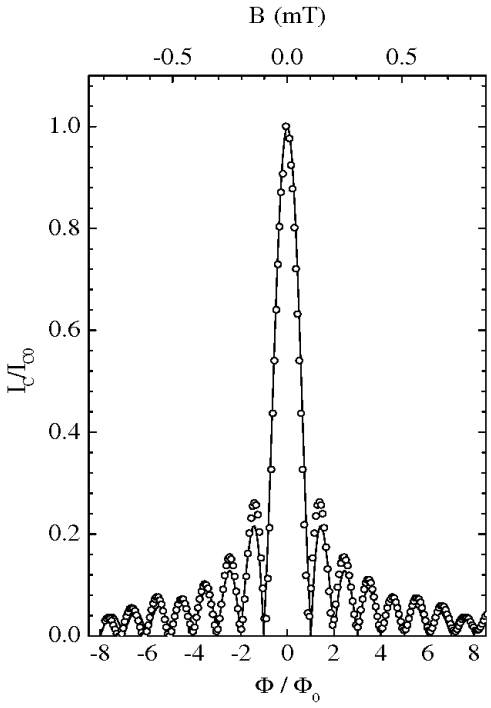

Figure 2.6: Plot of the normalized I_C at 0.5 K as a function of the magnetic field B for a 450-nm-long and 6-µm-wide S-2DEG-S junction. The circles are the experimental data whereas the full line is the Fraunhofer-like fit (Eq. 2.16). I_C^0 is the critical current at zero magnetic field and Φ_0 is the magnetic flux quantum. Adapted from [3].

the junctions, the external magnetic field can be focused into the semiconductor region owing to the shielding of the superconducting electrodes (Meissner effect). Experimentally, the focusing factor (B_{eff}/B_{ext}) can be obtained by matching the minima of the measured pattern with the corresponding multiples of Φ_0. A theoretical expression for the focusing factor was formulated by Gu *et al.* [55]:

$$(B_{eff}/B_{ext}) = (2W_S/L)^{2/3}, \tag{2.17}$$

where W_S is the width of the superconducting electrodes and L is the junction length.

In the last 15 years, the magnetic field dependence of I_C has been investigated also in S-2DEG-S junctions with a width W comparable to the length L. In this case, the period and the shape of the interference pattern are modified as functions of the L/W ratio. In 1998, Heida *et al.* [57] found that for $L/W \lesssim 1$ the period of the Fraunhofer-like pattern was consistent with $2\Phi_0$, taking into account the flux focusing by the electrodes. In 2009, Rohlfing *et al.* [56] analyzed the I_C dependence on the magnetic field for three different junctions with L/W= 0.3, 0.6 and 1.2. With the increase of the L/W ratio, they observed a clear transition from the standard Fraunhofer pattern to a monotonic decay of the critical current. This transition is shown in Fig. 2.7.

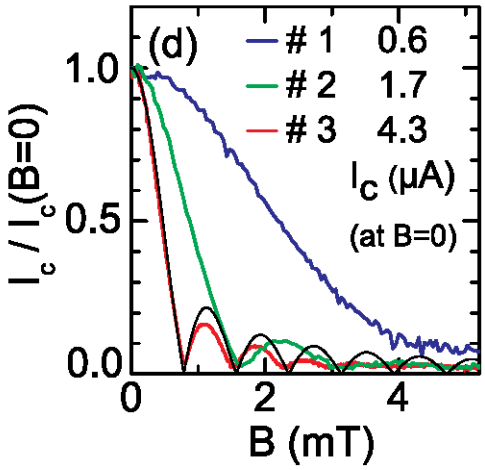

Figure 2.7: Normalized critical current I_C versus perpendicular magnetic field B for different widths W. Sample 1 has W_1=0.5 μm, sample 2 W_2=1 μm and sample 3 W_3=2 μm. All samples have a length L=0.6 μm. The black curve is the standard Fraunhofer pattern fitting the data of sample 3. Adapted from [56].

A qualitative model which can explain these results was proposed in 1999 by Barzykin and Zagoskin [11]. It is based on a quasi-classical description of the quasi-particles trajectories in the normal region of the S-2DEG-S junction. In contrast to the standard result (Eq. 2.16), which is obtained considering only trajectories perpendicular to the interfaces, when $W \lesssim L$ all the possible trajectories from one electrode to the other must be taken into account. The considered ballistic junction (represented in Fig. 2.8) is assumed to be in the limit $L \gg \xi_0$, with ideal N/S interfaces and totally absorbing lateral boundaries (at $y = \pm W/2$). The usual step-like approximation is used to describe the superconducting pair potential. If the Fermi wave-length λ_F of the 2DEG is much smaller than all other length scales, it is possible to apply the method of quasi-classical Green's functions [58], which can describe the trajectories of quasi-particles in the junction. When a perpendicular magnetic field is applied, the final expression for the critical current is:

$$I_C = \max_{0\leq\phi\leq 2\pi}\left\{\frac{ev_F}{W\lambda_F L}\int\int_{-W/2}^{W/2}\frac{2}{\pi}\frac{dy_1 dy_2}{\left[1+\left(\frac{y_1-y_2}{L}\right)^2\right]^{3/2}}\right.$$
$$\left.\times\sum_{k=1}^{\infty}(-1)^{k+1}\frac{L}{\xi_N\cos\theta_{y_1-y_2}}\frac{\sin k\left(\frac{\pi\Phi}{W\Phi_0}(y_1+y_2)+\phi\right)}{\sinh\frac{kL}{\xi_N\cos\theta_{y_1-y_2}}}\right\}. \qquad (2.18)$$

Here, v_F is the Fermi velocity of the 2DEG, $\xi_N = \hbar v_F/2\pi k_B T$ is the coherence length of the 2DEG in the ballistic limit and ϕ is the phase difference between the superconducting electrodes. Furthermore, $\theta_{y_1-y_2} = \arctan[(y_1-y_2)/L]$ is the

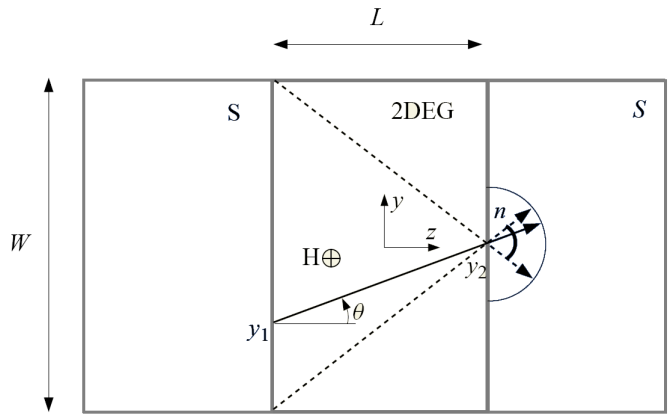

Figure 2.8: Schematic drawing of a ballistic S-2DEG-S junction. The magnetic field is applied perpendicular to the plane. One of the possible trajectories of the quasi-particles (solid line) is represented. Adapted from [11].

angle between the quasi-particle trajectory and the normal to the interfaces. The sum over k considers the contributions from quasi-classical "Andreev tubes" of width λ_F each. Every single contribution depends on the length of the trajectory and on the phase gained along it (because of Andreev reflections at the N/S interfaces and of the vector potential in the normal region). The double integration over y_1 and y_2 takes into account the non-local character of the transport through the junction: every trajectory allowed by the boundary conditions must be considered. From Eq. 2.18 we numerically calculated the I_C dependence on the magnetic flux for different values of the L/W ratio and temperature. Some relevant examples of the calculated curves are shown in Fig. 2.9. It can be seen that the minima move towards higher values of Φ/Φ_0 as L/W is increased; the opposite behaviour is obtained by raising the temperature, because the effective length of the junction $L_{eff} = \sqrt{L\xi_N}$ is reduced.

As it will be illustrated in chapter 3, we used two side gates near the junction in order to reduce both the number of occupied modes and the effective width of the 2DEG region [10]. Although this method offers the possibility to vary continuously the L/W ratio within the same junction, it has never been applied up to date. Moreover, the interference pattern can be measured at different temperatures in order to test the predictions by Barzykin and Zagoskin. The results of this innovative approach will be presented in chapter 5 and qualitatively compared to those obtained in Fig. 2.9.

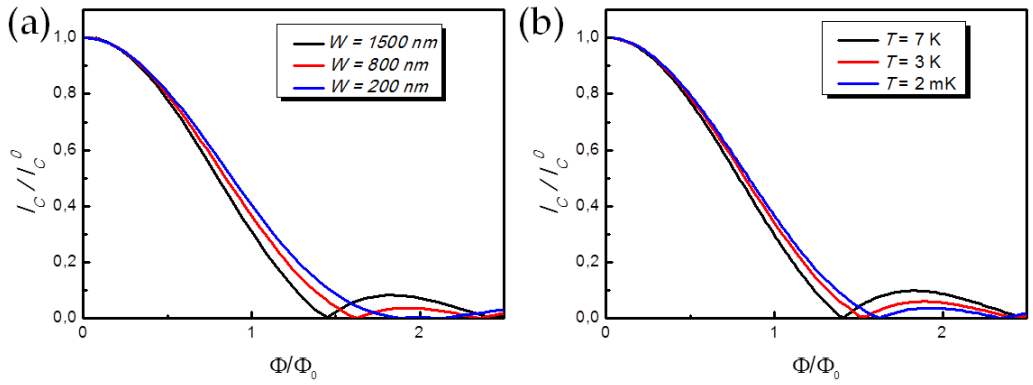

Figure 2.9: Plot of the normalized critical current I_C as a function of the magnetic flux in a 1-µm-long S-QPC-S junction. The curves are calculated for different values of the junction width W (a) and temperature T (b). In (a) T is equal to 10 mK, while in (b) W is assumed to be 0.8 µm. $\Phi_0 = h/2e$ is the magnetic flux quantum. I_C^0 is the critical current at zero magnetic field.

2.4 S-QR-S junctions

Similarly to the case of the QPC, very interesting effects are obtained if a normal QR is coupled to two superconducting electrodes, thereby creating a ballistic S-QR-S junction. This device differs from the direct-current superconducting quantum interference device (DC SQUID) [2], where two Josephson weak-links are present, since a single weak-link with two distinct arms connects the same N/S interfaces [see Fig. 2.10(a)]. In the following lines, we will discuss how this feature determines the properties of the QR interferometer.

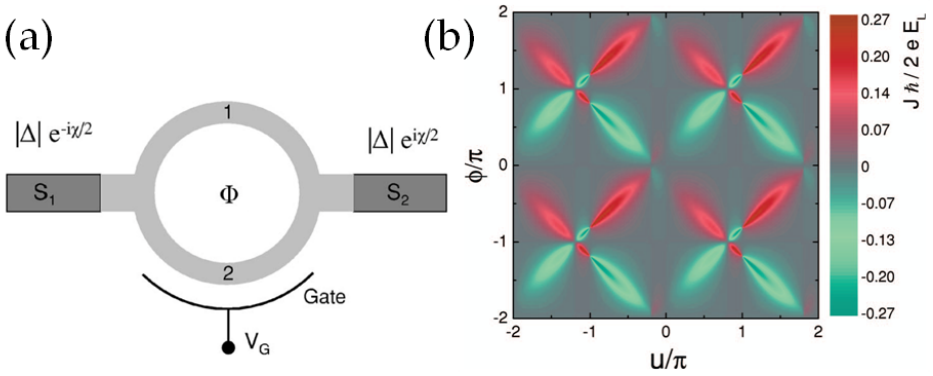

Figure 2.10: (a) Schematic drawing of an S-QR-S junction. A magnetic flux Φ and a gate voltage V_G can be applied. (b) Colour plot of the Josephson current J as a function of the magnetic and electrostatic phase shifts: $\phi = 2\pi\Phi/\Phi_{AB}$ and $u = eV_G/E_L$, respectively. The periodicity is the same of a normal Aharonov-Bohm interferometer. $E_L = \hbar v_F/L$ and $\Phi_{AB} = h/e$. Adapted from [14].

The S-QR-S configuration was first theoretically addressed by Dolcini and

Giazotto in 2007 [14]. Figure 2.10(a) presents the schematic drawing of the considered device. The superconducting pair potential is assumed to be $\Delta(x) = \Delta_0 e^{-i\chi/2}$ in the left lead, $\Delta(x) = \Delta_0 e^{i\chi/2}$ in the right lead and $\Delta(x) = 0$ in the normal region, where χ is the phase difference between the S electrodes. In the Dolcini-Giazotto model no Fermi velocity mismatch between the superconductors and the normal region is considered, while the quality of the interfaces is treated as a variable. By applying the scattering matrix method [59] (whose basic principles are discussed in section 1.4.2), it is possible to write the Josephson current flowing through the junction as a sum of two contributions $J_d(\chi)$ and $J_c(\chi)$, arising from the discrete Andreev levels and the continuous spectrum, respectively. It turns out that both these contributions depend only on the properties of the normal region scattering matrix [14]. In our case, the latter is composed by two Y-junction matrices (which also accounts for the transmission coefficients of the N/S interfaces) and by a propagation matrix which describes the phase shifts of electrons and holes in the normal ring arms. These phase shifts are due to the external magneto-electrostatic fields and lead to the AB interferometry effect: right movers, for instance, acquire a phase $\exp[i(kL - \phi/2]$ along arm 1 and $\exp[i(kL + u + \phi/2]$ along arm 2 [see Fig. 2.10(a)]. Here, $\phi = 2\pi\Phi/\Phi_{AB}$ and $u = eV_G/E_L$, where Φ is the magnetic flux in the QR, $\Phi_{AB} = h/e = 2\Phi_0$ is the Aharonov-Bohm magnetic flux quantum and V_G is the voltage applied to the side gate.

Because of these interference effects, the S-QR-S junction can work as a π-junction. The latter is a system where the sign of the Josephson current can be externally tuned, representing a fundamental building block for quantum computing. In Fig. 2.10(b) the Josephson current behaviour in the S-QR-S junction is shown. It is worth noting the oscillating behaviour of the supercurrent as a function of ϕ and u. In particular, the Josephson current dependence on the magnetic flux evolves with the AB period Φ_{AB}, in contrast to the standard Φ_0 periodicity of DC SQUID characteristics. This significant difference is due to the peculiar properties of ballistic S-N-S junctions. As it has been already proven in S-QPC-S systems, the Josephson current flowing through a ballistic S-N-S junction reflects the distinctive features of the normal region scattering matrix, such as the conductance quantization and the AB interference period.

The last statement does not apply to diffusive junctions, where the strong impurity scattering randomizes the momentum of the quasi-particles [54]. As a matter of fact, in 2011 Wei *et al.* [13] fabricated metallic S-QR-S junctions in the diffusive regime and observed a $\Phi_0 = h/2e$ periodicity in the zero-bias resistance dependency on the external magnetic flux, as shown in Fig. 2.11.

In this thesis, we report the first realization of a ballistic S-QR-S interferome-

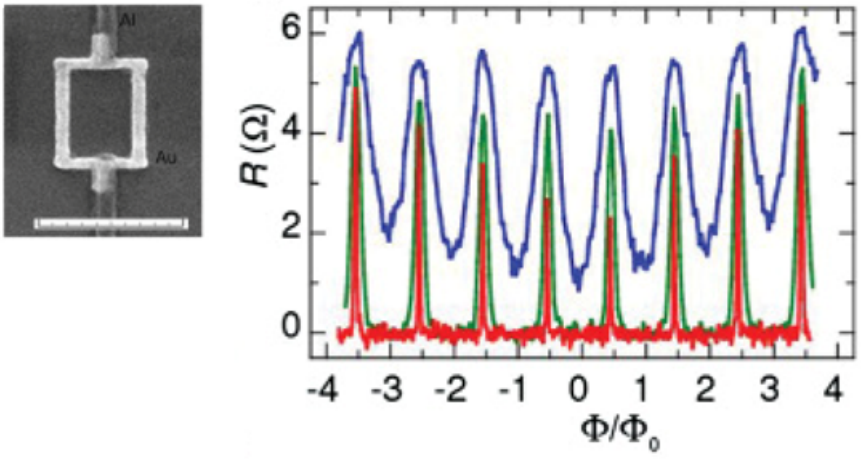

Figure 2.11: Plot of the zero-bias resistance of a diffusive S-QR-S junction as a function of the magnetic flux Φ, measured at three different temperatures: 0.6 K (blue curve), 0.4 K (green curve) and 0.03 K (red curve). $\Phi_0 = h/2e$ is the magnetic flux quantum. The inset shows a scanning electron micrograph of the metallic junction: the normal metal (Au) ring is shown in light grey, while the dark wires are the superconducting (Al) leads. The scale bar is 1 µm. Adapted from [13].

ter [12]. The fabrication process will be described in chapter 3, while chapter 5 will report the experimental critical current and resistance dependence on the magnetic flux with a theoretical discussion following the predictions by Dolcini and Giazotto [14].

Chapter 3

Device nanofabrication

3.1 Experimental realization of 2DEGs

Each device reported in this thesis is based on a 4-nm-thick InAs QW, inserted between two 5.5-nm-thick $In_{0.75}Ga_{0.25}As$ layers and $In_{0.75}Al_{0.25}As$ barriers. InAs has been found to be the ideal semiconductor to couple with superconductors, thanks to the lack of Schottky barrier at the interface with a metal, combined with the small effective mass of its electrons [39].
A schematic view of the heterostructures (named HM1544 and HM3090) employed to fabricate the devices investigated in this thesis is depicted in Figure 3.1. They were grown at CNR-IOM Laboratorio TASC in Trieste by means of Molecular Beam Epitaxy (MBE).
MBE is an Ultra-High-Vacuum (UHV) growth technique that can produce crystalline layers of extreme purity with monolayer precision, also allowing for dopant implantations during the process. Its basic principle is relatively sim-

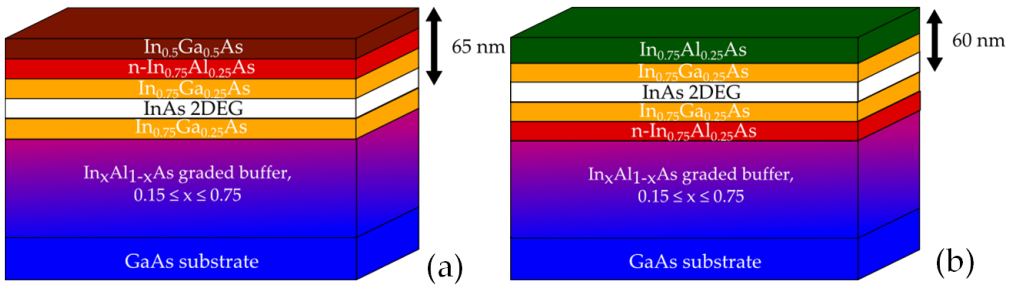

Figure 3.1: Schematic drawing of the two heterostructures [named HM1544 (a) and HM3090 (b)] used to fabricate the devices under investigation. In both structures a 2DEG (white) is created in the InAs 4-nm-thick quantum well. The main difference between the two heterostructures is the position of the n-doped layer (red): (a) in HM1544 the n-InAlAs layer is above the 2DEG, whereas (b) in HM3090 it is located below the 2DEG.

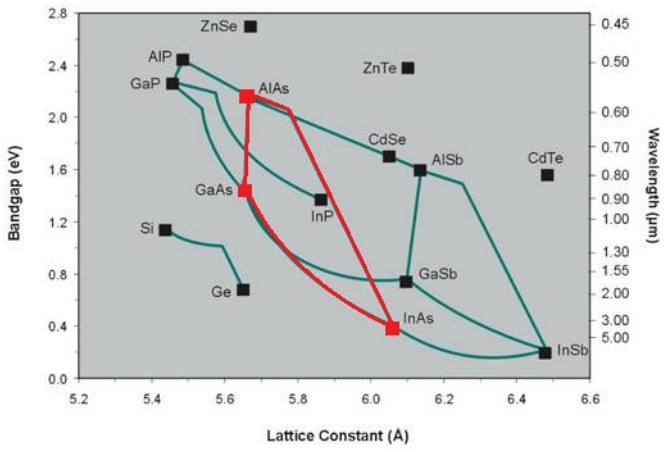

Figure 3.2: Band gaps and lattice parameters of most common semiconductors at 300 K. GaAs, AlAs, InAs and their ternary alloys are colored in red (adapted from [60]).

ple: atoms are produced by heating solid sources, placed inside several effusion cells. They then migrate in an UHV chamber through small orifices, under the form of highly collimated beam, whose flux rate can be controlled by shutters placed in front of each effusion cell. Various molecular beams containing Ga, As, In, Al and Si elements are aimed at a GaAs substrate, upon which atoms can diffuse and eventually are incorporated in the growing film. The sample holder is heated and constantly rotated, in order to obtain a uniform beam deposition on the substrate. Besides, with Reflected High Energy Electron Diffraction (RHEED) spectroscopy, it is possible to calibrate precisely the beam flux rates and to monitor the epitaxial growth monolayer by monolayer.

Apart from a few lucky exceptions, crystals of different semiconductors have different lattice parameters or even different crystal structures. This makes it very difficult to grow heterostructures without the formation of crystal defects. GaAs, AlAs and their alloys are the most important exception. In fact, they both have a zincblende structure and the difference between their lattice constant is so small (< 1%), that it is possible to grow an almost arbitrary thickness of these materials and their alloys without any strain between different layers.

As shown in Fig. 3.2, the situation is more difficult for InAs and its alloys: the lattice mismatch between InAs and the most common III-V commercial substrate, GaAs, is large (almost 7%), and with InP (other commercially available substrate) it is more than 3%. The latter substrate can not be used because Phosphorous is a contaminant for GaAs and AlGaAs.

As it can be seen in Fig. 3.1, a series of 50-nm-thick $In_xAl_{1-x}As$ layers are grown on top of a (001) GaAs substrate, with x ranging from 0.15 to 0.75. This step-graded buffer gradually relaxes the strain between the substrate and subsequent

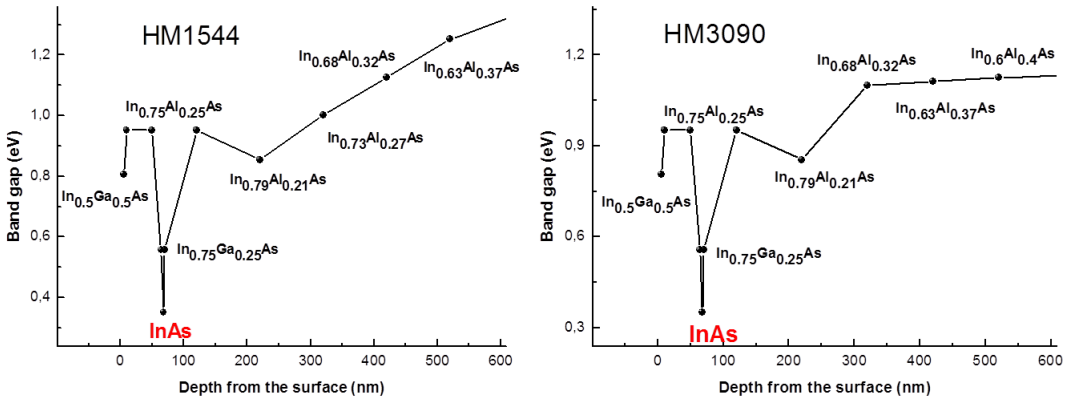

Figure 3.3: Band gap trend as a function of the depth from the surface for HM1544 and HM3090 heterostructures at room temperature. The InAs quantum well is highlighted in red.

layers, in order to grow the active region of the structure with a low defect density [61].

The growth of different layers modulates the band gap of the semiconductors along the z-axis (i.e., the axis parallel to growth direction). At 300 K the energy gap of InAs is equal to 0.35 eV and it can be increased by substituting a fraction of In atoms with Ga or Al atoms. In particular, $In_{0.75}Ga_{0.25}As$ has a band gap of 0.56 eV, whereas $In_{0.75}Al_{0.25}As$ band gap is 0.95 eV. These three materials create the QW in our heterostructures, whose band gap change along the growth direction is represented in Fig. 3.3. The n-doped region (colored in red in Fig. 3.1) is located in one of the $In_{0.75}Al_{0.25}As$ layers. In this particular configuration, scattering of the two-dimensional electrons from remote donor impurities is strongly reduced and extremely high mobilities can be achieved at low temperatures [62, 63]. On the contrary, the achievable charge density is relatively low if compared to metallic systems. This last property, combined with the high mobility and the small effective mass, results in a small Fermi energy ($\sim 65\ meV$) and a large mean free path, which enables us to realize completely *ballistic* nanodevices.

For HM1544 heterostructure, the sheet electron density was extracted from Shubnikov-de Haas oscillations [25] at 4.2 K without external illumination, and resulted to be $n \simeq 4.53 \cdot 10^{11}\ cm^{-2}$. Furthermore, the measured mobility $\mu \simeq 3 \cdot 10^5\ cm^2/Vs$ yields a large mean free path $l_e \simeq 3.33\ \mu m$.

For HM3090, the results are similar: $n \simeq 6.24 \cdot 10^{11}\ cm^{-2}$, $\mu \simeq 1.6 \cdot 10^5\ cm^2/Vs$ and $l_e \simeq 2.16\ \mu m$. All these values satisfy the clean limit condition (see Eq. 1.33).

As we will explain in the next sections, the 2DEG can be patterned in arbitrary shapes by means of Electron Beam Lithography (EBL) and Reactive Ion Etching (RIE) (see sections 3.2.2 and 3.2.4). By using these fabrication techniques

constrictions, rings and side gates can be produced, in order to create devices with a particular geometry and to obtain electron confinement in the plane of the 2DEG. Moreover, a Niobium (Nb) film can be deposited on the sample to create Superconductor-2DEG-Superconductor (S-2DEG-S) junctions.

3.2 Device fabrication

We fabricated and investigated two classes of devices: normal systems and hybrid superconductor-semiconductor systems. The former are preliminary devices obtained by tailoring the 2DEG in Quantum Point Contact (QPC) and Quantum Ring (QR) geometries, without superconducting structures; the latter are devices based on a S-2DEG-S junction, where the 2DEG mesa is contacted by two Nb leads and the Josephson effect can take place.
The HM1544 heterostructure was used for normal devices, while HM3090 was employed to fabricate the hybrid structures. In the case of normal devices, the fabrication process can be summarized as follows:

1. the heterostructure wafer is cleaved and its surface cleaned;
2. ohmic contacts are fabricated and annealed;
3. 2DEG mesa is designed by EBL and, after the deposition of a Titanium mask, etched;
4. Ti mask is removed and mesa is thermally cured.

For hybrid devices, two additional steps are performed after the previous four:

5. Nb leads are designed by EBL;
6. after HF:H_2O solution rinsing and low-energy Ar^+ cleaning, Nb is sputter deposited on the surface.

At the end of the process, the sample was mounted on a Dual-In-Line (DIL) sample-holder and wire bonded with Al wires.
All fabrication steps were performed in the clean room of NEST laboratory (class ISO7). In next subsections each step will be described in more details.

3.2.1 Sample preparation

A diamond scriber was used to cut typically 3 mm by 3 mm-sized pieces out of the heterostructure wafer. First, the edge of the surface was indented. Then, a light pressure was applied on the backside, so that the wafer split along the

chosen cleavage axis.
Each device had a size of approximately 0.5 mm by 0.5 mm, so that usually 20 devices could be fabricated on the same chip. Some extra space was left at the edges of the sample, not only for the ease of handling, but also in order to ensure a uniform PMMA (see next section) profile over the area of interest.
Throughout the fabrication process, the surface of the sample was kept as clean as possible.
Wafer cleaning was performed in a few steps:

1. dust and small wafer particles removal in an ultrasonic bath (optional);
2. rinsing in acetone (Ace);
3. rinsing in isopropanol (IPA);
4. drying with Nitrogen gas.

Water residues were eliminated by drying the sample on a hot plate at 180° C for 5 minutes. Other surface contaminants (especially organic contaminants) were removed using a Gambetti Colibri plasma system. The latter is a small vacuum chamber where low-energy Oxygen plasma can be created. Radio Frequency (RF) voltages are applied to ionize a low pressure gas (in our case 90% O_2 at 0.05 mbar, with a power of 40 W), which can break organic molecular bonds and react with organic contaminants to form H_2O, CO and CO_2. These products have relatively high vapour pressures and are evacuated from the chamber during processing. Thus, the resulting surface is perfectly cleaned.

3.2.2 Electron Beam Lithography (EBL)

EBL is a very flexible method to produce a nanostructured device on a substrate. The main steps of a typical EBL process are schematically represented in Fig. 3.4.

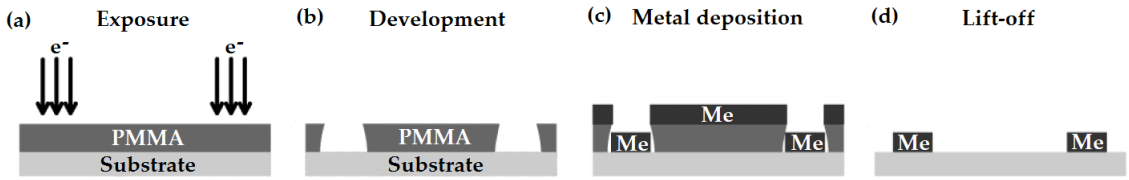

Figure 3.4: Example of an electron beam lithography process. a) A thin polymethylmethacrylate (PMMA) layer is exposed with highly energetic electrons (20-30 keV); b) development in a mixture of methylisobutylketone (MIBK) and isopropanol (IPA) results to a PMMA mask; c) the evaporated metal (Me) sticks on the substrate and on the PMMA; d) lift-off in hot acetone removes the PMMA mask and the metal covering it.

A polymer, polymethylmethacrylate (PMMA), diluted in a solvent, is spin coated on the substrate and baked on a hot plate. In this way, the solvent is removed and a homogeneous solid thin film of polymer remains on the substrate. When an area of PMMA is exposed to a dose of accelerated electrons (usually at an energy of 20-30 keV), the polymer fragments into very small parts. This exposed polymer can be removed using a mixture of methylisobutylketone (MIBK) and isopropanol (IPA) with a ratio of 1 to 3, in what is called the development step [see Fig. 3.4(b)]. During the development step, which usually takes a few minutes, the unexposed polymer is not affected and it is used as a mask. If a metal is evaporated, then it sticks on the substrate at the places where the developer removed the PMMA. The metal which sticks on the PMMA mask can be removed from the sample by dissolving the polymer in hot acetone: this is called the lift-off step. The result is a clean sample with metallic structures only at places where we exposed the PMMA with an electron beam.
All lithographies of this thesis work were performed using a Merlin Scanning Electron Microscope (SEM) by Zeiss Company, controlled by J. C. Nabity's Nanometer Pattern Generation System (NPGS) software. The design of the devices was realized with DesignCAD software.

3.2.3 Ohmic contacts

Ohmic contacts were shaped as 200 µm by 200 µm square pads by means of EBL. Together with the pads, we realized also 20 µm by 20 µm cross-shaped markers for following alignments. PMMA 950K (4% in ethyllactat-n-Butylacetat, AR-P 679.04 from ALL-RESIST GmbH) was spin coated on the sample surface at 6000 rpm for 1 minute and then baked for 15 minutes at 120° C on a hot plate. Thus, a 220-nm-thick film of solid PMMA was formed over the sample. It was exposed to a dose of 220 $\mu C/cm^2$ with 20 keV electrons, developed for 1 minute in AR 600-56 developer and rinsed in IPA for 30 seconds.
After that, we performed an O_2 plasma cleaning (20 W for 150 s) to remove possible last traces of PMMA in the developed regions. Afterwards, we used a Sistec thermal evaporator to deposit four layers of Nickel (Ni), Gold-Germanium (AuGe), Ni and Au on the surface of the sample. The best results were obtained with the following recipe: 10 nm Ni, 160 nm AuGe, 10 nm Ni and 60 nm Au. Evaporation rates were 1.5 Å/s for Ni, 5 Å/s for AuGe and 3 Å/s for Au.
Lift-off was made in 50° C acetone and the contacts were annealed by heating the sample up to a temperature of 400° C for 4 minutes.
During the annealing process, the electrodes diffuse deeply into the heterostructure wafer. The incorporation of Ge atoms is crucial at this point, since these

provide dopants in the InGaAs region near the metal interface, thereby increasing the conductivity of the layers between the contacts and the 2DEG.
The Ni layers shape into spikes that penetrate in the adjacent layers, improving the quality and the uniformity of the contacts. The final Au layer facilitates the wire bonding process. Typical annealed ohmic contacts are shown in Fig. 3.5 (a),(b). They were tested at 4.2 K: the average resistance resulted to be 50 Ω.

3.2.4 Reactive Ion Etching (RIE)

Reactive Ion Etching (RIE) is a dry etching technique that uses chemically reactive plasma to remove material deposited on wafers. The plasma is obtained by applying RF voltages to low-pressure gases, such as Argon (Ar), Sulfur Hexafluoride (SF_6), Methane (CH_4) or Hydrogen (H_2). The process is realized in a cylindrical vacuum chamber, with a wafer platter in its bottom portion. The wafer platter is electrically isolated from the rest of the chamber, which is usually grounded.
The plasma is initiated in the system by applying a strong RF electric field to the wafer platter. Electrons are stripped from the gas molecules and accelerated in the vertical direction (orthogonal to the wafer), whereas massive positive ions react more slowly to the applied field. In this way, electrons are absorbed by the wafer, polarising it negatively (the electrons which strike other parts of the chamber are transmitted to ground). At the same time, the loss of electrons in the plasma makes a global positive charge in the ion "cloud". Therefore ions are accelerated toward the wafer.
Thus, very anisotropic etching (along the vertical direction) can be achieved, in contrast to wet etching, which is typically isotropic. In this thesis work, we used the RIE technique to define the 2DEG structures, as it will be explained in the next section.

3.2.5 Mesa etching

The mesa is the conducting area of the heterostructure that remains unaffected by the fabrication process. It was designed (together with new 1-µm-sized markers) through a second step of aligned EBL. The alignment was performed using the markers produced during the ohmic contact fabrication process. PMMA AR-P 679.04 was spin coated on the sample with the same recipe as the one described in section 3.2.3. It was exposed to a variable dose (from 180 to 220 µC/cm^2, depending on the shape and the position of the exposed part) of 20 keV electrons, developed for 90 seconds in AR 600-56 and rinsed in IPA for 30

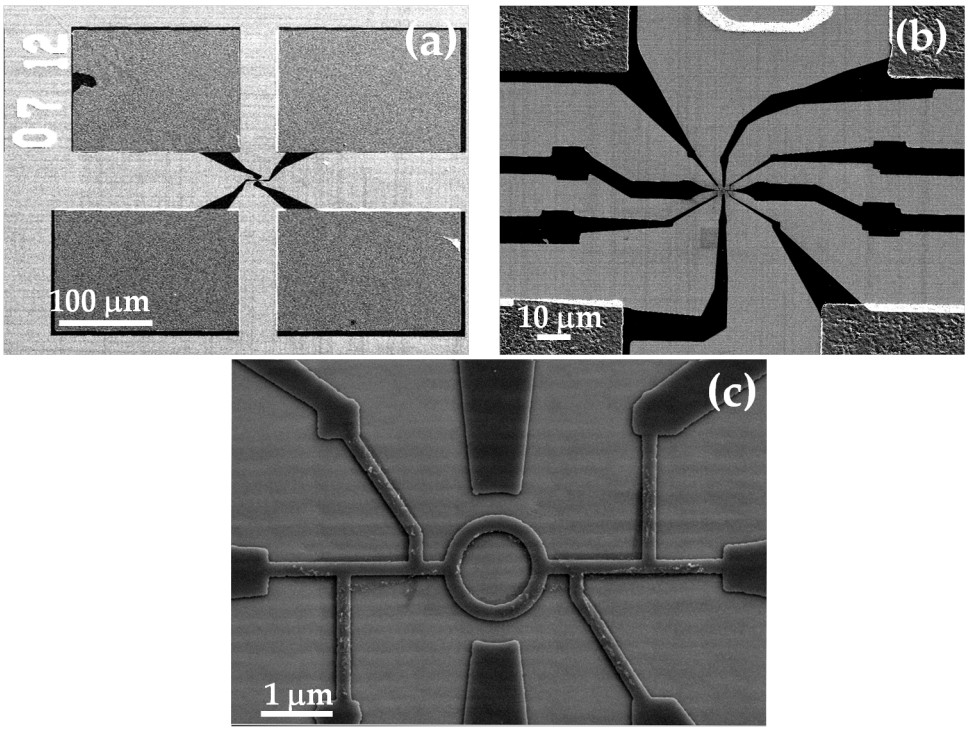

Figure 3.5: Examples of typical Ti masks. a) Low magnification SEM image of a Ti mask (dark region at the center of the image) for a normal QPC. The annealed ohmic contacts (grey square pads) are also covered by the mask. b), c) Higher magnification SEM images of a Ti mask for a normal QR.

seconds.

After an O_2 plasma cleaning, we thermally evaporated a 20-nm-thick Titanium (Ti) mask on the sample at a mean rate of 2 Å/s. It was designed to protect the ohmic contacts together with the mesa. Lift-off was made in hot acetone. Figure 3.5 shows some examples of Ti masks.

At this point, the sample was etched using a RIE system by Sistec. First, the vacuum chamber was cleaned for 30 minutes with 10 sccm of Ar and 30 sccm of O_2. Then, the sample was inserted in the chamber and etched for 10 minutes in $Ar/CH_4/H_2$ atmosphere (8 sccm of Ar, 5 sccm of CH_4 and 17 sccm of H_2). The pressure in the chamber was $\sim 6 \times 10^{-2}$ mbar and RF power was 150 W. Then, the surface was cleaned with an O_2 plasma etching for 7 minutes. The Ti mask was removed by a 1:20 HF:H_2O solution sample rinse.

This procedure resulted in an average 280-nm-etched mesa, which patterned the 2DEG in several devices with different geometries.

Eventually, the mesa was thermally cured at 300° C in order to reduce the defects created during the etching process. Examples of resulting devices are shown in section 3.3.

3.2.6 Niobium (Nb) sputter deposition

For hybrid devices, the last fabrication process is the deposition of superconducting leads in electrical contact to the 2DEG. This step is accomplished in a DC magnetron sputter deposition system.
The latter is a vacuum chamber where a solid target material is bombarded with ionized gas molecules in order to displace atoms from the target onto a substrate. The plasma is obtained by applying a strong DC voltage to a low pressure inert gas, such as Ar. The target holder constitutes the cathode, whereas the substrate holder is the anode. In our case, a magnetron, located below the target, creates also a static magnetic field, which traps the secondary electrons in a cylinder between the target and the substrate. These electrons are accelerated by the electromagnetic field and can ionize Ar atoms, thereby raising the ion density and improving the sputtering efficiency. Unlike thermal evaporation, which produces highly directional deposition, sputter deposition is almost isotropic. This is crucial for creating superconducting contacts to the etched mesa.

The superconducting leads were designed by a third step of aligned EBL. The alignment was performed using the markers produced in the previous EBL steps. PMMA bilayer was used to spin coat the sample: first, lower molecular weight AR-P 669.04 was spun at 6000 rpm for 1 minute and baked for 15 minutes at 180° C; then, higher molecular weight AR-P 679.02 was spun at 6000 rpm for 1 minute and baked for 10 minutes at 170° C. Using this recipe, a 240-nm-thick bilayer is obtained. It was exposed to a dose of 250 $\mu C/cm^2$ with 30 keV electrons, developed for 2 minutes in AR 600-56 and rinsed in IPA for 30 seconds.
High energy electrons penetrate and diffuse in the PMMA with a characteristic "pear" profile. The width of the "pear" increases as the PMMA molecular weight decreases. Thus, the section profile of the exposed PMMA can be modulated by using a bilayer, creating a larger "cavern" near the substrate. This technique facilitates the lift-off process, which otherwise can be extremely difficult for sputter deposited films.
After development, an O_2 plasma cleaning was made to remove last traces of PMMA from the exposed regions. Then, immediately before inserting the sample in the sputtering vacuum chamber, it was dipped in a 1:30 HF:H_2O solution for 90 seconds to remove oxides from the sample surface. These last two steps turned out to be essential for the quality of S-2DEG interfaces.
Previous to starting the sputter deposition, the sample was cleaned in the vac-

uum chamber with a low-energy Ar^+ sputtering for 1 minute: keeping the Nb target shutter closed, RF voltage was applied to create the plasma. The Ar pressure was 500 mTorr and the power was 25 W.
After that, Ar pressure was reduced to 40 mTorr, the target shutter was opened and the sputter deposition was started by applying a DC voltage of 230 V to the target holder (with a power of 250 W). The sample shutter was kept closed for 2 minutes in order to clean the target surface; then, Nb was deposited for 130 s, with a rate of ~ 15 Å/s. On the average, the produced films were 180 nm thick. Lift-off was made in hot acetone with mild sonication in ultrasonic bath. Examples of final devices are shown in Fig. 3.8 and Fig. 3.9.

3.3 Final devices

3.3.1 NQPC fabrication

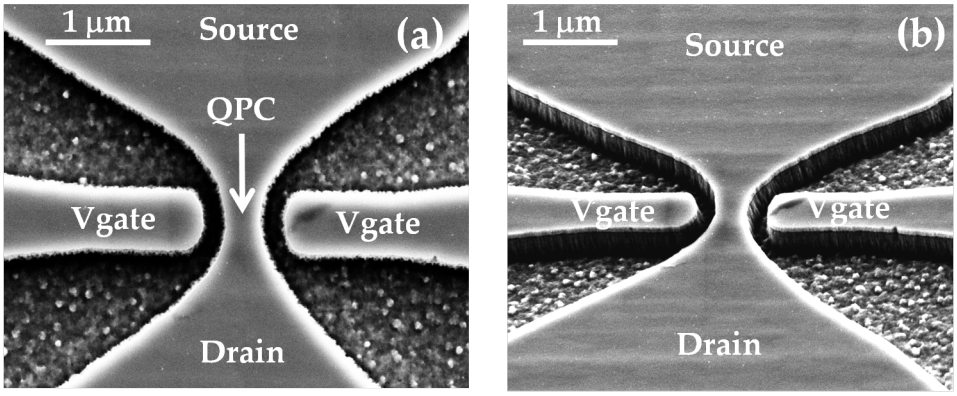

Figure 3.6: SEM images of a typical normal QPC. a) Vertical image of the QPC. The gates, the source and the drain are connected to four different ohmic contacts. b) Same device tilted at 45°: the etched mesa is clearly visible.

We fabricated Normal Quantum Point Contacts (NQPCs) by patterning a 450-nm-wide constriction of the 2DEG. Two side gates were etched at a distance of 150-200 nm from the QPC, with a diameter of 550 nm. When a negative voltage is applied to them, the electron density in the 2DEG is reduced and the number of available conduction channels decreases. The differential conductance of the QPC shows this phenomenon with $(2e^2/h)$-quantized plateaux. When the QPC is completely charge depleted, its conductance goes to zero and the so-called "pinch-off" is obtained. The experimental data for these devices will be shown in section 5.1.
A typical NQPC is represented in Fig. 3.6. The source, the drain and the gates are connected to four different ohmic contacts.

3.3.2 NQR fabrication

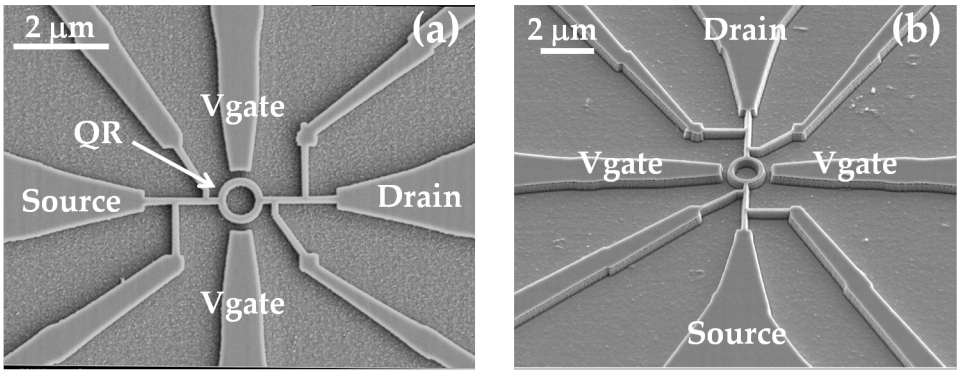

Figure 3.7: SEM images of a typical normal QR. a) Vertical image of the QR. The gates, the source, the drain and the other 4 arms are connected to eight different ohmic contacts. b) Same device tilted at 45° to highlight the mesa etching.

We etched the 2DEG in the shape of Quantum Rings (QRs) with outer/inner diameters of 1.4/1 μm to investigate the magneto-electrostatic Aharonov-Bohm (AB) effect. Two 500-nm-wide side gates were patterned at a distance of 200 nm from the nearest ring arm. Applying a gate voltage and an external magnetic field (orthogonal to the 2DEG plane), it is possible to induce AB interference effects on the QR conductance.
A typical device is represented in Fig 3.7. The additional 4 arms connected to source and drain can be used to perform 4-probe measurements. The experimental results will be presented in section 5.2.

3.3.3 S-QPC-S junction fabrication

We produced QPCs with superconducting leads (S-QPC-S) by etching a rectangular mesa island at a distance of 200 nm from two side gates and by sputter depositing the Nb contacts on the etched surface. The mesa islands are 1 μm long and 0.6 μm or 0.8 μm wide. The width of the gates is approximately 500 nm. Nb electrodes are connected to two Nb pads, which are wire bonded to the sample holder. On the contrary, the gates are connected to two ohmic contacts, as in the case of normal devices.
If the S-2DEG-S contacts are sufficiently clean, Andreev bound states originate in the 2DEG and a Josephson current can be detected. The latter can be modulated by applying a gate voltage and/or an external magnetic field (orthogonal to the 2DEG plane). The experimental results will be presented in section 5.3.
A pseudo-colour scanning electron micrograph of one of the 0.8-μm-wide junctions is shown in Fig. 3.8. Nb leads are coloured in blue, while the normal region

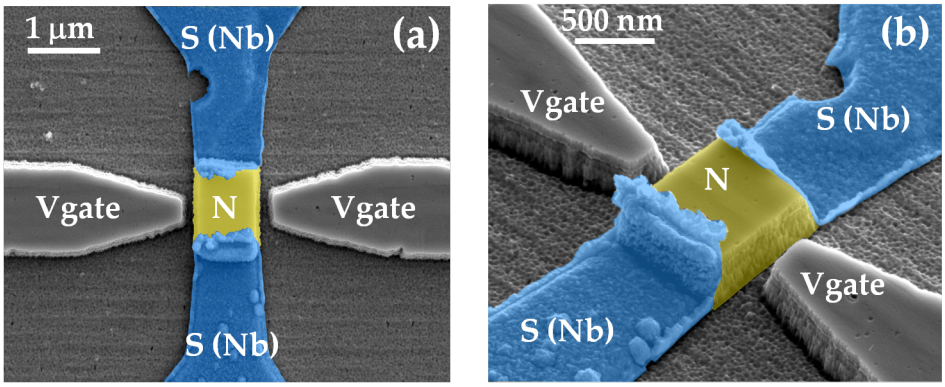

Figure 3.8: Pseudo-colour SEM images of a typical S-QPC-S junction. a) Vertical image of the device. Nb electrodes appears in blue whereas the normal region in yellow. The leads are connected to two different Nb pads and the gates to two ohmic contacts. b) Same device tilted at 45°: the sputter deposited Nb covers two walls of the etched mesa island, thus creating a S-2DEG-S junction.

is highlighted in yellow.

3.3.4 S-QR-S junction fabrication

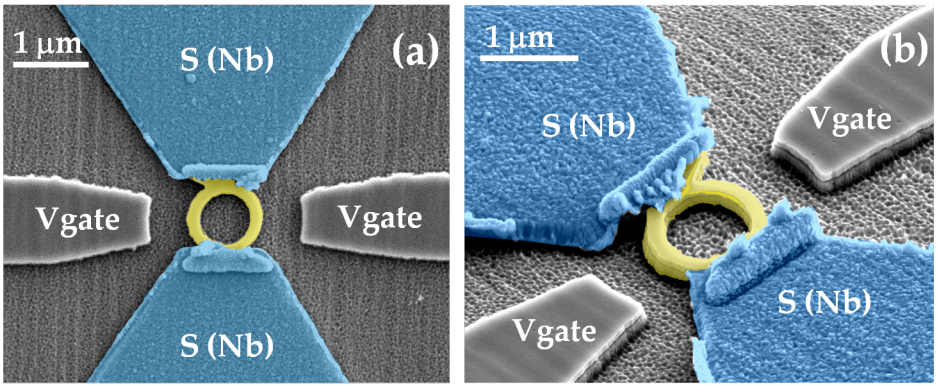

Figure 3.9: Pseudo-color SEM images of a typical S-QR-S junction. a) Vertical image of the device. Nb electrodes appears in blue whereas the normal region in yellow. The leads are connected to two different Nb pads and the gates to two ohmic contacts. b) Same device tilted at 45°: the lateral protrusions of the QR are visible. They were produced to maximize the S-2DEG contact region.

We fabricated Superconductor-Quantum Ring-Superconductor junctions (S-QR-S) by sputter depositing two Nb electrodes in contact with a previously etched QR mesa. The QR mean radius is $r \simeq 400$ nm and its arm width is ~ 180 nm. At the sides of the ring, two 1.1-µm-wide lateral protrusion were fabricated in order to maximize the contact surface between the superconductor and the 2DEG. If the S-2DEG interfaces are sufficiently clean, a supercurrent can flow through

the junction, as a manifestation of the Andreev bound states that originate in the 2DEG region.
Two side gates were etched at a distance of 250 nm from the nearest ring arm. Unfortunately they were not sufficiently etched (180 nm instead of the expected 280 nm) and did not work properly: in fact, low gate voltages produced no measurable effects on the transport properties of the junction, while applying more than 1.5 V (in absolute value) caused current leakages from the gates to the S-QR-S junction. Therefore, the Josephson current was manipulated only by means of an external magnetic field (orthogonal to the plane of the 2DEG).
A pseudo-colour SEM image of a typical device is shown in Fig. 3.9: the superconducting electrodes are coloured in blue, whereas the normal QR is represented in yellow. Experimental data for this device will be shown in section 5.4.

Chapter 4

Experimental setup

4.1 Cryogenics

We describe in this chapter the main cryogenic equipments used in our studies and briefly explain the setup used for the electrical measurements. All transport measurements were made at temperatures below 10 K. Two cryogenic systems were used to reach low temperatures: an Heliox VL and a Triton 200 by Oxford Instruments. The former can reach a base temperature of 230 mK, while the latter is able to cool the sample down to 10 mK.
Both systems are based on the unique properties of the stable isotopes of Helium (He), whose main thermodynamic features are resumed in the following section.

4.1.1 Properties of liquid Helium

Two stable isotopes of He exist in nature. The most common one is ^{4}He, consisting of two neutrons and two protons. The other one is ^{3}He, which is made of two protons and one neutron. ^{4}He is a boson and its boiling temperature is 4.22 K under atmospheric pressure. At 2.17 K it goes through the superfluid

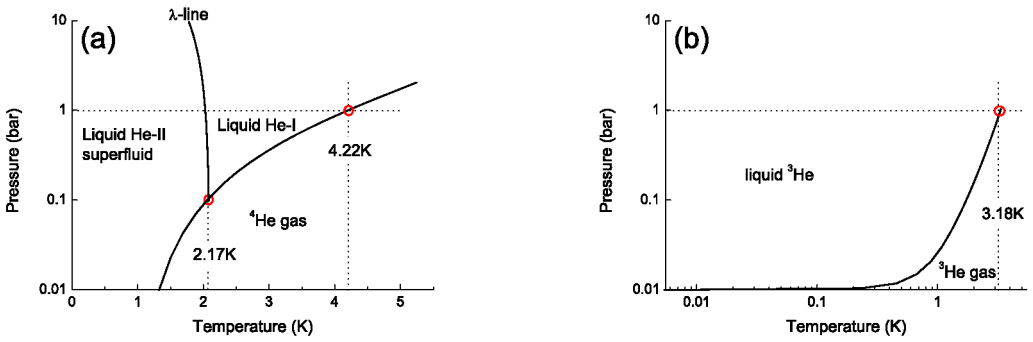

Figure 4.1: Pressure-temperature phase diagrams of ^{4}He (a) and ^{3}He (b), adapted from [64].

phase transition, marked by the λ-line in Fig. 4.1(a). ^{3}He is a fermion and its natural abundance on Earth is only 0.000137% [64]; it is commercially obtained as a byproduct of tritium manufacture in nuclear reactors. These facts make it extremely expensive (over 2500 \$/l [65]). ^{3}He boils at 3.19 K [see Fig. 4.1(b)] and becomes superfluid only at 2.5 mK because of its fermionic nature.
The main properties which make a liquid suitable for cryogenics are the latent heat of evaporation L and the vapour pressure P_{vap}. The latent heat of evaporation is the heat absorbed by the liquid during its evaporation, which occurs without a change in temperature. The vapour pressure is the pressure of vapour in thermodynamic equilibrium with the liquid. Liquid helium evaporates easily with any thermal excitation leading to a very small latent heat of evaporation and large vapour pressure. It can be demonstrated [64] that P_{vap} is given by

$$P_{vap} \propto e^{-\frac{L}{RT}}, \tag{4.1}$$

where R is the gas constant. Liquid helium can be cooled below its boiling point by pumping the "hot" gas which evaporates from it. If one pumps away atoms from the vapour phase, the most energetic atoms will leave the liquid to replenish the vapour. Therefore the mean energy of the liquid will decrease: it will cool. The cooling power of this method is given by

$$\dot{Q} = \dot{n}L \propto e^{-\frac{L}{RT}}L, \tag{4.2}$$

where $\dot{n}$ is the number of particles flowing through the liquid-vapour boundary. Assuming that the pumping speed is constant, $\dot{n}$ is proportional to the vapour pressure $P_{vap}(T)$ leading to an exponential dependence of $\dot{Q}$ on 1/T. In this way, the minimum temperature attainable with ^{4}He and ^{3}He refrigerators is limited to $T \simeq 1.2$ K and $T \simeq 230$ mK, respectively. At these temperatures the vapour pressure floating over the helium bath nearly disappears and the cooling power eventually becomes smaller than the external heat flowing to the bath. The higher limit for ^{4}He is due to several reasons: the most important one is that ^{3}He has a larger vapour pressure than ^{4}He at the same temperature, as it can be seen in Fig. 4.4(a). Besides, the specific heat of ^{3}He is larger and varies much less below 2 K. Finally, ^{4}He is superfluid below 2 K: a thin film of superfluid ^{4}He can creep up the pump line from a cold spot to a warm spot where it evaporates. Because of this, the pressure in the pump line is determined by this warmer place, preventing the liquid from cooling further.

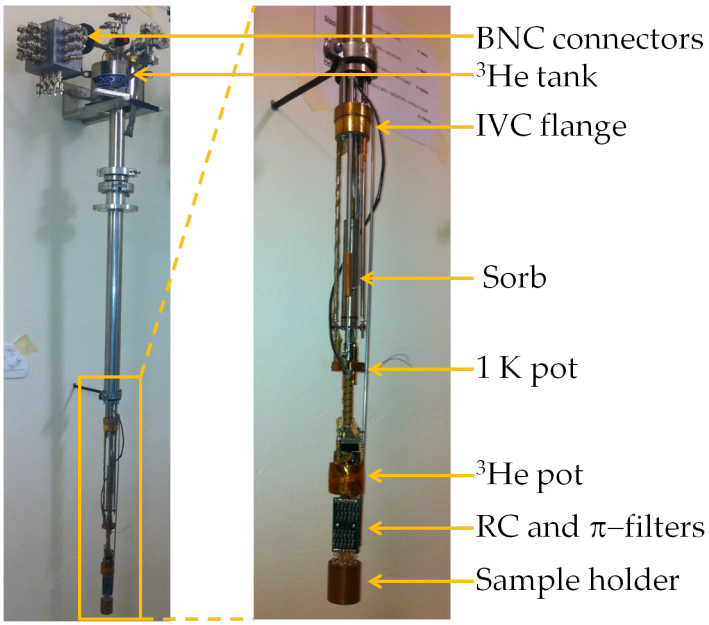

Figure 4.2: Picture of Heliox VL. The photo on the right shows the main components of the Inner Vacuum Chamber (IVC).

4.1.2 Heliox VL

The Heliox VL system is an ^{3}He refrigerator which is used in a liquid ^{4}He storage dewar (International Cryogenics). Its main components are shown in Fig. 4.2. The top of the cryostat always remains at room temperature. Its main elements are an ^{3}He tank (which contains 2.5 litres at 2 bar), together with three connectors for the temperature controller and for the measuring system. Also two vacuum valves are placed on top of the Heliox: one is for pumping ^{4}He from the dewar, the other is for evacuating the IVC to a rough vacuum before cooling the cryostat. A scroll pump (XDS5 by Edwards) is used to carry out these two processes.

The Inner Vacuum Chamber (IVC) is placed at the bottom of the Heliox. It is closed by a vacuum tube (not shown in Fig. 4.2) with a vacuum grease seal. The most important parts of the cryostat are placed inside the IVC: the Sorbtion pump (Sorb), the 1 K plate and the ^{3}He pot. The Sorb is a small vessel filled with several cm^3 of charcoal. Since gases adsorb at cold surfaces, the charcoal can work as an adsorption pump at low temperatures, thanks to its extremely large surface area. The 1 K plate is the ^{3}He condenser, which works at the temperatures of pumped ^{4}He. The ^{3}He pot is the container where liquid ^{3}He is collected. It is in thermal contact with the sample holder, which is placed below it.

In the following lines, the cool-down procedure is briefly described. After mounting the sample on the sample holder, the IVC is closed and pumped for about 30

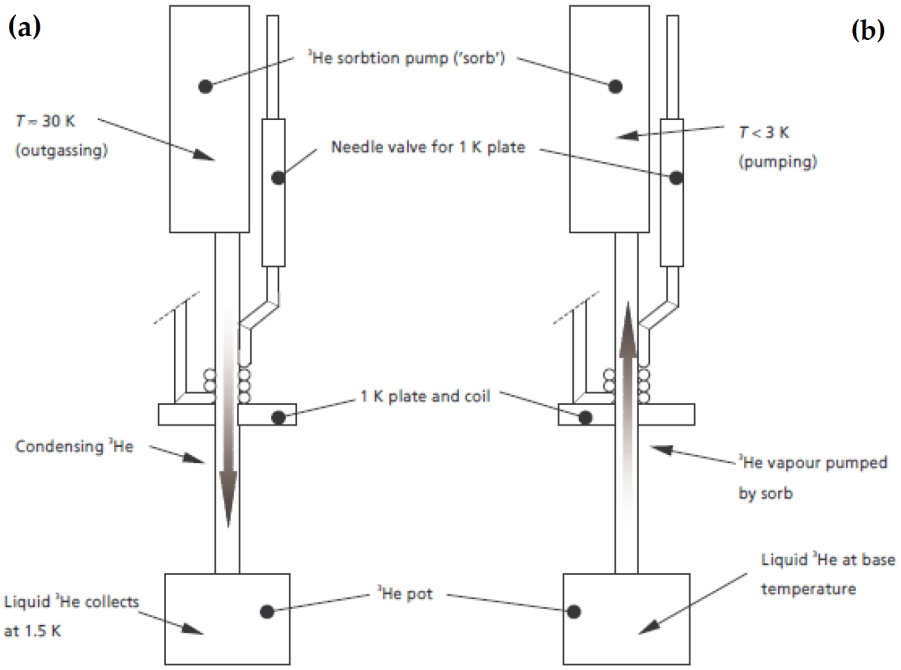

Figure 4.3: Schematic view of the Heliox cooling process. (a) ^{3}He condensing: the heated Sorb outgasses the ^{3}He, which is condensated by the 1 K plate and collected in the ^{3}He pot. (b) Final state: the ^{3}He pot is pumped by the cold Sorb and reaches the base temperature of 230 mK. Adapted from [66].

minutes. Then, a very small amount of exchange gas (He) is let inside the IVC in order to accelerate the cooling down of the inner parts. An exchange gas sorb is mounted on the 1 K plate; it pumps the exchange gas automatically during the cooling procedure. Then, the Heliox is pre-cooled in liquid Nitrogen, until the Sorb reaches a temperature of almost 77 K. Afterwards, the cryostat is transferred in the liquid ^{4}He dewar. When the system is at thermal equilibrium, the ^{4}He is pumped in order to cool the Sorb below 3 K. At this temperature it works as a pump which collects the ^{3}He from the tank placed at the top of the Heliox. After ten minutes, the Sorb is heated up to a temperature of about 40 K for 30-40 minutes. During this period, the Sorb outgasses the ^{3}He, which is condensed by the 1 K plate and collected in the ^{3}He pot [see Fig. 4.3(a)]. Then, the heater is turned off and the Sorb temperature falls down under 3 K, thereby starting to work as a pump again. In the final state, the sample is in thermal contact with a pumped ^{3}He bath [see Fig. 4.3(b)]. In this way, a base temperature of 230 mk can be obtained. The whole cool-down process takes 4-5 hours to complete. When all the ^{3}He is evaporated from the ^{3}He pot, the condensation process can be repeated.

The lines connected to the sample are filtered with two LC π-filter and two low-pass RC filters ($R = 1$ kΩ, C =47 nF). One π-filter is at room temperature, while the others are placed below the ^{3}He pot and work at low temperatures in order

to avoid Johnson noise. The combined cutoff frequency is 776 Hz. A superconducting magnet can be mounted at the bottom of the IVC: it produces magnetic fields orthogonal to the sample surface with a field/current ratio of about 200 Gauss/Ampere and with a maximum value of 600 Gauss.

4.1.3 ^{3}He-^{4}He dilution refrigerators

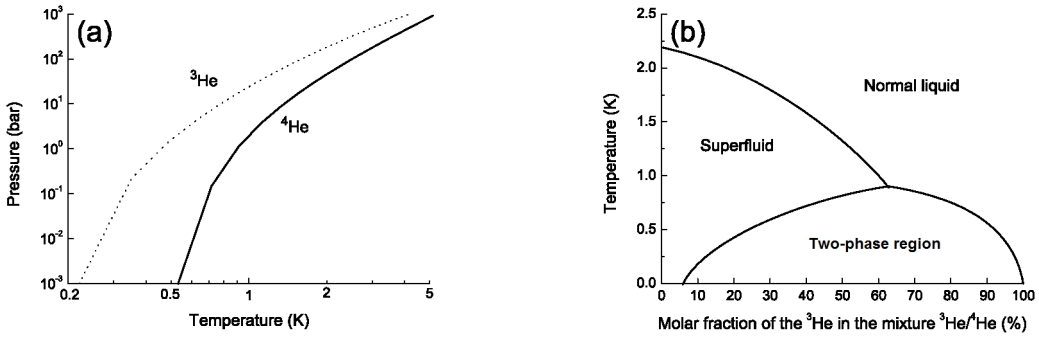

Figure 4.4: (a) Vapour pressure of liquid ^{4}He and liquid ^{3}He versus temperature. (b) Phase diagram of liquid ^{3}He-^{4}He mixture as a function of the ^{3}He concentration. In the two-phase region the mixture separates into a ^{4}He-rich and a ^{3}He-rich phase. Adapted from [64].

We now focus on another kind of cryostat whose working principles are the basis for Triton 200. The ^{3}He-^{4}He dilution refrigerator was first proposed by Heinz London in 1962 as a method to cool down below 300 mK, taking advantage of the special properties of the liquid ^{3}He-^{4}He solution.
The phase diagram of a ^{3}He-^{4}He mixture as a function of the ^{3}He concentration is shown in Fig. 4.4(b). If the ^{3}He concentration is more than 6.6%, two different phases appear below T = 0.87 K: one rich in ^{3}He, usually referred to as the concentrated phase, and the other one rich in ^{4}He, referred to as the diluted phase. The concentrated phase becomes nearly pure at sufficiently low temperatures, having $\sim$ 100% of ^{3}He atoms. In contrast, the diluted phase has a constant concentration of 6.6% ^{3}He down to the absolute zero.
The concentrated phase is less dense and floats over the diluted phase. The latter is superfluid and behaves as an "inert background" with negligible heat capacity. The ^{3}He atoms belonging to the diluted phase can be extracted or pumped, playing therefore the role of the "vapour pressure" in a conventional ^{4}He- or ^{3}He-refrigerator. By doing so, there will be a continuous flow of ^{3}He forced to go from the pure to the diluted phase in order to keep the 6.6% ^{3}He constant. The "vapour pressure" of a dilution refrigerator does not decrease with temperature, providing sufficient cooling power even at mK temperatures.

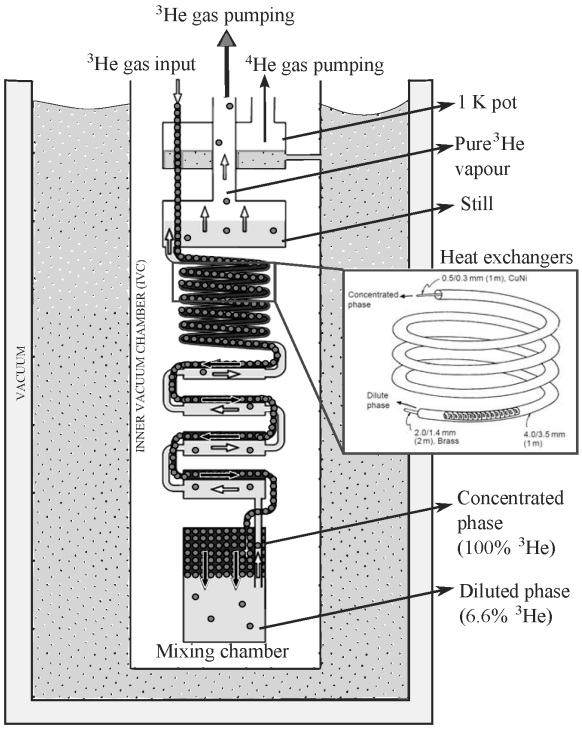

Figure 4.5: Schematic view of a ^{3}He-^{4}He dilution refrigerator. The inset shows an amplified view of the heat exchangers. Adapted from [64].

Figure 4.5 shows schematically how a dilution refrigerator works. It is introduced in a liquid ^{4}He bath and it is completely isolated from the environment by vacuum shields. The ^{3}He-^{4}He mixture is pre-cooled through thermal contact with the 1 K pot, i.e., a chamber that collects Helium from the ^{4}He bath that surrounds the IVC. As in Heliox, the 1 K pot reaches temperatures of about 1.3 K when the ^{4}He is pumped. Therefore it works as the ^{3}He-^{4}He mixture condenser. Then, the liquid mixture enters the mixing chamber, filling part of the still as well. Pumping the still forces ^{3}He atoms going from the concentrated to the diluted phases, thereby lowering the temperature. The pumped helium is then taken back to circulation in a closed circuit. At room temperature, ^{3}He gas is passed through liquid Nitrogen "traps". In these traps, impurities such as O_2, N_2 or H_2O are cryopumped so that they remain attached to the walls of the trap, while helium continues circulating.

The heat exchangers are one of the most critical parts of a dilution refrigerator determining the minimum temperature attainable. In the heat exchangers, the warm incoming ^{3}He is cooled down to mK temperatures by transferring heat to the cold outgoing helium. These are designed to maximize the contact area between the helium flow and the heat exchanger itself providing values as large as ~ 100 m^2. This can be achieved by using spiral coils as shown in Fig. 4.5. These tubes are additionally filled with sintered metal powder to increase the

contact surface area.
After the ^{3}He leaves the heat exchangers, it has eventually reached the temperature of the helium leaving the mixing chamber. It is then introduced again in the chamber through a capillary or impedance to make sure that it is liquid. The optimum working temperature at the still is about 0.7 K which can be controlled by a heater. At this temperature, almost all the vapour pressure is due to ^{3}He [see Fig. 4.4(a)].

4.1.4 Triton 200 dilution refrigerator

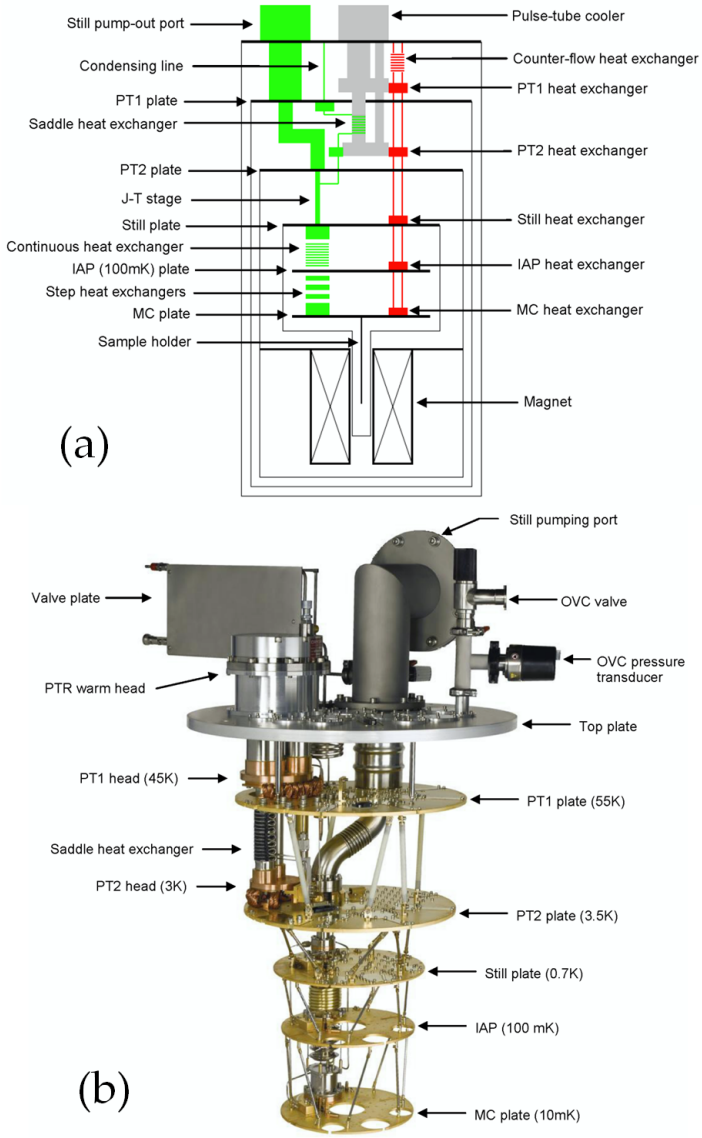

Figure 4.6: (a) Schematic view of Triton 200, showing the main components and heat exchangers inside the Vacuum Chamber (VC). The dilution circuit is shown in green and the pre-cool circuit in red. (b) More detailed view of the internal parts of the cryostat. Adapted from [67].

Triton 200 is a cryogen-free dilution refrigerator: instead of using a 1 K pot and a ^{4}He bath, the condensation of the ^{3}He-^{4}He mixture is achieved through a Pulse-Tube Cooler (PTC) and a Joule-Thompson (J-T) stage.

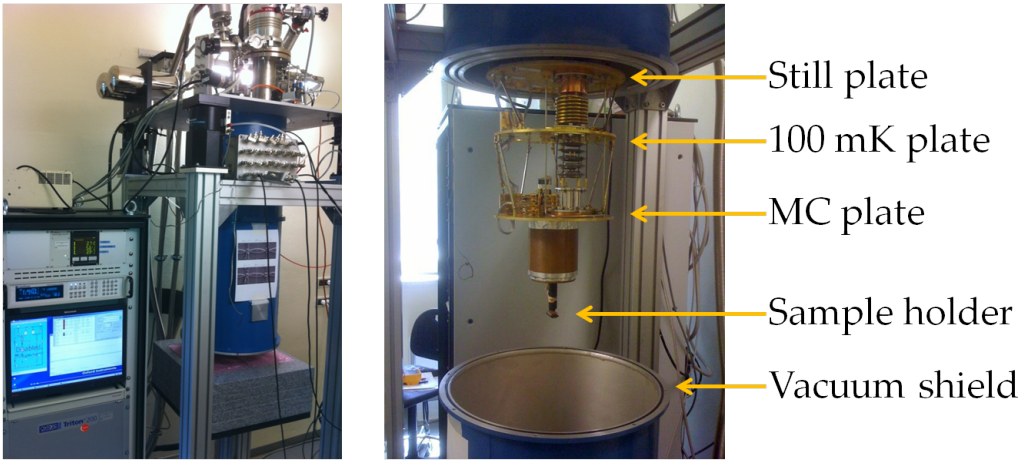

Figure 4.7: Pictures of Triton 200. On the left, the closed cryostat is shown together with the control computer. On the right, the main parts of the dilution unit are represented. The sample holder is also visible.

A Vacuum Chamber (VC) protects (thermally and mechanically) the cold parts of the cryostat. It does not contain an inner vacuum chamber, since the Triton does not need liquid ^{4}He to pre-cool the system. The top plate of the VC provides access at room temperature to all system services (thermometry, pumping lines, superconducting magnet), gas supply for the condensing circuit and pre-cool circuit, as well as the electric lines connected to the sample. An external tank at room temperature contains 75 litres of ^{3}He-^{4}He mixture (15 litres of ^{3}He and 60 litres of ^{4}He). The mixture is circulated through the pre-cool loop (red circuit in Fig. 4.6(a)) to assist the cooling of the components inside the VC with the the PTC. The PTC is composed by a compressor and a series of heat exchangers which are able to lower the temperature of the system down to 10 K in 12 hours. Afterwards, the pre-cool loop is evacuated using a turbo pump and the mixture is recollected in the tank. Then it is compressed and passed through the heat exchangers of the condensing line (see Fig. 4.6) in order to cool the gas to around 4 K. After that, the condensation is achieved using a J-T stage, consisting of a very efficient heat exchanger located inside the still pumping line and an impedance where the gas can undergo isenthalpic expansion. Then, the liquid mixture enters the Mixing Chamber (MC) and starts the dilution cycle which has been described in the previous section. In this way, a base temperature of 10 mK can be reached in almost 24 hours. The cool-down procedure is completely automatic and controlled by a computer, which monitors pressures and temper-

atures of different parts of the cryostat.
The lines connected to the sample for electrical measurements are filtered with two low-pass RC filters ($R = 1\ k\Omega$, $C = 47\ nF$), two LC π-filters and a coaxial low-pass filter (VLFX-80 by Mini-circuits with a cut-off frequency of 80 MHz). One of the π-filters is at room temperature, while all the other filters are placed below the MC plate and work at low temperatures. The total cut-off frequency is 765 Hz. A superconducting magnet is placed around the sample holder: it generates low magnetic fields orthogonal to the sample surface with a field/current ratio of 0.1663 Tesla/Ampere and a maximum field of 0.4 Tesla.

4.2 Electronics

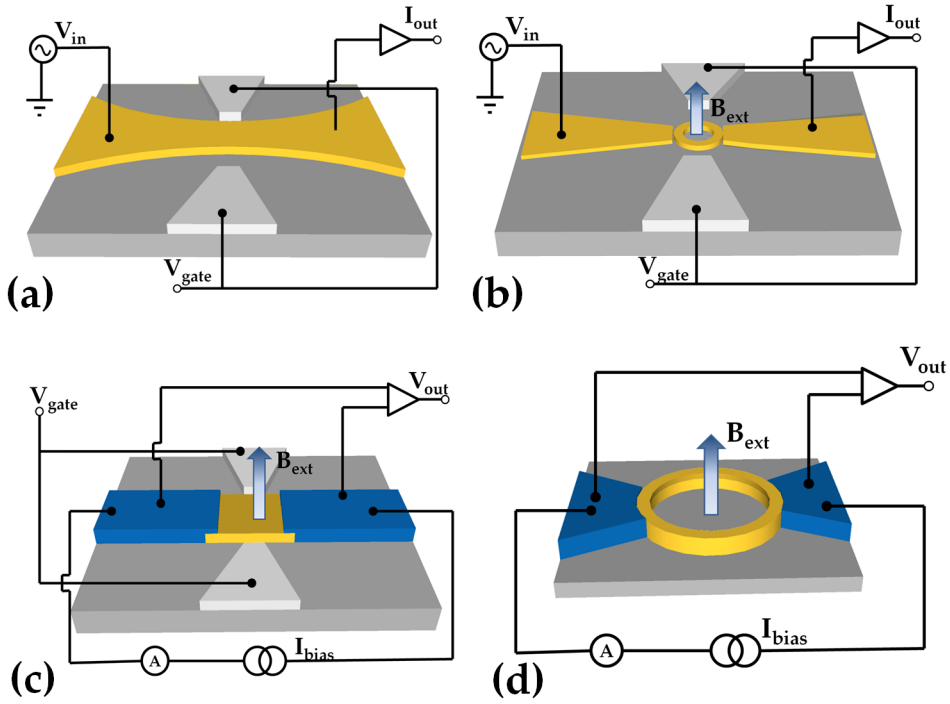

Figure 4.8: Schematic drawing of the measurement set-up used for different devices. The normal regions appear in yellow, the superconducting regions in blue and the gates in light grey. (a),(b) Two-probe measurements of the differential conductance are performed in the case of normal structures. V_{in} is the applied AC voltage, I_{out} is the measured current and V_{gate} is the voltage applied to the gates.(c),(d) Four-probe measurements of hybrid devices are shown. I_{bias} is the bias current, V_{out} is the voltage drop across the junction and B_{ext} is the external magnetic field applied orthogonal to the plane of the samples.

In this thesis work we performed both two-probe and four-probe transport measurements. The former method consists of applying a small AC voltage (V_{in}

must be $< K_B T/e$ to prevent electron heating) to the source electrode and measuring the resulting current from the drain with a phase-sensitive lock-in technique. The typical AC frequency used throughout the measurements was 17.3 Hz. In this way, the differential conductance of the device is obtained by dividing the resulting signal by the amplitude of the sinusoidal excitation. The main problem of this method is that the signal needs to be normalized by subtracting the in-series resistances of RC low-pass filters, ohmic contacts and mesa.
The second method consists of running a current through the device and measuring the voltage drop between source and drain. This is particularly easy to do in S-N-S junctions at low temperatures, since it is possible to connect two Al wires to the same superconducting pad with no need to worry about the voltage drop over the resistance of contacts and filters. In this way it is possible to obtain DC current-voltage characteristics or, alternatively, differential resistance curves by adding a small AC signal to a DC bias current.
The typical electrical configurations applied to the different devices are schematically depicted in Fig. 4.8.
In the case of normal devices, the AC signal was generated by a NF LI5640 lock-in amplifier and opportunely reduced by a voltage divider. The measured current was amplified by a DL Instruments 1211 pre-amplifier (the typical sensitivity was 10^7 V/A). The signal was extracted by the lock-in amplifier and then read by a multimeter (Agilent 34410).
For hybrid devices, the DC bias current was generated by a Digital-to-Analog Converter (DAC 488HR/4 by IOTECH). The voltage signal was amplified by a NF LI75A preamplifier (gain = 100) and read by a multimeter (Keithley 2700). A SRS SR830 lock-in amplifier was used for AC measurements.
In both cases, the gate voltage was provided by a HP 3245A function generator, while the magnets were driven by a Keithley 2602 power supply.

Chapter 5

Experimental results and discussion

In this chapter we shall present and discuss the experimental results obtained for the devices introduced in section 3.3.
First, we shall present the differential conductance of a Normal Quantum Point Contact (NQPC) as a function of the voltage applied to the side gates. We confirmed the conductance quantization described in section 2.1 and we observed its variation at different temperatures. Then, we shall discuss in section 5.2 the investigation of the Aharonov-Bohm (AB) effect in the Normal Quantum Rings (NQRs) introduced in section 2.2. The periodicity of the differential conductance dependence on the magnetic flux was analyzed and compared to the expected AB flux quantum. Afterwards, we observed the effects of the electrostatic AB effect by applying a voltage to the side gates.
In Secs. 5.3 and 5.4 we shall focus our attention on the superconducting hybrid junctions. After a preliminary characterization of the devices, external magneto-electrostatic fields were used to manipulate the Josephson current flowing through the S-2DEG-S junctions. In the case of S-QPC-S junctions, we were able to tailor the magnetic interference pattern of the critical current by applying a negative voltage to the side gates or by varying the temperature [10]. The results confirmed qualitatively the theoretical predictions made by Barzykin and Zagoskin [11] (see section 2.3). In addition, the critical current dependence on the gate voltage hinted at a quantized behaviour, even though not all the plateaus were clearly visible.
Finally, in the case of S-QR-S junctions, we observed an AB h/e periodicity of the Josephson current dependence on the magnetic flux [12], as predicted by Dolcini and Giazotto [14] (see section 2.4). This result demonstrates how the ballistic 2DEG region reflects its properties on the behaviour of the supercurrent which flows through the hybrid junction.

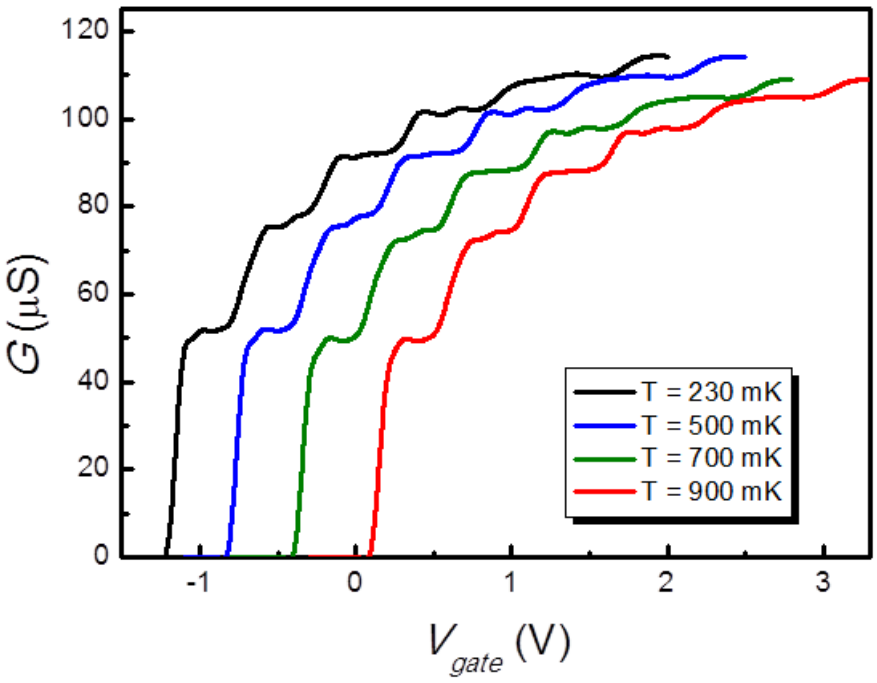

Figure 5.1: Plot of the QPC differential conductance as a function of the gate voltage at different temperatures. Five quantized steps of conductance are visible. The curves are horizontally shifted for clarity. It is possible to note how the quantization smoothens by increasing temperature.

5.1 NQPCs

The NQPCs under investigation (shown in Fig. 3.6) had a width $W \simeq 450$ nm. They were fabricated by patterning the heterostructure HM1544, introduced in section 3.1. At 4.2 K the expected Fermi wave vector of the electrons in the InAs 2DEG is $k_F = \sqrt{2\pi n_{2D}} = 1.69 \times 10^8$ m^{-1}, where $n_{2D} = 4.53 \times 10^{15}$ m^{-2} is the charge density in the 2DEG. Thus, the expected total number of conductance channels in the QPC is $N = k_F W/\pi \simeq 23$.

We measured the differential conductance of the devices by using the two-probe AC lock-in technique described in section 4.2. The frequency of the signal applied to the source of the QPC was 17.3 Hz, while the amplitude was V_{in} = 20 μV, which satisfies the condition $V_{in} < k_B T/e$ at 230 mK. The results obtained for one of the devices are shown in Fig. 5.1. By varying the gate voltage from 2 V to -1.2 V, the conductance decreases step-wise until the QPC pinches off at V_{gate} < -1.2 V. This voltage dependence does not vary with temperature, so it applies to all the horizontally shifted curves shown in Fig. 5.1. Five quantized steps are clearly visible. At zero gate voltage, the total resistance of the device (including the in-series resistance of cryostat low-pass filters, ohmic contacts and semiconductor mesa) ranges from 10.9 kΩ at 230 mK to ∼ 11.4 kΩ at 900 mK. The increasing resistance is caused by the reduced mobility of the electrons in

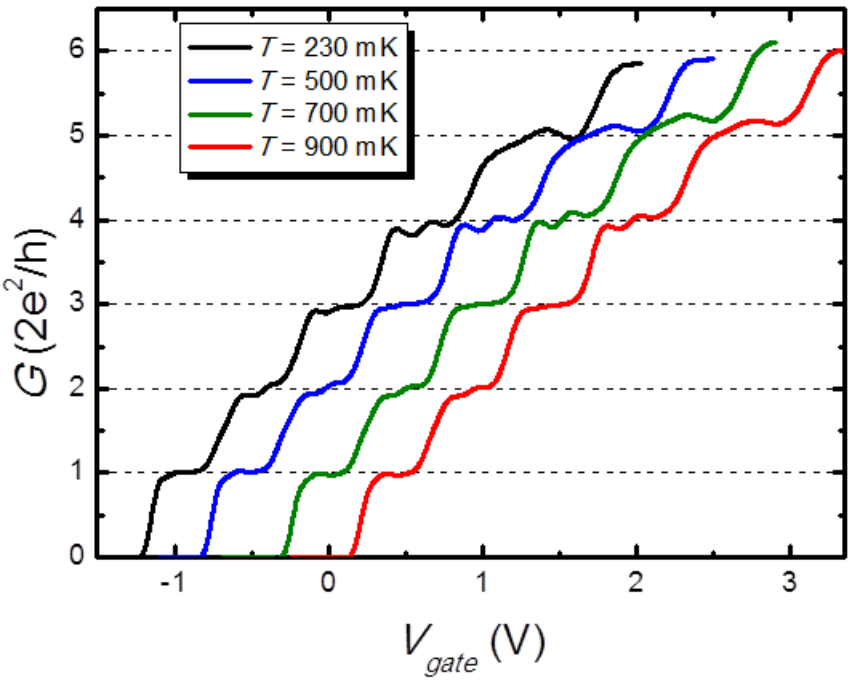

Figure 5.2: Normalized differential conductance versus the gate voltage at different temperatures. The step heights are consistent with the conductance quantum $G_0 = 2e^2/h$. The curves are horizontally shifted for clarity.

the 2DEG as the temperature is raised.

In order to compare the quantized step height to the conductance quantum $G_0 = 2e^2/h$, the curves represented in Fig. 5.1 must be normalized by subtracting the in-series resistances that are not due to the QPC. The value of the in-series resistance can be obtained by matching the resistance of the i-th plateau to R_0/i, where $R_0 = h/2e^2 \sim 12.9$ kΩ. In this way, we subtracted a resistance ranging from 6.6 kΩ at 230 mK to ~ 7 kΩ at 900 mK. The filters and the contacts contribute to these values with ~ 4.1 kΩ, so the mesa resistance varied from 2.5 kΩ to almost 3 kΩ. This high resistance value combined with the small number of measured conductance steps suggest that the charge density in the 2DEG is reduced after processing by about one order of magnitude with respect to the original value. This reduction could be due to the dry-etching fabrication process, which can produce charge depletion layers at the borders of the device [41]. However, as it can be seen in Fig. 5.2, the conductance plateau heights are all consistent with G_0. Some resonance features due to the boundary roughness are super-imposed on the step-like behaviour of the conductance. These features smoothen by increasing temperature, as well as the quantization effect turns out to be smeared.

Despite the reduced charge density in the QPCs, the fabrication process described in chapter 3 allowed us to produce ballistic devices that confirmed the

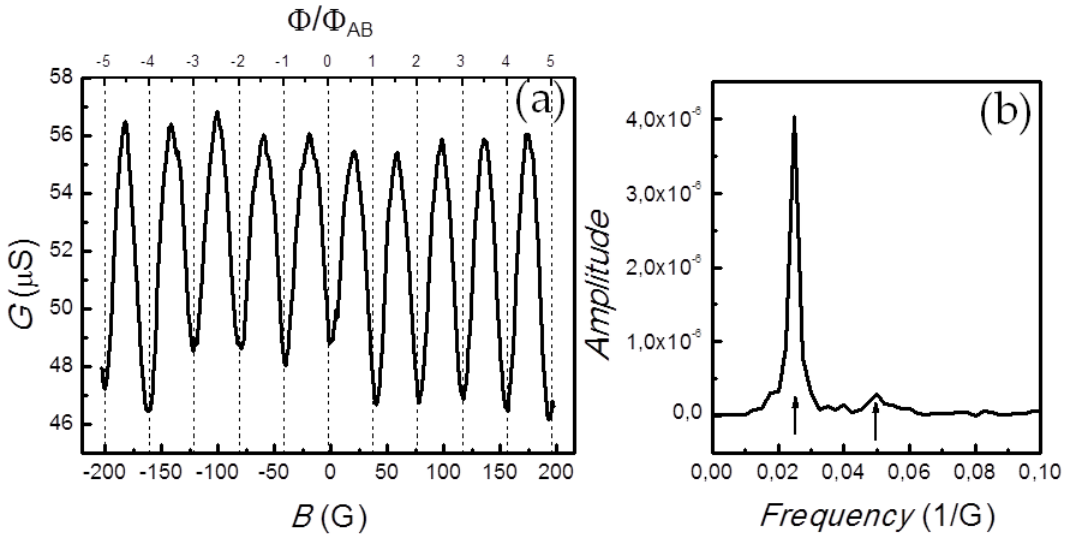

Figure 5.3: (a) Plot of the NQR differential conductance G versus the applied magnetic field B at T = 230 mK and zero gate voltage. The contrast $\Delta G/\langle G\rangle \simeq 19\%$. (b) The Fast Fourier Transform (FFT) of $G(B)$ shows that two harmonics contribute to the oscillations: one with period B_1 = (40 $\pm$ 4) G and one with period B_2 = (20 $\pm$ 2) G. The former value is consistent with $B_1^{th} = \Phi_{AB}/\pi r^2$, where r = 600 nm is the QR mean radius.

well-known conductance quantization effect.

5.2 NQRs

The fabricated QRs have a mean radius $r \simeq 600$ nm and 200-nm-wide arm rings, as shown in Fig. 3.7. They were measured with the same two-probe AC lock-in technique used to measure NQPCs. At 230 mK the bias amplitude was kept at 20 μV, while the frequency was set at 5.3 Hz. The typical average QR resistance was $\sim$ 20 kΩ, including the cryostat low-pass filters and the ohmic contacts.
Figure 5.3(a) shows the QR differential conductance G dependence on the external magnetic field B at 230 mK and zero gate voltage. The conductance G exhibits AB modulations with a contrast $\Delta G/\langle G\rangle \simeq 19\%$. The Fast Fourier Transform (FFT) of $G(B)$ shows that two harmonics contribute to the oscillations: one with period B_1 = (40 $\pm$ 4) G and one, presenting a lower amplitude, with period B_2 = (20 $\pm$ 2) G. The former is consistent with $B_1^{th} = \Phi_{AB}/\pi r^2$, while the latter, consistent with $B_2^{th} = \Phi_{AB}/2\pi r^2$, is due to multiple transport loops in the QR, as explained in section 2.2. These results indicate that the employed fabrication process has a small impact on the transport properties of the patterned nano-structures. Indeed, apart from the charge density reduction, the devices showed a good electric stability and gave us the possibility to prove coherent

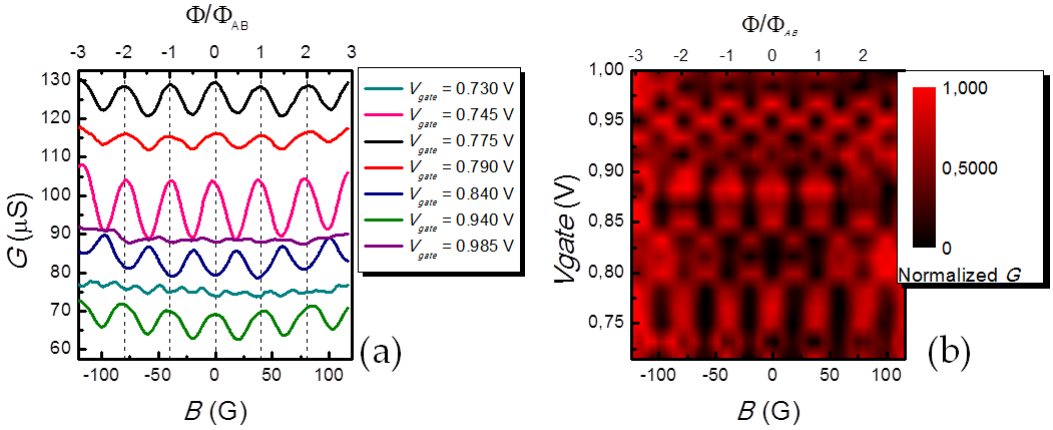

Figure 5.4: (a) Magnetic flux dependence of the QR differential conductance G for different values of the voltage applied to one of the gates. The other gate voltage was kept fixed at 0.5 V and the temperature was set at 230 mK. The electrostatic AB effect reduces the amplitude or invert the phase of the oscillations. (b) Colour plot of the QR normalized conductance as a function of the external magnetic field and of the voltage applied to one of the gates. The absolute value of the conductance is subtracted in order to highlight the periodicity change of the conductance for different values of the gate voltage.

electric transport through 200-nm-wide ring arms.

In order to investigate the electrostatic AB effect, we used the side gates etched at a distance of 250 nm from the ring arms. One of the gates was kept at a fixed voltage, while a bias sweep was applied to the other one. As already explained in section 2.2, this method allows us to vary the phase of the electrons in one of the ring arms, thereby changing the magnetic interference pattern obtained in Fig. 5.3. The results of these measurements are presented in Fig. 5.4(a). By varying the voltage applied to one of the side gates from 0.7 V to 1 V (whereas the other one was kept at 0.5 V), we could change the amplitude or invert the phase of the magnetic modulations. In particular, in Fig. 5.4(a), we can note that the magenta and the blue curve (measured at $V_{gate} = 0.745$ V and $V_{gate} = 0.84$ V, respectively) are clearly shifted by a phase π. The phase shift is highlighted also in the colour plot represented in Fig. 5.4(b). Each conductance characteristic obtained at a different gate voltage is normalized, so that the minima correspond to 0 and the maxima to 1. In this way, we lose information about the absolute value of the conductance (which is not monotonically increased with the gate voltage), but we are able to notice that the phase inversion occurs several times within the considered voltage range, following a relatively complex behaviour.

Given these promising results in all-normal devices, we extended the fabrication process in order to realize ballistic S-2DEG-S junctions.

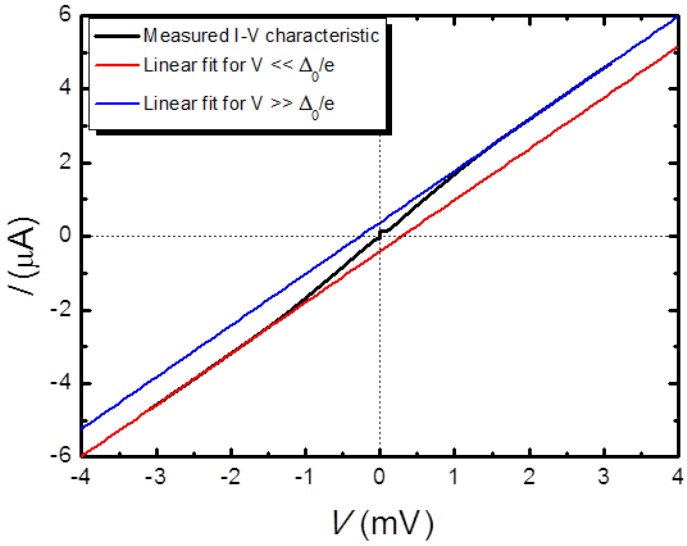

Figure 5.5: Experimental determination of the excess current I_{exc}. Two linear fits are used to approximate the normal-state I-V characteristic of the junctions, one for $V \gg \Delta_0/e$ and one for $V \ll \Delta_0/e$. I_{exc} is obtained from the mean value of the fit intercepts with the I-axis.

5.3 S-QPC-S junctions

As already mentioned in section 3.3, we fabricated S-QPC-S junctions by patterning a 1-μm-long mesa island on the HM3090 heterostructure and by sputter depositing Nb electrodes on the etched walls of the island. The hybrid junctions were measured with the four-probe technique described in section 4.2. In this Section, we report the results obtained for four different devices: two 800-nm-wide junctions (labelled A and B) and two 600-nm-wide junctions (labelled C and D).

The 180-nm-thick Nb films have a critical temperature $T_C \sim 8$ K, which corresponds to a BCS superconducting gap $\Delta_0 = 1.764 k_B T_C \simeq 1.2$ meV. Thus, the BCS coherence length is given by $\xi_0 = \hbar v_{FS}/\pi\Delta_0 \simeq 240$ nm, being the bulk Fermi velocity of the Nb $v_{FS} = 1.37 \times 10^6$ m/s [31]. The 2DEG mean free path is equal to $l_e \simeq 2.16$ μm. By comparing ξ_0 and l_e with the junction length $L = 1$ μm we conclude that the junctions operate in the intermediate-length ballistic regime, i. e., $\xi_0 < L < l_e$.

Following the method based on the OTBK model introduced in section 1.5, we can estimate the BTK Z parameter which describes the strength of the potential barriers at the N/S interfaces. As shown in Fig. 5.5, for each device we measured a current-voltage (I-V) characteristic and fitted the linear branches at $V \gg \Delta_0/e$ and $V \ll \Delta_0/e$. The slope of the fits give us the normal-state resistance R_N of

Device	Width	R_N	I_{exc}	Z	$\mathcal{T}$
	nm	Ω	nA		%
A	(800 ± 30)	(716 ± 2)	(391 ± 12)	(0.96 ± 0.01)	(52.0 ± 0.5)
B	(800 ± 30)	(763 ± 6)	(328 ± 2)	(0.98 ± 0.01)	(51.0 ± 0.5)
C	(600 ± 30)	(990 ± 10)	(320 ± 30)	(0.94 ± 0.01)	(53.0 ± 0.5)
D	(600 ± 30)	(1147 ± 2)	(227 ± 14)	(0.97 ± 0.01)	(51.5 ± 0.5)

Table 5.1: Physical parameters of the four measured S-QPC-S junctions. R_N is the normal-state resistance of the junctions, I_{exc} is the excess current, Z describes the strength of the barriers at the interfaces and $\mathcal{T}$ is the junction transmissivity in the normal state.

the junctions, while the excess current I_{exc} is obtained from the mean value of the intercepts with the I-axis. These results are used to estimate the Z value by using the graph represented in Fig. 1.14. Thus, it is possible to calculate the junction transmissivity in the normal state $\mathcal{T} = 1/(1 + Z^2)$. The results obtained for each device are presented in Table 5.1.

In Fig. 5.6(a), we present the temperature evolution of a few selected I-V characteristics for device A. The Josephson coupling survives up to $T \simeq 1$ K, whereas traces of superconductivity persist up to 2 K. At 30 mK a maximum critical current $I_C^0 = 105$ nA is observed, together with a marked hysteretic behaviour below 300 mK. This hysteresis stems from quasi-particle heating in the 2DEG-region once the junction switches into the dissipative regime [68]. Thus, it is possible to define two different critical currents for each I-V characteristic: the switching current I_{Cs}, at which the system switches to the dissipative state, and the retrapping current I_{Cr}, that determines the point where the junction returns to the Josephson state. The temperature evolution of the switching and retrapping currents are shown in Fig. 5.6(b). The purple dashed line displays the temperature dependence of I_{Cs} accordingly to the Chrestin, Matsuyama and Merkt (CMM) model [31] (see section 1.4.3) for the nominal values of the superconducting gap $\Delta_0 = 1.2$ meV, the 2DEG charge density $n = 6.24 \times 10^{15}$ m^{-2}, the junction width $W = 800$ nm and length $L = 1$ µm. The only fitting parameter is the value of Z, which results to be $Z = 1.02$, slightly higher than the value obtained with the OTBK method. At low temperature the CMM model recovers the experimental value of the maximum supercurrent while the thermal reduction predicted theoretically is much less pronounced than the one observed experimentally. This different behaviour might be due to two essential steps of

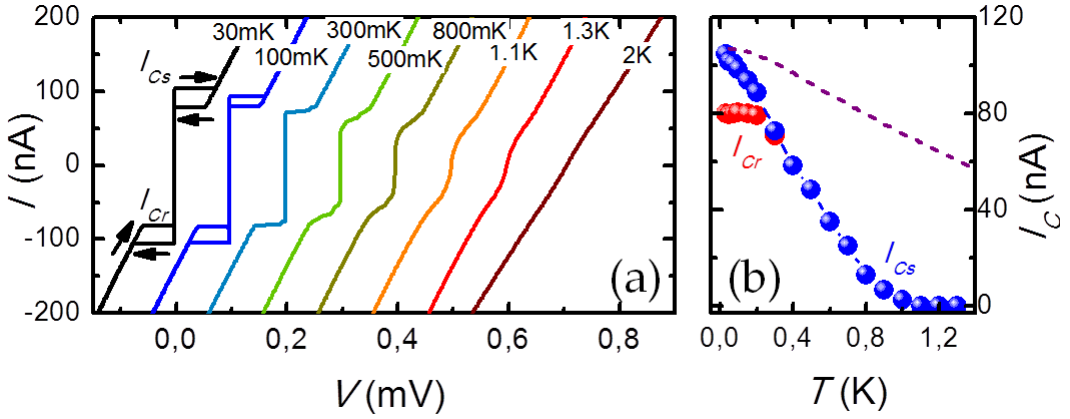

Figure 5.6: (a) Temperature evolution of a few selected I-V characteristics for device A. The curves have been horizontally shifted for clarity and the temperature spans from 30mK to 2 K. (b) Evolution of the switching (I_{Cs}) and retrapping (I_{Cr}) currents as a function of T. The device shows a clear hysteretical behaviour at temperatures below 300 mK. The Josephson coupling decays monotonically as a function of T surviving up to $T \sim 1$ K. The purple dashed line shows the calculated temperature dependence of the critical current accordingly to the CMM model with the fitting parameter Z = 1.02. The fitting curve shows a good agreement for the value of the low-temperature critical current.

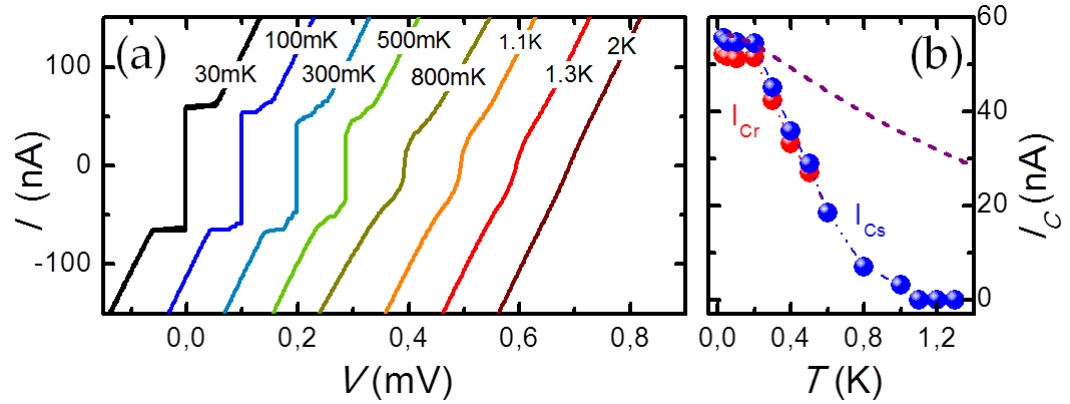

Figure 5.7: (a) Temperature evolution of a few selected current-voltage characteristics for device D. The curves have been horizontally shifted for clarity and the temperature spans from 30mK to 2 K. (b) Evolution of the switching (I_{Cs}) and retrapping (I_{Cr}) currents as a function of T. This device shows a limited hysteretical behaviour at temperatures below 300 mK. The purple dashed line shows the calculated temperature dependence of the critical current accordingly to the CMM model with the fitting parameter Z = 1.1.

the fabrication process: the Reactive Ion Etching (RIE) and the low-energy Ar sputtering, indeed, can damage the surfaces of the mesa island, thereby reducing the electron mean free path and the charge density in the regions exposed to the ion bombardment. Because of this, the experimental decay of the Josephson current results to be much faster than the theoretical one, since the imperfections near the interfaces can reduce the coherent transport between the Nb electrodes. Anyway, we stress that both the aforementioned fabrication steps are crucial for the realization of the hybrid junctions and for the achievement of fairly-transparent interfaces, as explained in section 3.

Figure 5.7 shows the temperature dependence of the Josephson current in a narrow junction, (device D). The main differences from device A are the value of the maximum critical current $I_C^0 = 60$ nA and the reduced hysteresis in the I-V characteristics. They are due to the smaller width of the junction. The CMM fit with $Z = 1.1$ is in good agreement with the observed value of I_C^0, but the theoretical I_C dependence on T decays much slower than the experimental one, as for device A.

After this preliminary characterization of the devices, we shall now focus our attention on the manipulation of the Josephson current by using magneto-electrostatic fields. In Fig. 5.8(a), the critical current dependence on the gate voltage V_{gate} for device A is shown. This measurement was made at $T = 10$ mK in the absence of external magnetic fields. The curve is obtained by averaging ten different I_C versus V_{gate} characteristics. The Josephson coupling decreases noticeably by shrinking the QPC. The junction reaches the dissipative regime for $V_{gate} \leq$ -1.2 V. The averaged conductance G versus V_{gate} in device A, which was extracted from 20 different conductance characteristics, is shown in the inset. G was measured in the regime of Josephson coupling suppression, at $B =$ 125 G with the two-probe AC lock-in technique (the amplitude of the excitation current was 15 nA and the frequency was 17 Hz). The conductance presents hints of a few quantized plateaus and reaches the pinch-off for $V_{gate} \leq$ -2.7 V. In Fig. 5.8(b), an expanded view of the I_C versus V_{gate} dependence is presented. The trend of the critical current suggests a possible quantization with $\Delta I_C =$ 8.6 nA, but the quantized steps are not all clearly visible. This might be due to the same reasons mentioned for the thermal reduction of the critical current. The dry etching and the Ar sputtering techniques can damage the 2DEG regions near the interfaces with the superconductors, thereby increasing the scattering between different transverse modes and reducing the visibility of the transport quantization. It is worth noting that for our devices the value of ΔI_C is not universal, but it depends on the 2DEG Fermi velocity, the junction length L and transmissivity $\mathcal{T}$, as explained in section 2.3. The supposed value of ΔI_C is of

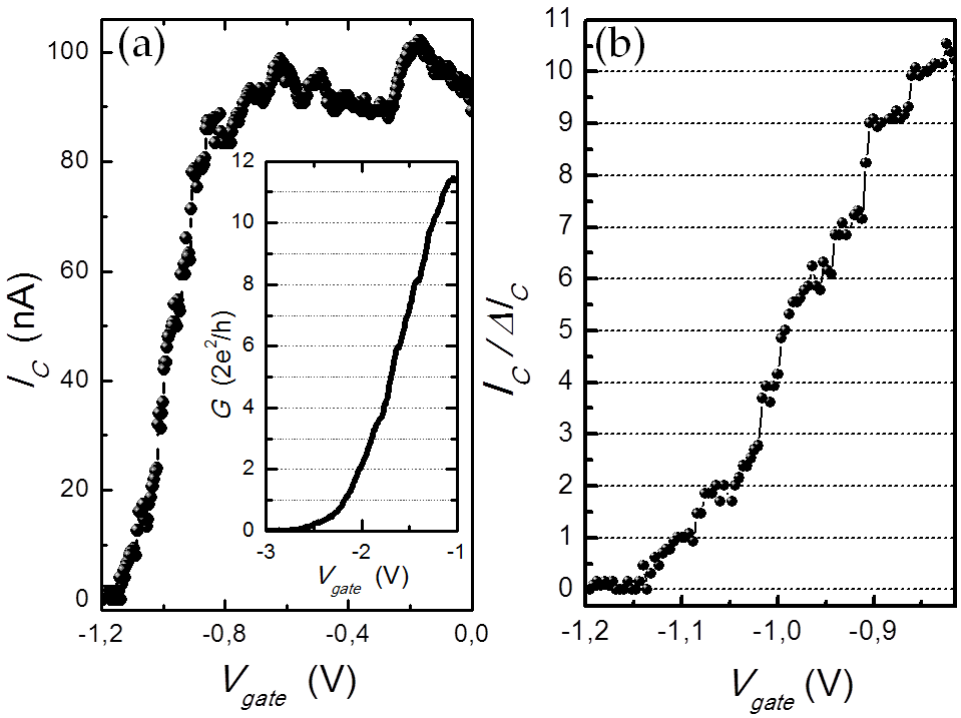

Figure 5.8: (a) Josephson critical current versus gate voltage with $B = 0$ for device A. The Josephson coupling decreases noticeably by shrinking the QPC reaching the dissipative regime for $V_{gate} \leq$ -1.2 V. The normalized conductance as a function of V_{gate} measured at $B = 125$ G for the same device is displayed in the inset. A few plateaus of conductance are visible. (b) Expanded view of the I_C dependence on V_{gate}. On the vertical axis the critical current is normalized in units of a quantization value $\Delta I_C = 8.6$ nA.

the same order of magnitude as the expected theoretical one, calculated from Eq. 2.14 for $L = 1$ µm and $\mathcal{T} = 52\%$.

More noticeable results were obtained by applying an external magnetic field B perpendicular to the plane of the junctions. In Fig. 5.9 we present the magnetic dependence of the critical current for all the investigated devices at 10 mK, with the gate voltage set at -0.5 V. The wide junctions exhibit a typical Fraunhofer-like pattern, while in narrow junctions I_C decays monotonically with B. In a previous work by Rohlfing *et al.* [56], both these behaviours were observed in junctions with different widths, as described in section 2.3. In this thesis work, we changed the effective width and length of each junction by applying a gate voltage or by varying the temperature. This approach allowed us to observe for the first time the continuous evolution of the magnetic interference pattern within the same junction.

Figure 5.10 shows the I_C versus B characteristics measured at 10 mK for a few selected values of V_{gate} in devices A (a) and C (b). By depleting the 2DEG-region with a negative gate voltage the Fraunhofer-like interference pattern observed

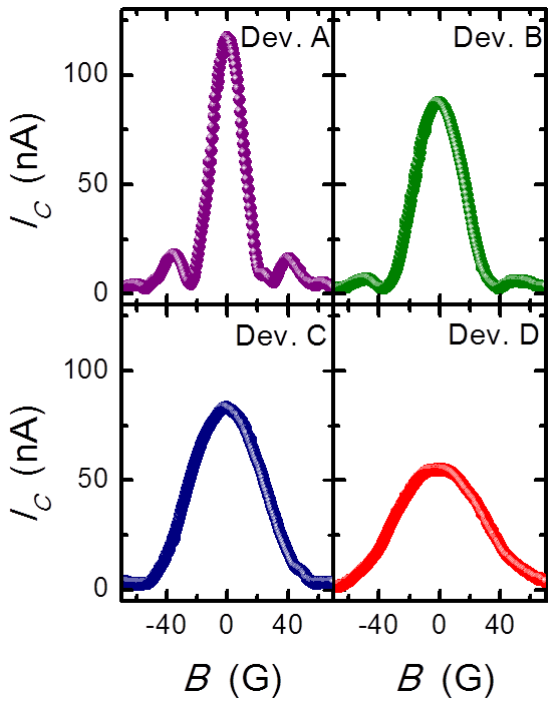

Figure 5.9: Magnetic dependence of the critical current I_C for all the investigated devices at 10 mK. The gate voltage was set to V_{gate} = -0.5 V. The wider junctions (devices A and B) present a Fraunhofer-like interference pattern, while the narrower junctions (C and D) exhibit a monotonic decay of I_C by increasing the magnetic field B.

in device A evolves to that typical of narrow junctions. Device C, instead, displays the Fraunhofer-like interference pattern for $V_{gate} \geq$ -0.5 V with the first-order maximum barely visible and dramatically switches to the narrow-junction one when shrinking the QPC. From the position of the first minimum in the wide junction interference pattern, we can estimate the area A of the 2DEG region by using the relation $LWB = \Phi_0$, where $\Phi_0 = h/2e$ is the superconducting flux quantum. At $V_{gate} = 0$, the first minimum is found at $B \simeq 26$ G, thus $A \simeq 0.79$ μm^2, that well matches the dimensions of devices A and B. By closing the QPC the position of the first minimum moves to higher values of B. At $V_{gate} =$ -1.45 V the minimum is observed at $B \simeq 34$ G yielding a value for $A = 0.61$ μm^2, which coincides with the area of the 2DEG-region in devices C and D. We remark that the obtained values agree with the geometrical junction areas without invoking the flux focusing correction introduced in section 2.3.

In Figure 5.11, we display a representative selection of the I_C magnetic interference patterns measured at different temperatures for devices A (a) and D (b) with V_{gate} = -0.75 V. In device A the first-order maxima of the Fraunhofer-like patter are visible up to $T = 300$ mK. When outrunning such temperature only the central peak remains visible up to 1 K. Device D shows a narrow-junction interference pattern in the whole range of temperatures.

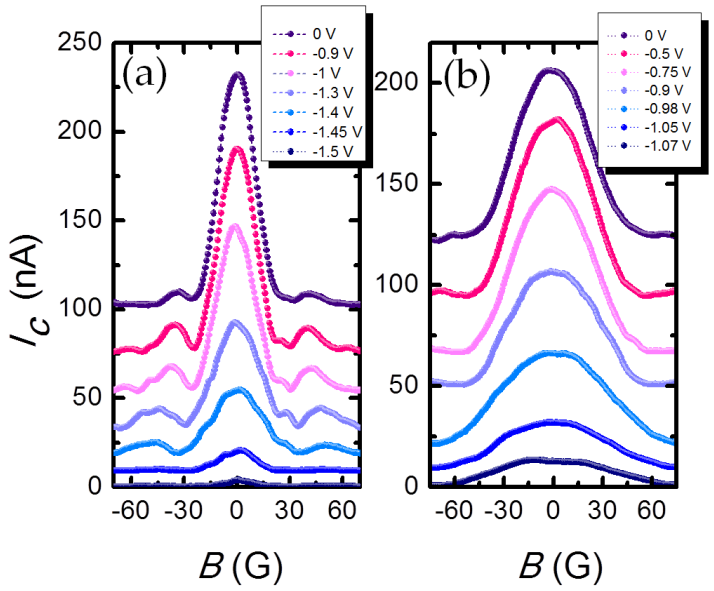

Figure 5.10: Magnetic interference pattern of the critical current I_C for different values of the gate voltage, measured in device A (a) and C (b). The curves are vertically shifted for clarity. Data were recorded at 10 mK. Device A shows a Fraunhofer-like interference pattern, which evolves to the narrow-junction-like one by shrinking the QPC. Device C shows the Fraunhofer-like interference pattern for $V_{gate} \geq$ -0.5 V with barely visible first-order maxima and switches to the monotonic decay, typical for the narrow junctions, when closing the QPC.

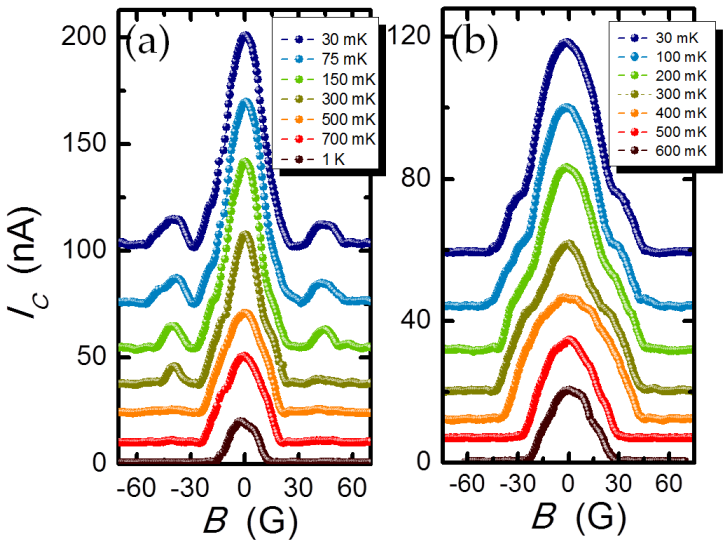

Figure 5.11: Magnetic interference pattern of the critical current I_C at different temperatures, measured in device A (a) and D (b). The curves are vertically shifted for clarity. Data were recorded at V_{gate} = -0.75 V. Device A shows a Fraunhofer-like interference pattern for $T \leq$ 300 mK. At higher temperatures first-order maxima disappear, with only the central peak surviving up to 1 K. Device D displays the narrow-junction interference pattern in the whole range of temperatures.

Now we can compare these results to the theoretical predictions made by Barzykin and Zagoskin [11] with the model introduced in section 2.3. From Eq. 2.18 we numerically calculated the magnetic interference patterns in a 1-µm-long S-2DEG-S junction for different values of W and T. The calculated curves are shown in Figs. 5.12(b) and 5.13(b), next to selected experimental characteristics measured at different V_{gate} [Fig. 5.12(a)] and T [Fig. 5.13(a)]. Grey dashed lines appear as a guide for the eye and show the evolution of the first interference pattern minimum. We note an overall good qualitative agreement between theory and experiment. The electrostatic shrinking of the QPC is equivalent to a physical reduction of the junction width W, while the raise of temperature corresponds to the decrease of the junction effective length $L_{eff} = \sqrt{L\xi_N}$, where $\xi_N = \hbar v_F / 2\pi k_B T$ is the 2DEG thermal coherence length. The theoretical model can not reproduce quantitatively the experimental data, since it considers ideal 2DEG/S interfaces and completely absorbing boundary conditions (see section 2.3). However, the obtained results demonstrate that the theoretical description made by Barzykin and Zagoskin captures the essential features of the junction physics when the L_{eff}/W ratio is changed by applying a gate voltage or by varying the temperature.

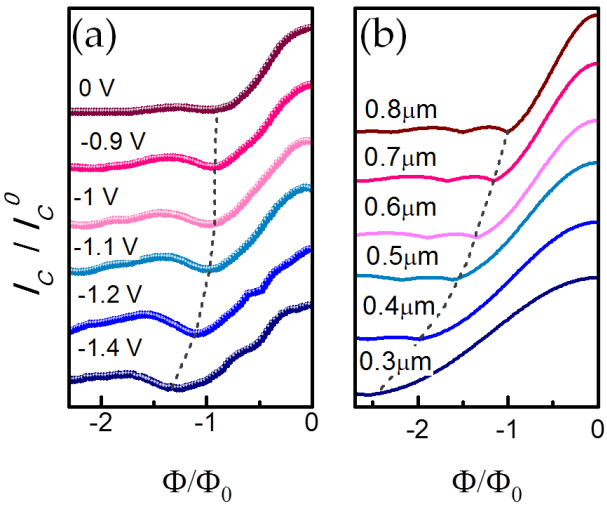

Figure 5.12: (a) Magnetic interference pattern of the critical current I_C for different values of V_{gate}, measured in device A. The curves are vertically shifted for clarity. Data were recorded at $T = 10$ mK. (b) Theoretical magnetic flux dependence of I_C for different value of W, according to the model by Barzykin and Zagoskin (see section 2.3). The curves were calculated from Eq. 2.18 for a 1-µm-long S-2DEG-S junction. Grey dashed lines appear as a guide for the eye and show the evolution of the first interference pattern minimum. In both graphs, the magnetic flux was calculated by considering the nominal geometrical area of the 2DEG region. We note a good qualitative agreement between theory and experiment.

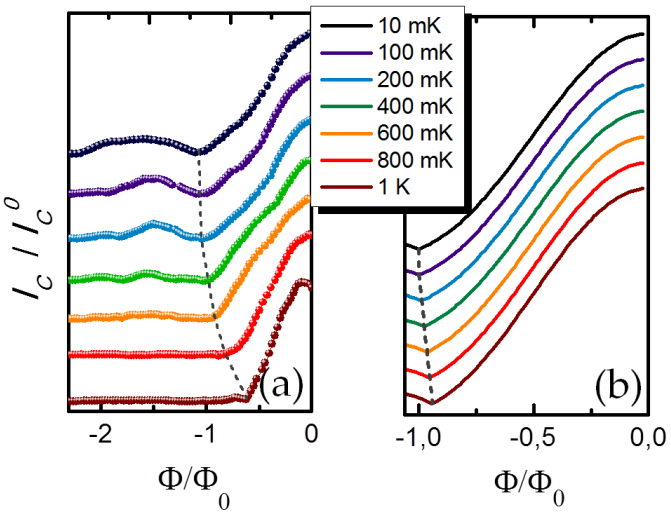

Figure 5.13: (a) Magnetic interference pattern of the critical current I_C at different temperatures T, measured in device A. The curves are vertically shifted for clarity. Data were recorded at V_{gate} = -0.75 V. (b) Theoretical magnetic flux dependence of I_C at different T, according to the model by Barzykin and Zagoskin (see section 2.3). The curves were calculated from Eq. 2.18 for a 1-µm-long S-2DEG-S junction. Grey dashed lines are guides for the eye and show the evolution of the first interference pattern minimum. In both graphs, the magnetic flux was calculated by considering the nominal geometrical area of the 2DEG region. We note a good qualitative agreement between theory and experiment.

5.4 S-QR-S junctions

As explained in section 3.3, we fabricated S-QR-S junctions by patterning a normal ring in the HM3090 heterostructure and by sputter depositing Nb contacts on the side of the etched walls. The structures were measured with the four-probe technique introduced in section 4.2. In the following we report the results obtained for one of the fabricated device.

The S-QR-S device is shown in Fig. 3.9. The total length of the junction is $L \simeq$ 1.2 µm. Comparing L with the superconducting coherence length $\xi_0 \simeq 240$ nm and the electron mean free path $l_e = 2.16$ µm, we can infer that the investigated device is in the intermediate-length junction ballistic regime. As in the case of S-QPC-S junctions, we estimated the value of the Z parameter by using the method based on the OTBK model presented in section 1.5. We obtained a normal-state resistance $R_N = 32\ \Omega$ and $Z \simeq 0.4$. The latter leads to an high transmissivity of the 2DEG/S interfaces, $T \simeq 85\%$.

Figure 5.14(a) displays the temperature evolution of a few selected S-QR-S current-voltage (I-V) characteristics at zero magnetic field. In particular, a well defined Josephson current with maximum amplitude of $I_C^0 = 52$ µA at 50 mK is

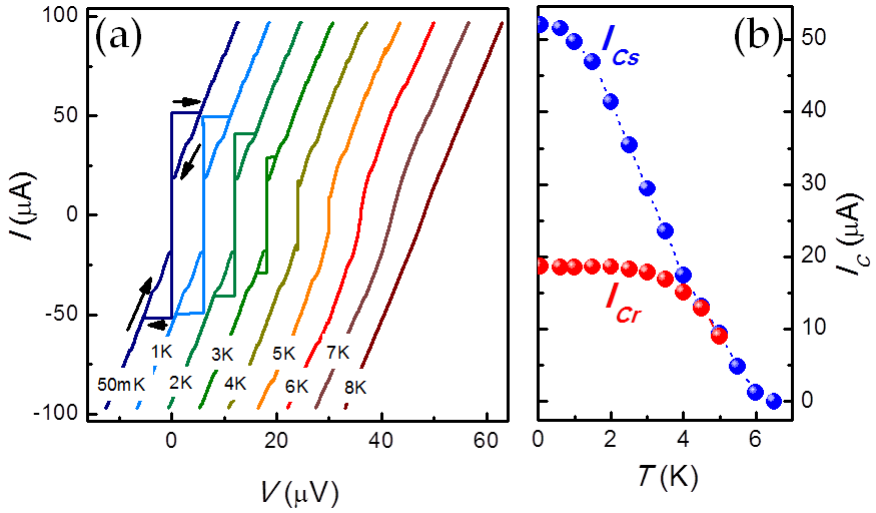

Figure 5.14: Evolution of the S-QR-S I-V characteristics as a function of temperature T at zero magnetic field. The curves have been horizontally shifted for clarity, and the temperature spans from 50 mK to 8 K. The Josephson current flowing through the junction survives up to $T \sim 6.5$ K, whereas traces of superconductivity in the Nb leads are visible up to $T \sim 8$ K. (b) Evolution of switching (I_{Cs}) and retrapping (I_{Cr}) critical currents as a function of T. Dotted lines are guides for the eye.

observed, and exhibits a marked hysteretic behaviour below 5 K. At higher temperatures, the hysteresis disappears, so that the switching (I_{Cs}) and retrapping (I_{Cr}) critical currents coincide. Traces of superconductivity are visible up to the critical temperature of the Nb electrodes ($T_C \simeq 8$ K, corresponding to a superconductor gap $\Delta_0 \simeq 1.2$ meV). The temperature dependence of I_{Cs} and I_{Cr} is shown in Fig. 5.14(b). Specifically, I_{Cs} saturates for $T \leq 1$ K whereas I_{Cr} remains constant for a wider range of temperatures (up to $T \sim 2.5$ K). The hysteresis, as already mentioned in the previous section, results from an increase of the 2DEG electron temperature once the junction switches to the resistive state [68]. Following the approach discussed in section 1.4, we know that one of the two contributions to the Josephson current in a S-2DEG-S junction is determined by the occupation of discrete Andreev levels. These levels carry a supercurrent in alternate directions. A thermal broadening of the electron distribution function leads to formerly unoccupied discrete states and thus, the maximum obtainable supercurrent is reduced from I_{Cs} to I_{Cr}. It is worth noting that the heating is relatively independent of the bath temperature, since I_{Cr} does not vary in a wide range of temperatures. The same argument applies also to the experimental data shown in Figs. 5.6 and 5.7.

As explained in section 1.5, MARs generate subharmonic gap structures in the differential resistance characteristics of hybrid junctions. Figure 5.15(a) shows a representative differential resistance (dV/dI) trace as a function of V at 50mK.The

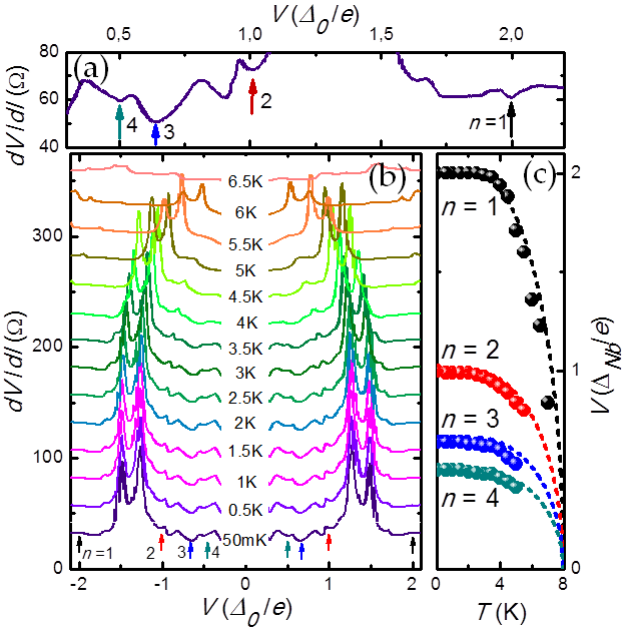

Figure 5.15: (a) Differential resistance (dV/dI) as a function of bias voltage measured at $T =$ 50 mK and zero magnetic field. Coloured arrows, placed at $V = 2\Delta_0/en$, match with the first four observable MAR dips. (b) Plot of dV/dI characteristics as a function of V , measured at different temperatures. The curves have been vertically shifted for clarity. (c) Temperature evolution of the position of the first four MAR dips in dV/dI characteristics. The BCS prediction for the superconducting energy gap are superimposed as dashed lines.

coloured arrows corresponding to voltages $V = 2\Delta_0/en$, where n is an integer, coincide with the position of the first four MAR dips. The curve was measured with a four-probe lock-in method, with an AC excitation amplitude of 100 nA and a frequency of 17.3 Hz. Figure 5.15(b) displays the full temperature evolution of dV/dI versus V. In Fig. 5.15(c) we show the temperature dependence of the position of the first four MAR dips and the comparison with the BCS prediction for the superconducting energy gap (dashed lines). We note a good agreement between the BCS prediction and the evolution of the dV/dI dips.

We now focus on the measurements that offer evidence that our device performs as a ballistic Josephson interferometer. We applied an external magnetic field B orthogonal to the plane of the junction and measured the evolution of the voltage drop V across the junction as a function of B at 50 mK for several DC-bias current values I_{bias}. In Fig. 5.16(a) we display a selection of the measured characteristics. By increasing I_{bias}, V shows an emergent series of peaks whose periodicity matches with the AB period, $\Phi_{AB} = h/e$, for a QR with $r = 306$ nm. This value for the radius is in good agreement with the inner one of our loop, ~ 310 nm. The h/e flux periodicity reveals the ballistic operation of our S-QR-S interferometer as theoretical predicted by Dolcini and Giazotto [14] (see sec-

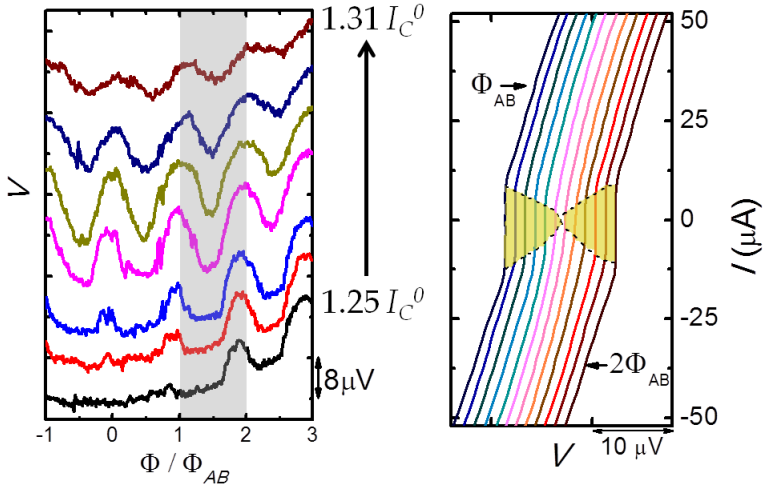

Figure 5.16: (a) Evolution of the voltage drop V developed across the junction versus magnetic flux measured at 50 mK for different DC-bias current spanning from $1.25I_C^0$ to $1.31I_C^0$ in steps of $0.01I_C^0$. V shows a modulation with an AB magnetic flux period $\Phi_{AB} = h/e$. The curves have been vertically shifted for clarity. (b) Evolution of the I-V characteristics comprised within the hatched grey region in (a). The magnetic flux ranges from $\Phi = \Phi_{AB}$ to $\Phi = 2\Phi_{AB}$ and increases in steps of $0.083\Phi_{AB}$. The yellow shadow region comprised within dashed lines highlights the magnetic flux-induced modulation of the Josephson critical current. The curves have been horizontally shifted for clarity and were measured at 5 K.

tion 2.4), and differs remarkably from the usual periodicity $\Phi_0 = h/2e$ observed in conventional SQUIDs. As already pointed out in section 2.4, this different behaviour arises from the topology and the ballistic nature of our S-QR-S junction. In DC SQUIDs the Φ_0 periodicity originates from the interference of *two* Josephson junction set in parallel. On the contrary, here a *single* ring-shaped weak-link connects the same 2DEG/S interfaces with two arms. The phases of electron and hole quasi-particles in the ring arms are varied by the magnetic field as in a normal AB quantum ring. This results in a modulation with a period h/e of the critical current, and thereby of the voltage V developed across the junction.
Figure 5.16(b) shows the junction current-voltage characteristics measured at 5 K for several external magnetic flux values comprised within the shadow region in Fig. 5.16(a). The evolution of the critical current with Φ is highlighted in light yellow. The range of magnetic fluxes is centred at 1.5 Φ_{AB}, thus in the region where the AB voltage oscillations present a minimum. By varying B, it is possible to tune the Josephson current making it to vanish when approaching 1.5 Φ_{AB} and to reappear when outrunning the minimum. The curves were recorded at high temperature, where the supercurrent was small enough to be suppressed by the magnetic flux. At lower temperatures, the Josephson current can be magnetostatically tuned as well [see Fig 5.16(a)] but not fully suppressed.

These results demonstrate that this system performs as a superconducting AB interferometer.

Chapter 6

Conclusions and future perspectives

In this thesis work we have investigated the transport properties of four kinds of devices: Normal Quantum Point Contacts (NQPCs), Normal Quantum Rings (NQRs), Superconductor-Quantum Point Contact-Superconductor (S-QPC-S) and Superconductor-Quantum Ring-Superconductor (S-QR-S) junctions. In the case of normal devices, we confirmed the conductance quantization [6, 7] and the magneto-electrostatic Aharonov-Bohm (AB) interference effect [8, 9]. In particular, by varying the gate voltage we observed five plateaus in the NQPC conductance, thus proving the ballistic nature of our devices. In NQRs, the conductance exhibited AB modulations with a remarkably high contrast of almost 20%. As a demonstration of the electrostatic AB effect, the phase and amplitude of these modulations were tuned by varying the voltage applied to one of the side gates. These results confirmed the quality of the fabricated devices, which showed a good electric stability and coherent transport through the 200-nm-wide ring arms.

In both kinds of hybrid junctions, we observed a well-defined Josephson current. In the 800-nm-wide S-QPC-S junctions, the supercurrent showed a Fraunhofer-like magnetic interference pattern that we were able to manipulate by applying a negative voltage to the side gates. In this way, we were able to shrink the effective width of the junctions until the interference pattern was reduced to the monotonic decay obtained in the 600-nm-wide junctions [10]. The interference pattern was also modified by varying the temperature of the junctions. We compared our results to the theoretical predictions made by Barzykin and Zagoskin [11], finding a good qualitative agreement for the position of the first-order minima as a function of the effective width and temperature. Furthermore, the critical current dependence on the gate voltageshowed some evidence of a quantized behaviour, even though not all the steps were clearly visible.

Finally, in the case of S-QR-S junctions, we observed magnetic modulations of

the Josephson current with an AB period h/e [12]. This result is in contrast with the interference periodicity $h/2e$ found in conventional SQUIDs or in diffusive metallic rings. It stems from the particular properties of the scattering matrix that describes the ballistic ring-shaped weak-link: if an external magnetic field is applied orthogonal to the plane of the junction, the electron and hole quasiparticle in the 2DEG ring arms acquire a phase as in a normal AB ring. The supercurrent flowing through the junction reflects this behaviour, thus showing a periodicity typical of an AB interferometer. This result agrees with the theoretical prediction made by Dolcini and Giazotto [14] for this particular system.
The investigated hybrid devices can be sought as promising building blocks to implement fully controllable Josephson π-junctions [69], which are of great interest in quantum computing. In particular, the supercurrent modulation in S-QR-S junctions can be electrostatically influenced by using side gates. Indeed, it has been shown [14] that the combination of electric and magnetic fields can reverse the sign of the Josephson current flowing through the junction. This aspect will be investigated in new devices, since the side gates in the fabricated S-QR-S junctions did not work properly, as mentioned in section 3.3.4.
Additionally, the study of such ballistic hybrid junctions might pave the way to the experimental investigation of topological superconductors, that may support the existence of Majorana fermions (MFs) [70, 71, 72]. The latter are particles identical to their own anti-particles, whose existence has been originally pointed out by Ettore Majorana in 1937 [73]. Although it is still unclear if there are elementary particles which are MFs, they have been theoretically predicted to manifest as zero-energy bound states in one-dimensional *p*-wave superconductors [74]. Since the existence of MFs is a topological invariant, it should be possible to find them also in hybrid structures, such as a semiconductor nanowire proximized by a common *s*-wave superconductor (Nb, for instance). In order to obtain a topological superconductor, the proximized semiconductor must have a high spin-orbit coupling (InAs and InSb are the best candidates) and an external magnetic field must be applied along the nanowire direction. Recently, this configuration has led to the first experimental results [75, 76] that might support the aforementioned predictions. In 2011 Wimmer *et al.* [77] claimed that MF existence could be detected in a topological quantum wire, whose conductance is controlled by a QPC.
On the basis of this thesis work, we have started to investigate new devices that can mimic the geometry studied by Wimmer *et al*. Figure 6.1 shows one of the prototypes fabricated at the end of this thesis work. It consists of a N-S junction, in which the normal part (coloured in yellow) is a 2.5-µm-long and 450-nm-wide quantum wire controlled by a QPC. The additional gates (labelled

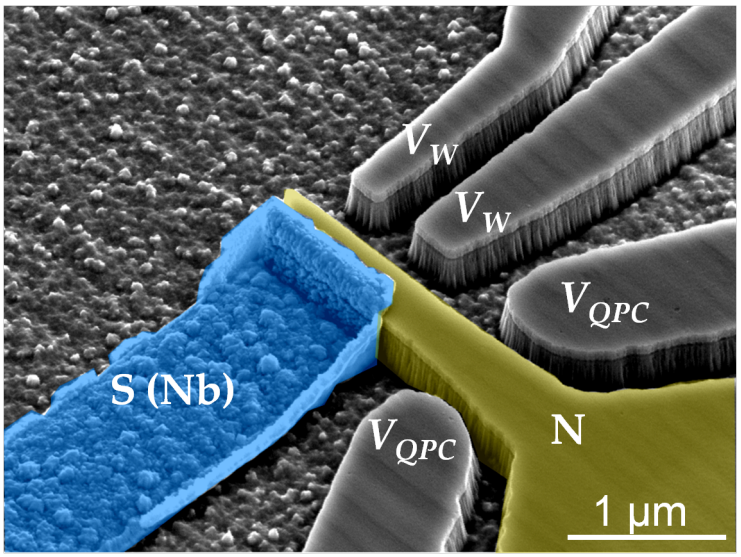

Figure 6.1: Pseudo-color scanning electron micrograph of one of the devices fabricated to investigate the existence of Majorana Fermions. The superconducting region (Nb) is coloured in blue, while the normal region (InAs 2DEG) appears in yellow. At one end of the wire two gates (labelled V_{QPC}) create the QPC, while at the other end two gates (labelled V_W) can be used to control the Fermi energy in the proximized region.

V_W) can be used to control the Fermi energy in the proximized region. We are currently working to fabricate and measure this and similar devices.
Beyond the fundamental research interest, MFs could be a very powerful tool for quantum computing, since they are de-localized non-abelian anyons that result to be very well protected from decoherence. For all these reasons, the search for MFs is nowadays one of the most fascinating quest in condensed matter physics.

Bibliography

[1] B. D. Josephson, *Phys. Lett.* **1**, 251 (1962).

[2] M. Tinkham, *Introduction to superconductivity*, McGraw-Hill, 1996.

[3] T. Schäpers, *Superconductor/semiconductor junctions*, Springer, 2001.

[4] H. Takayanagi, T. Akazaki, J. Nitta, *Phys. Rev. Lett.* **75**, 3533 (1995).

[5] T. Bauch, E. Hürfeld, V. M. Krasnov, P. Delsing, H. Takayanagi, T. Akazaki, *Phys. Rev. B* **71**, 174502 (2005).

[6] B. J. van Wees, H. van Houten, C. W. J. Beenakker, J. G. Williamson, L. P. Kouwenhoven, D. van der Marel, C. T. Foxon, *Phys. Rev. Lett.* **60**, 848 (1988).

[7] D. A. Wharam, T. J. Thornton, R. Newbury, M. Pepper, H. Ahmed, J. E. F. Frost, D. G. Hasko, D. C. Peacock, D. A. Ritchie, G. A. C. Jones, *J. Phys. C* **21**, 209 (1988).

[8] Y. Aharonov, D. Bohm, *Phys. Rev.* **115**, 485 (1959).

[9] Y. Aharonov, D. Bohm, *Phys. Rev.* **123**, 1511 (1961).

[10] M. Amado, A. Fornieri, F. Carillo, G. Biasiol, L. Sorba, V. Pellegrini, F. Giazotto, in preparation.

[11] V. Barzykin, A. M. Zagoskin, *Superlattices Microstruct.* **25**, 797 (1999).

[12] A. Fornieri, M. Amado, F. Carillo, F. Dolcini, G. Biasiol, L. Sorba, V. Pellegrini, F. Giazotto, arXiv: 1211.1629v1.

[13] J. Wei, P. Cadden-Zimansky, V. Chandrasekhar, P. Virtanen, *Phys. Rev. B* **84**, 224519 (2011).

[14] F. Dolcini, F. Giazotto, *Phys. Rev. B* **75**, 140511 (2007).

[15] J. Bardeen, L. N. Cooper, J. R. Schrieffer, *Phys. Rev* **106**, 162 (1957).

[16] J. Bardeen, L. N. Cooper, J. R. Schrieffer, *Phys. Rev* **108**, 1175 (1957).

[17] H. K. Onnes, *Leiden Comm.* **120b, 122b, 124c**, (1911).

[18] N. Bogoliubov, *Nuovo Cimento* **7**, 794 (1958).

[19] J. G. Valatin, *Nuovo Cimento* **7**, 843 (1958).

[20] G. Grosso, G. Pastori Parravicini, *Solid state physics*, Academic Press, 2000.

[21] P. G. de Gennes, *Superconductivity of metals and alloys*, Westview Press, 1999.

[22] G. E. Blonder, M. Tinkham, T. M. Klapwijk, *Phys. Rev. B* **25**, 4515 (1982).

[23] A. F. Andreev, *Zh. Éksp. Teor. Fiz.* **46**, 1823 (1964) [*Sov. Phys. JETP* **19**, 1228 (1964)].

[24] A. Messiah, *Quantum mechanics*, Dover, 1999.

[25] G. Bastard, *Wave mechanics applied to semiconductor heterostructures*, Les Éditions de Physique, 1988.

[26] S. Luin, *Spectroscopy of emergent states in quantum Hall bilayers*, PhD Thesis, Scuola Normale Superiore, Pisa, 2005.

[27] R. Dingle, H. L. Störmer, A. C. Gossard, W. Wiegmann, *Appl. Phys. Lett.* **33**, 665 (1978).

[28] S. J. Bass, *J. Cryst. Growth* **47**, 613 (1979).

[29] M. Büttiker, Y. Imry, R. Landauer, S. Pinhas, *Phys. Rev. B* **31**, 6207 (1985).

[30] I. O. Kulik, *Zh. Éksp. Teor. Fiz.* **57**, 1745 (1969) [*Sov. Phys. JETP* **30**, 944 (1970)].

[31] A. Chrestin, T. Matsuyama, U. Merkt, *Phys. Rev. B* **49**, 498 (1994).

[32] H. X. Tang, Z. D. Wang, Y. Zhang, *Z. Phys. B* **101**, 359 (1996).

[33] M. Octavio, M. Tinkham, G. E. Blonder, T. M. Klapwijk, *Phys. Rev. B* **27**, 6739-6746 (1983).

[34] K. Flensberg, J. Bindslev Hansen, M.Octavio, *Phys. Rev. B* **38**, 8707 (1988).

[35] Y. V. Sharvin, *Zh. Éksp. Teor. Fiz.* **48**, 984 (1965) [*Sov. Phys. JETP* **21**, 655 (1965)].

[36] T. J. Thornton, M. Pepper, H. Ahmed, D. Andrews, G. J. Davies, *Phys. Rev. Lett.* **56**, 1198 (1986).

[37] R. Landauer, *IBM J. Res. Dev.* **1**, 223 (1957).

[38] D. K. Ferry, S. M. Goodnick, J. Bird, *Transport in nanostructures*, Cambridge University Press, 2009.

[39] C. Nguyen, H. Kroemer, E. L. Hu, *Appl. Phys. Lett.* **65**, 103 (1994).

[40] K. Kajiyama, Y. Mizushima, S. Sakata, *Appl. Phys. Lett.* **23**, 458 (1973).

[41] F. Carillo, G. Biasiol, D. Frustaglia, F. Giazotto, L. Sorba, F. Beltram, *Physica E* **32**, 53 (2006).

[42] R. A. Webb, S. Washburn, C. P. Umbach, R. B. Laibowitz, *Phys. Rev. Lett.* **54**, 2696 (1985).

[43] G. Timp, A. M. Chang, J. E. Cunningham, T. Y. Chang, P. Mankiewich, R. Behringer, R. E. Howard, *Phys. Rev. Lett.* **58**, 2814 (1987).

[44] K. Ismail, S. Washburn, K. Y. Lee, *Appl. Phys. Lett.* **59**, 1998 (1991).

[45] A. Fuhrer, S. Lüscher, T. Ihn, T. Heinzel, K. Ensslin, W. Wegscheider, M. Bichler, *Nature* **413**, 822 (2001).

[46] V. Kotimäki, E. Räsänen, *Phys. Rev. B* **81**, 245316 (2010).

[47] D. Takai, K. Ohta, *Phys. Rev. B* **48**, 1537 (1993).

[48] E. B. Olshanetsky, M. Cassé, Z. D. Kvon, G. M. Gusev, L. V. Litvin, A. V. Plotnikov, D. K. Maude, J. C. Portal, *Physica E* **6**, 322 (2006).

[49] C. W. J. Beenakker, H. van Houten, *Phys. Rev. Lett.* **66**, 3056 (1991).

[50] A. Furusaki, H. Takayanagi, M. Tsukada, *Phys. Rev. B* **45**, 10563 (1992).

[51] J. Bardeen, R. Kümmel, A. E. Jacobs, L. Tewordt, *Phys. Rev.* **187**, 556 (1969).

[52] N. M. Chtchelkatchev, G. B. Lesovik, G. Blatter, *Phys. Rev. B* **62**, 3559 (2000).

[53] N. M. Shchelkachev, *JETP Lett.* **71**, 504 (2000).

[54] J. B. Ketterson, S. N. Song, *Superconductivity*, Cambridge University Press, 1999.

[55] J. Gu, W. Cha, K. Gamo, S. Namba, *J. Appl. Phys.* **50**, 6437 (1979).

[56] F. Rohlfing, G. Tkachov, F. Otto, K. Richter, D. Weiss, G. Borghs, C. Strunk, *Phys. Rev. B* **80**, 220507 (2009).

[57] J. P. Heida, B. J. van Wees, T. M. Klapwijk, G. Borghs, *Phys. Rev. B* **57**, r5618 (1998).

[58] G. Eilenberg, *Z. Phys.* **214**, 195 (1968).

[59] C. W. J. Beenakker, *Phys. Rev. Lett.* **67**, 3836 (1991).

[60] P. Y. Yu, M. Cardona, *Fundamentals of Semiconductors*, Springer, 2005.

[61] F. Capotondi, G. Biasiol, I. Vobornik, L. Sorba, F. Giazotto, A. Cavallini, B. Fraboni, *J. Vac. Sci. Technol. B* **22**, 702 (2004).

[62] F. Capotondi, G. Biasiol, D. Ercolani, L. Sorba, *J. Cryst. Growth* **278**, 538 (2005).

[63] F. Capotondi, G. Biasiol, D. Ercolani, V. Grillo, E. Carlino, F. Romanato, L. Sorba, *Thin Solid Films* **484**, 400 (2005).

[64] F. Pobell, *Matter and methods at low temperatures*, Springer, 2007.

[65] J. Cartwright, *Shortages spur race for helium-3 alternatives*, *Chemistry World*, January 2012.

[66] Heliox VL operator's handbook, Oxford Instruments, 2006.

[67] Triton 200 product guide, Oxford Instruments, 2012.

[68] H. Courtois, M. Meschke, J. T. Peltonen, J. P. Pekola, *Phys. Rev. Lett.* **101**, 067002 (2008).

[69] J. J. A. Baselmans, A. F. Morpurgo, B. J. van Wees, T. M. Klapwijk, *Nature* **397**, 43 (1999).

[70] J. Alicea, *Rep. Prog. Phys.* **75**, 076501 (2012).

[71] M. Leijnse, K. Flensberg, arXiv: 1206.1736v2.

[72] C. W. J. Beenakker, arXiv: 1112.1950v2.

[73] E. Majorana, *Nuovo Cimento* **14**, 171 (1937).

[74] A. Y. Kitaev, *Physics-Uspekhi* **44**, 131 (2001).

[75] V. Mourik, K. Zuo, S. M. Frolov, S. R. Plissard, E. P. A. M. Bakkers, L. P. Kouwenhoven, *Science* **336**, 1003 (2012).

[76] A. Das, Y. Ronen, Y. Most, Y. Oreg, M. Heiblum, H. Shtrikman, *Nature Physics* **8**, 887 (2012).

[77] M. Wimmer, A. R. Akhmerov, J. P. Dahlhaus, C. W. J. Beenakker, *New J. Phys.* **13**, 053016 (2011).

Acknowledgements

I would like to express my deepest gratitude to Mario Amado Montero for his constant support throughout the thesis work. He collaborated with me on all the experiments and taught me everything I know about working in a clean room facility. Most of all, he has always tried to fight my underlying indolence, helping me to solve one problem at a time.
I am also grateful to all the other members of the superconductivity group at Laboratorio NEST: Maria José Martínez Pérez, Alberto Ronzani, Maria Camarasa Gomez and Carles Altimiras Martin. They have been kind to me since my first day in the laboratory and they have become really good friends of mine. Without their contagious enthusiasm and their valuable advice everything would have been much more difficult for me.